LUND UNIVERSITY

Analysis of Structure, Composition and Growth of Semiconductor Nanowires by Transmission Electron Microscopy

Ek, Martin

2013

Analysis of Structure, Composition and Growth of Semiconductor Nanowires by Transmission Electron Microscopy

Martin Ek

Doctoral thesis

2013

LUND
UNIVERSITY

Polymer & Materials Chemistry
Centre for Analysis and Synthesis
Sweden

Akademisk avhandling som för avläggande av teknologie doktorsexamen vid tekniska fakulteten, Lunds universitet, kommer att offentligen försvaras i hörsal B på Kemicentrum, Getingevägen 60, fredagen den 31 januari 2014, kl. 13.00.

Fakultetsopponent

Prof. Jordi Arbiol, Institut de Ciència de Materials de Barcelona

Organization	Document name
LUND UNIVERSITY Centre for Synthesis and Analysis Department of Chemistry P.O. Box 124 SE-221 00 Lund, Sweden	DOCTORAL DISSERTATION Date of issue 9 December 2013
Author(s) Martin Ek	Sponsoring organization

Title and subtitle

Analysis of Structure, Composition and Growth of Semiconductor Nanowires by Transmission Electron Microscopy

Abstract

Nanowires have the potential to be a very flexible platform for the design of semiconductor devices. In nanowires it is possible to form crystal structures not found in the bulk materials under normal conditions, and to combine different III-V and group IV materials into axial or radial heterostructures. As quite complex structures can be formed, both intentionally and unintentionally, characterization of the crystal structure and composition is important. In this thesis, various transmission electron microscopy techniques are presented for this purpose.

High resolution imaging can directly visualize the crystal structure, including twinning and stacking faults. The polar nature of the III-V materials leaves one more parameter to be determined. In order to determine polarity from high resolution images it is not only necessary to improve the resolution further by aberration correction, but in addition the local orientation of the sample must be determined. Convergent beam electron diffraction is an alternative method with much lower demands on the microscope and operator, and can be adapted to suit most materials and crystal structures.

Transmission electron microscopy also provides several methods for determining and mapping the composition of the nanowires. It is important in all cases to avoid damaging the nanowires during the acquisition of the analytical signal. In the most commonly used method, energy dispersive X-ray spectroscopy, this can be achieved by spreading the electron dose over as large an area as possible. If there is only a single unknown parameter for the composition, alternative methods such as the shift in plasmon energy with composition can be used instead, as they have higher collection efficiencies.

In order to improve the nanowires in terms of crystal structure and composition, these must be connected to the dynamic processes occurring during growth. Occasionally these processes can be inferred from the fully formed nanowires after growth, but ideally one would like to observe the growth *in-situ* in the microscope. This is usually possible only with highly specialized environmental microscopes. In this thesis, nanowire growth in much simpler closed cells is demonstrated. Although the growth conditions could neither be precisely measured nor controlled, the closed cells made it possible to observe for the first time growing InAs nanowires *in-situ* in a conventional transmission electron microscope.

Key words

Transmission electron microscopy, nanowires, III-V semiconductors, polarity, *in-situ*TEM

Classification system and/or index terms (if any)

Supplementary bibliographical information	Language English
ISSN and key title	ISBN 978-91-7422-340-8
Recipient´s notes	Number of pages 191 Price
	Security classification

Analysis of Structure, Composition and Growth of Semiconductor Nanowires by Transmission Electron Microscopy

Martin Ek

Doctoral thesis

2013

LUND
UNIVERSITY

Polymer & Materials Chemistry
Centre for Analysis and Synthesis
Sweden

Cover: High resolution transmission electron micrograph recorded from the heterojunction region of an InAs-GaSb nanowire, illustrating the transition from a zincblende to a wurtzite crystal structure type.

Polymer & Materials Chemistry
Centre for Analysis and Synthesis
Lund University
P.O. Box 124
SE-221 00 Lund
Sweden

ISBN 978-91-7422-340-8
Printed by Media-Tryck, Lund
December 2013

Abstract

Nanowires have the potential to be a very flexible platform for the design of semiconductor devices. In nanowires it is possible to form crystal structures not found in the bulk materials under normal conditions, and to combine different III-V and group IV materials into axial or radial heterostructures. As quite complex structures can be formed, both intentionally and unintentionally, characterization of the crystal structure and composition is important. In this thesis, various transmission electron microscopy techniques are presented for this purpose.

High resolution imaging can directly visualize the crystal structure, including twinning and stacking faults. The polar nature of the III-V materials leaves one more parameter to be determined. In order to determine polarity from high resolution images it is not only necessary to improve the resolution further by aberration correction, but in addition the local orientation of the sample must be determined. Convergent beam electron diffraction is an alternative method with much lower demands on the microscope and operator, and can be adapted to suit most materials and crystal structures.

Transmission electron microscopy also provides several methods for determining and mapping the composition of the nanowires. It is important in all cases to avoid damaging the nanowires during the acquisition of the analytical signal. In the most commonly used method, energy dispersive X-ray spectroscopy, this can be achieved by spreading the electron dose over as large an area as possible. If there is only a single unknown parameter for the composition, alternative methods such as the shift in plasmon energy with composition can be used instead, as they have higher collection efficiencies.

In order to improve the nanowires in terms of crystal structure and composition, these must be connected to the dynamic processes occurring during growth. Occasionally these processes can be inferred from the fully formed nanowires after growth, but ideally one would like to observe the growth *in-situ* in the microscope. This is usually possible only with highly specialized environmental microscopes. In this thesis, nanowire growth in much simpler closed cells is demonstrated. Although the growth conditions could neither be precisely measured nor controlled, the closed cells made it possible to observe for the first time growing InAs nanowires *in-situ* in a conventional transmission electron microscope.

List of papers

This thesis is based on the following papers, which will be referred to in the text by Roman numerals.

I **Electron Image Series Reconstruction of Twin Interfaces in InP Superlattice Nanowires**
M. Ek, M. T. Borgström, L. S. Karlsson, C. J. D. Hetherington, and L. R. Wallenberg
Microscopy and Microanalysis **17** (2011) 752

II **Changes in Contact Angle of Seed Particle Correlated with Increased Zincblende Formation in Doped InP Nanowires**
J. Wallentin, M. Ek, L. R. Wallenberg, L. Samuelson, K. Deppert, and M. T. Borgström
Nano Letters **10** (2010) 4807

III **Formation of the Axial Heterojunction in GaSb/InAs(Sb) Nanowires with High Crystal Quality**
M. Ek, B. M. Borg, A. W. Dey, B. Ganjipour, C. Thelander, L.-E. Wernersson, and K. A. Dick
Crystal Growth & Design **11** (2011) 4588

IV **Diameter Limitation in Growth of III-Sb-Containing Nanowire Heterostructures**
M. Ek, B. M. Borg, J. Johansson, and K. A. Dick
ACS Nano **7** (2013) 3668

V **Continuous Gas-Phase Synthesis of Nanowires with Tunable Properties**
M. Heurlin, M. H. Magnusson, D. Lindgren, M. Ek, L. R. Wallenberg, K. Deppert, and L. Samuelson
Nature **492** (2012) 90

VI **InAs Nanowire Growth Observed In-Situ by Transmission Electron Microscopy**
F. Lenrick, M. Ek, K. Deppert, L. Samuelson, and L. R. Wallenberg
Manuscript

My contributions

I I acquired the focal series together with C. J. D. Hetherington and performed the focal series reconstruction, the analysis of the reconstructed object wavefunction, and the multislice simulations. I was the main author of the paper.

II I acquired the TEM and STEM images, performed the XEDS compositional analyses, and quantified the crystal structures.

III I acquired the TEM and STEM images, performed the XEDS compositional analysis, and the tracking of the seed particle composition during the switch of materials. I was the main author of the paper.

IV I acquired the TEM and STEM images, performed the XEDS compositional analysis and the GPA local lattice parameter measurements. I took part in applying the Gibbs-Thomson model to the growth data. I was the main author of the paper.

V I performed the CBED polarity determinations and wrote the corresponding parts of the paper.

VI The paper contains equal contributions from myself and F. Lenrick with regards to the design of the cell, performing and analysing the *in-situ* experiments, and writing the paper.

Papers not included in the thesis:
I contributed to the following papers which are outside the scope of this thesis.

vii **Valence Band Splitting in Wurtzite InP Nanowires Observed by Photoluminescence and Photoluminescence Excitation Spectroscopy**
G. L. Tuin, M. T. Borgström, J. Trägårdh, M. Ek, L. R. Wallenberg, L. Samuelson and M.-E. Pistol
Nano Research **4** (2011) 159

viii **In Situ Etching for Total Control Over Axial and Radial Nanowire Growth**
M. T. Borgström, J. Wallentin, J. Trägårdh, P. Ramvall, M. Ek, L. R. Wallenberg, L. Samuelson, and K. Deppert
Nano Research **3** (2010) 264

ix **Probing the Wurtzite Conduction Band Structure Using State Filling in Highly Doped InP Nanowires**
J. Wallentin, K. Mergenthaler, M. Ek, L. R. Wallenberg, L. Samuelson, K. Deppert, M.-E. Pistol, and M. T. Borgström
Nano Letters **11** (2011) 2289

x **High Current Density Esaki Tunnel Diodes Based on GaSb-InAsSb Heterostructure Nanowires**
B. Ganjipour, A. W. Dey, B. M. Borg, M. Ek, M.-E. Pistol, K. A. Dick, L.-E. Wernersson, and C. Thelander
Nano Letters **11** (2011) 4222

xi **InAs Quantum Dots and Quantum Wells Grown on Stacking-Fault Controlled InP Nanowires with Wurtzite Crystal Structure**
K. Kawaguchi, M. Heurlin, D. Lindgren, M. T. Borgström, M. Ek, and L. Samuelson
Applied Physics Letters **99** (2011) 131915

xii **Diameter Reduction of Nanowire Tunnel Heterojunctions Using In-Situ Annealing**
B. M. Borg, M. Ek, K. A. Dick, B. Ganjipour, A. W. Dey, C. Thelander, and L.-E. Wernersson
Applied Physics Letters **99** (2011) 203101

xiii **Degenerate p-Doping of InP Nanowires for Large Area Tunnel Diodes**
J. Wallentin, P. Wickert, M. Ek, A. Gustafsson, L. R. Wallenberg, M. H. Magnusson, L. Samuelson, K. Deppert, and M. T. Borgström
Applied Physics Letters **99** (2011) 253105

xiv **Electron Trapping in InP Nanowire FETs with Stacking Faults**
J. Wallentin, M. Ek, L. R. Wallenberg, L. Samuelson, and M. T. Borgström
Nano Letters **12** (2012) 151

xv **Single GaInP Nanowire p-i-n Junctions Near the Direct to Indirect Bandgap Crossover Point**
J. Wallentin, L. B. Poncela, A. M. Jansson, K. Mergenthaler, M. Ek, D. Jacobsson, L. R. Wallenberg, K. Deppert, L. Samuelson, D. Hessman, and M. T. Borgström
Applied Physics Letters **100** (2012) 241103

xvi **Influence of Doping on the Electronic Transport in GaSb/InAs(Sb) Nanowire Tunnel Devices**
B. M. Borg, M. Ek, B. Ganjipour, A. W. Dey, K. A. Dick, L.-E. Wernersson, and C. Thelander
Applied Physics Letters **101** (2012) 043508

xvii **Combinatorial Approaches to Understanding Polytypism in III-V Nanowires**
J. Johansson, J. Bolinsson, M. Ek, P. Caroff, and K. A. Dick
ACS Nano **6** (2012) 6142

xviii **Carrier Control and Transport Modulation in GaSb/InAsSb Core/Shell Nanowires**
B. Ganjipour, M. Ek, B. M. Borg, K. A. Dick, M.-E. Pistol, L.-E. Wernersson, and C. Thelander
Applied Physics Letters **101** (2012) 103501

xix **Demonstration of Defect-Free and Composition Tunable $Ga_xIn_{1-x}Sb$ Nanowires**
S. G. Ghalamestani, M. Ek, B. Ganjipour, C. Thelander, J. Johansson, P. Caroff, and K. A. Dick
Nano Letters **12** (2012) 4914

xx **Single InAs/GaSb Nanowire Low-Power CMOS Inverter**
A. W. Dey, J. Svensson, B. M. Borg, M. Ek, and L.-E. Wernersson
Nano Letters **12** (2012) 5593

xxi **Vertical "III-V" V-Shaped Nanomembranes Epitaxially Grown on a Patterned Si[001] Substrate and Their Enhanced Light Scattering**
S. Conesa-Boj, E. Russo-Averchi, A. Dalmau-Mallorqui, J. Trevino, E. F. Pecora, C. Forestiere, A. Handin, M. Ek, L. Zweifel, L. R. Wallenberg, D. Rueffer, M. Heiss, D. Troadec, L. Dal Negro, P. Caroff, and A. Fontcuberta i Morral
ACS Nano **6** (2012) 10982

xxii **High-Current GaSb/InAs(Sb) Nanowire Tunnel Field-Effect Transistors**
A. W. Dey, B. M. Borg, B. Ganjipour, M. Ek, K. A. Dick, E. Lind, C. Thelander, and L.-E. Wernersson
IEEE Electron Device Letters **34** (2013) 211

xxiii **FIB Plan and Side View Cross-Sectional TEM Sample Preparation of Nanostructures**
F. Lenrick, M. Ek, D. Jacobsson, M. T. Borgström, and L. R. Wallenberg
Microscopy and Microanalysis, Accepted DOI: 10.1017/S1431927613013780

Abbreviations

ADF	annular dark field
BF	bright field
CBE	chemical beam epitaxy
CBED	convergent beam electron diffraction
CCD	charge-coupled device
CLC	centre of Laue circle
DEZn	diethyl zinc
DF	dark field
DMZn	dimethyl zinc
EDX	energy dispersive X-ray
EEL	electron energy loss
EELS	electron energy loss spectroscopy
FEG	field emission gun
FWHM	full width at half maximum
GPA	geometric phase analysis
HAADF	high angle annular dark field
HRTEM	high resolution transmission electron microscopy
MBE	molecular beam epitaxy
MO	metalorganic
MOVPE	metalorganic vapour phase epitaxy
MTF	modulation transfer function
PCA	principal component analysis
SAED	selected area electron diffraction
SEM	scanning electron microscopy
STEM	scanning transmission electron microscopy
TEM	transmission electron microscopy
TMIn	trimethyl indium
TMSb	trimethyl antimony
V/III	ratio between group V and III precursor partial pressures
WZ	wurtzite
XEDS	energy dispersive X-ray spectroscopy
ZB	zincblende
ZLP	zero-loss peak

Symbols

Aberration coefficients of the type A_x, B_x, and C_x are listed in full in table 2.1 on page 13, and have not been included in this table.

c	image contrast in real space
C	image contrast in reciprocal space
d	diameter
E	energy loss
E_c	(temporal coherence) envelope function due to defocus spread
E_p	plasmon energy loss
E_s	(spatial coherence) envelope function due to non-parallel illumination
f	atomic scattering factor
G	Bragg reflection
h	height (of nucleus)
H	curvature of a surface (of e.g. a particle)
I	intensity
k	reciprocal space coordinate
L	liquid (phase)
n	nucleus (phase)
l	length (of segment in nanowire)
p	transfer function in Wiener filter
P	pressure
P_g	relative geometric phase
P_g'	geometric phase
R	gas constant
S	solid (phase)
T	transmission coefficient
T	temperature
V	vapour (phase)
V	molar volume
V_t	projected potential
W	wave aberration function
x	real space coordinate
x	fraction of nucleus in contact with vapour
x	solute fraction
x_{eq}	solute fraction at equilibrium

Z	atomic number
α	electron beam convergence semi-angle
α	utilization factor of MOVPE precursors
β	electron beam collection semi-angle
β	seed particle contact angle
γ	interface energy
Γ	effective interface energy of nucleus
ΔC_1	defocus spread
Δf	difference in atomic scattering factor
ΔG	difference in Gibb's free energy
ΔZ	difference in atomic number
$\Delta\mu$	difference in chemical potential
λ	(electron) wavelength
ν	noise term in Wiener filter
σ	interaction constant relating projected potential to electron phase change
Φ	difference in cohesive energy of zincblende and wurtzite
φ	phase of scattered electron beam
χ	phase change due to lens aberrations
ψ_{illum}	illumination wavefunction in real space
ψ_i	image wavefunction in real space
ψ_o	object wavefunction in real space
Ψ_i	image wavefunction in reciprocal space
Ψ_o	object wavefunction in reciprocal space
$\Psi_{o,s}$	scattered part of object wavefunction in reciprocal space
ω	scattering angle

Contents

Chapter 1

Introduction

Structural and compositional characterization is an essential part of all materials research. Knowledge of these characteristics can provide an important connection between the performance of the material and the conditions used during its synthesis. The ideal for any structural characterization method would be to obtain, for each atom in a sample, the position, element and bonding. The modern transmission electron microscope is a very versatile tool capable of obtaining information on all three of these aspects. In most cases the sample itself limits the analysis however, and compromises must be made between resolution and precision. For this reason, it is important to continuously develop and improve the microscopy techniques.

Characterization at the atomic level might seem excessive, but in some areas the development has reached a point where design at this scale is becoming reality. Semiconductor devices are probably the best example, as they have been produced with components smaller than one hundred nanometres for the past ten years. Since then, not only have these devices become smaller, but there has also been a constant effort to make use of new materials, new combinations of materials, and new types of structures for enhancing device performance. Nanowires, crystals several hundreds of nanometres long but only a few tens of nanometres in diameter, are an example of this. The small diameter is in itself advantageous in many applications, but nanowires have several additional attributes which make them a very flexible platform for designing devices. For instance, nanowires have the ability to adopt crystal structures that are not usually found in the corresponding bulk materials. It is also possible in nanowires to combine several different semiconductor materials in both axial and radial heterostructures. Nanowires can in other words be synthesized, or grown, to from complex structures in terms of both crystal structure and composition.

In this thesis transmission electron microscopy techniques, which have been developed and adapted for the characterization of semiconductor nanowires, are presented. More specifically, nanowires of III-V materials – compounds consisting of group III

and group V elements – have been investigated in terms of both crystal structure and composition. The growth of III-V nanowires is discussed in chapter 3 and forms the framework for interpreting the results from the electron microscopy characterization.

While the crystal structure type, including stacking faults and twinning, can be determined locally directly from high resolution images as described in chapter 4, the determination of polarity of the III-V materials requires the use of additional methods. The polar nature of the III-V materials is discussed more in chapter 5, where two techniques for determining the polarity are also presented. When polar substrates are used these should provide a known reference for the polarity of the nanowires. Recently, new growth methods that use non-polar substrates, or do away with substrates altogether, have gained interest, making polarity determination important.

Transmission electron microscopy also offers many possibilities for compositional analysis at the nanoscale. In chapter 6 a selection of methods suitable for nanowires of III-V materials is discussed. In choosing a suitable method, it is important to consider the damage caused by the electron beam during the time the analytical signal is acquired. Energy dispersive X-ray spectroscopy is the most flexible method in terms of which materials can be characterized, but does not have the highest signal collection efficiency. It is therefore be important to consider alternative methods, and to make sure that the electron dose is spread over as large an area as possible.

The crystal structure and composition of the fully formed nanowires, even if determined with high resolution and precision, do not directly reveal what happened during the growth, but can of course provide important clues. Knowing how the dynamic processes occurring during the growth formed the final structure would be of tremendous help when attempting to modify it. The ideal solution would be to observe the growing nanowires in real time. Such *in-situ* observations normally require specialized microscopes, capable of containing the gaseous reactants at the sample. In chapter 7 a much simpler closed cell, used for the observation of growing InAs nanowires in a conventional transmission electron microscope, is discussed.

The use of nanowires of III-V materials in devices is not a part of this thesis, but is of course an important motivation for synthesizing and characterizing them in the first place. For this reason, four potential applications are presented at the end of this introduction which can be useful to keep in mind when the minutiae of the characterization methods are being discussed in later chapters.

A Brief Introduction to Electron Microscopy

The main advantage of electron microscopes lies in their resolution. For any microscope based on some type of illumination and lenses, the resolution is ultimately determined by the illumination wavelength and the degree of perfection of the lenses. Electrons accelerated to large velocities by an electric potential can achieve very short wavelengths

of only a fraction of the distances between the atoms in a solid material. Even at velocities of around 3/4 of the speed of light, electrons can be focused and deflected using magnetic fields, much like photons in a visible light microscope can be focused and deflected using glass lenses and prisms. The magnetic lenses used in electron microscopy are far from perfect, but compared to lenses for photons of similar wavelengths they are spectacularly good.

This thesis is focused on transmission electron microscopy (TEM), where acceleration potentials of hundreds of thousands of volts allow the electrons to pass through thin samples. Chapter 2 provides a general overview of transmission electron microscopy, while the specific techniques for analysing semiconductor nanowires are described in the subsequent chapters. The most common type of electron microscope is however probably the scanning electron microscope. In scanning electron microscopy (SEM) the acceleration voltage is one to two orders of magnitude lower than in TEM, and the incident electrons do not pass through the sample. Instead the image is usually formed from the secondary electrons ejected from the sample surface. In this thesis, SEM images are shown at a few places to illustrate the morphology of the nanowires.

Sample preparation usually features quite heavily in theses on TEM as it is a considerable challenge in most cases to produce electron transparent samples, especially if they are to be representative of the material as a whole. Nanowires are however already thin enough to be electron transparent, making the sample preparation relatively simple. For most nanowire samples it is sufficient to simply rub a carbon film coated grid on the substrate surface, whereby nanowires break off from the substrate and attach to the carbon film. After that, it is only a matter of perseverance to find nanowires which happen to be suitably oriented, and where the region of interest is located over a hole in the carbon film.

In cases where it is necessary to analyse the nanowire-substrate interface or to analyse the nanowires in cross section, the sample preparation becomes considerably more difficult. In paper xxiii, Lenrick et al. demonstrate the use of focused ion beam machining for creating these types of samples.

Advantages and Applications for Nanowires

Semiconductor technology based on silicon has been developed over many decades by now, and uses comparatively cheap and abundant raw materials. The III-V materials, although having superior properties, will therefore be most useful as complements to, rather than replacements of, silicon. One of the greatest advantages of nanowires is that they offer a route for combining silicon and the III-V materials, as III-V nanowires can be grown directly on silicon substrates.[1, 2]

Although the III-V materials and silicon have similar crystal structures the spacing between their atoms differ, which can be seen from the differing lattice parameters in

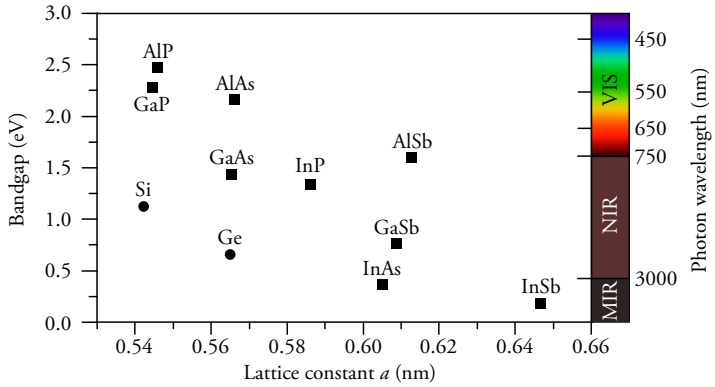

Figure 1.1: Bandgap vs. lattice constant for a selection of group IV (•) and III-V (▪) semiconductor materials. The corresponding photon wavelengths, ranging from visible (VIS) to near (NIR) and mid (MIR) infrared, are shown for comparison.

figure 1.1. Normally, when combining material with different lattice parameters, defects are generated at the interface due to the strain. For thin nanowires the strain can instead be accommodated by the material contracting or expanding at the perimeter.[3] For larger diameters, defects will also form in nanowires, but even here the nanowire geometry can be beneficial by hindering the defects from extending into the active areas of the device.[4]

The ability to combine materials with different lattice parameters also is useful for creating heterostructures within the nanowires. Figure 1.1 only shows the difference between the III-V materials in one aspect, the bandgap value, but there are of course several other aspects that need to be considered, e.g. bandgap type, band alignment, and carrier mobility. Combined with the possibility in nanowires to also control the crystal structure of these materials, nanowires offer a great deal of freedom when designing semiconductor structures.

Four application areas where III-V nanowires potentially can be used are presented below. These applications all have in common that they require advanced structures with a high degree of perfection in terms of compositions and crystal structures. Characterization by transmission electron microscopy will in other words be essential during their development.

Photovoltaics are devices which convert sunlight directly into electrical power. The III-V materials are better than silicon at absorbing light, but are too expensive to use in the large area solar panels that are needed. By growing the III-V materials as nanowires on silicon substrates instead of as self-supporting films, the amount of III-V material that is needed is drastically reduced. Furthermore, by carefully tuning the length, diameter and spacing, nanowires can actually be made to absorb light more efficiently than a solid film, even though they only cover a small fraction of the surface.[5]

The efficiency of converting light into electrical power for any single semiconductor material is limited by the fact that only photons with energies greater than the bandgap can be absorbed. The energy exceeding the bandgap is however lost to heat and cannot be used to produce electrical power. In order to produce high efficiency solar cells it is therefore necessary to combine several different materials with different bandgaps, and therefore usually different lattice parameters. Here, the ability of nanowires to accommodate strain or contain the defects could be important.

Light-emitting diodes are very efficient light sources, which in a way operate like a photovoltaic device in reverse. In light-emitting diodes, electron-hole pairs are recombined to produce photons, with energies corresponding to the bandgap of the semiconductor. In materials with indirect bandgaps, like silicon, this process is far too slow to be useful. Many of the III-V materials have direct bandgaps and are therefore better suited for this purpose. Using nanowires it could be possible to add such devices also to silicon based electronics in order to provide, for instance, optical communication.[6, 7]

At larger scales, light emitting diodes can also be used for lighting as they are far much more efficient than incandescent light bulbs. In order to provide light with different colours it will be necessary to use either different semiconductor materials with different bandgaps, or to use quantum confinement effects. Nanowires offer possibilities for both these routes.

Transistors form the basis of all modern electronics. Most transistors work by controlling the availability of charge carriers in a channel, and therefore the conductivity of the device as a whole, using an electric field applied by a gate electrode. For transistors designed with a nanowire as the channel it is possible to wrap the gate around the entire structure, resulting in the ultimate electrostatic control of the conductivity.[8]

Even with wrap-around gates, transistors working according to the above principles still have limits. For instance, the electric bias applied to the gate in the off-state of the transistor cannot be made too small, or a current will leak through the device. In order to allow for more efficient switching, new transistor types, such as tunnelling transistors, are being explored. These devices typically instead suffer from poor current levels in the on-state. By using heterostructures of III-V materials it might however be possible to improve this characteristic and make tunnelling transistors competitive.[9, 10] In such devices a narrow channel, formed for instance from a nanowire, has been predicted to be essential.[11]

Quantum devices working on radically different principles than today's electronics can also be fabricated from nanowires. For these applications, just as in the ones described earlier, it is the combination of high performance III-V materials with small diameters that is the key to creating functional devices. Notable examples include electronics utilizing also the spin of the charge carriers (spintronics)[12] and the creation of the solid state analogue of Majorana fermions.[13, 14] Both of these effects have been proposed for the use as quantum bits.

Chapter 2

Transmission Electron Microscopy

This chapter will give an overview of the workings of a transmission electron microscope and some background for the various techniques, which is needed when their application to the characterization of nanowires is discussed in later chapters. The two microscopes mainly used for the studies on which this thesis is based, the 300 kV JEOL 3000F in Lund and the 200 kV aberration corrected JEOL 2200MCO at the Department of Materials in Oxford, are used as examples.

There are two principal operating modes for transmission electron microscopes: transmission electron microscopy (TEM) where a parallel beam is used to illuminate the entire imaged region and scanning transmission electron microscopy (STEM) where the beam is focused to a point that is scanned over the sample, recording the image sequentially pixel by pixel. Image formation will be discussed in some detail for high resolution TEM (HRTEM) as this method has been used to record lattice resolved images. The theory behind image formation also forms the framework for image simulations, and for measuring and correcting the lens aberrations.

Contrast, the relative difference in intensity between parts of an image, is a very important concept in microscopy. The description of imaging in HRTEM and the limits to resolution from lens aberrations and microscope instabilities are all described in terms of how the contrast is reduced for different separations, or frequencies, between objects. If the contrast is reduced to zero for high frequencies, which is equivalent to short separations between objects, these will not contribute to the image. The lack of contrast can potentially make it impossible to resolve the separate objects as they might appear as one uniform "blob" in the image.

When talking about resolution it can be useful to put the numbers in relation to some actual interatomic distances in the materials we are interested in. For example, if the resolution is better than 0.34 nm it is possible to resolve the {111} planes in InP, which makes it possible to distinguish the wurtzite and zincblende crystal structure types in the images. For InP this could be said to be the minimum resolution where the term

high resolution TEM is warranted. If the resolution is improved to better than 0.15 nm even the shortest In-P distances in the ⟨110⟩ projection can be resolved, enabling full resolution of every individual atomic column. Provided that the different atoms can also be differentiated in the images, this would make it possible to determine whether the growth proceeds from planes terminated by In or P atoms, or whether there are homoatomic bonds (In-In or P-P) or heteroatomic bonds (In-P) across a twin interface. If we instead look at InP in a ⟨112⟩ projection this distance is only 0.08 nm, requiring a much higher resolution.

2.1 The Instrument

In figure 2.1 a photograph of a medium voltage (which in the context of TEM is 200-300 kV) transmission electron microscope is shown (a) together with a schematic drawing of the same (b). The microscope can be divided into three sections: the illumination system, the image forming system, and the projection system. The description in this section is for a microscope operated as a TEM and follows the description given by Williams and Carter[15], unless other references are given. STEM will be described in a separate section later.

The illumination system consists of the electron gun, an acceleration tube, and a series of lenses with the purpose of projecting a uniform and ideally parallel (but in reality slightly convergent) beam of electrons onto the sample. The gun itself is basically a filament which is either heated until it emits electrons (thermionic gun) or subjected to a very strong electric field which extracts electrons from the tip (field emission gun). The field emission gun (FEG) has the great advantage of emitting electrons from a very small region with a very small spread in energy – and consequently a small spread in wavelength – making the illumination highly coherent. This is very important for high resolution imaging and even more so for image series reconstruction, as will be shown later. Often the FEGs are also heated somewhat and are then called Schottky sources, in contrast to the unheated cold-FEGs. By increasing the temperature a small increase in energy spread is traded for increased emission stability and less stringent vacuum requirements. Both microscopes used in this thesis employ a Schottky source. The potential drop in the accelerator tube, the acceleration voltage, determines the wavelength of the electrons. At 200-300 kV the electrons have a wavelength of 0.0025-0.0019 nm and travel at approximately 3/4 the speed of light. Despite this large velocity the samples need to be very thin, at most a few hundred nanometres, in order not to scatter the electrons too much.

The illumination system also contains the condenser aperture, which allows the electrons emitted at high angles to be excluded at the cost of reducing the beam current. This allows some control of the illumination convergence angle for any given diameter of the beam.

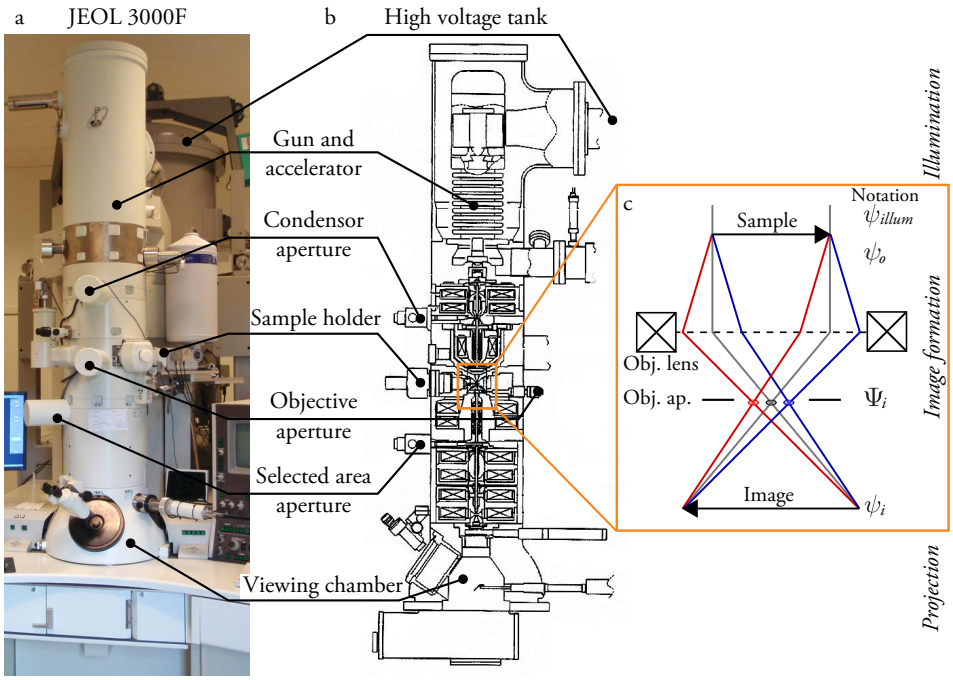

Figure 2.1: (a) Photograph of the 300kV JEOL 3000F TEM in Lund[1] with a few of the principal elements marked. (b) Cross-section illustration of the same instrument. (c) Ray diagram for the image forming (objective) lens showing the location of the diffraction pattern and the objective aperture in the back focal plane. Not included in this diagram are the effects from spherical aberration, which in a real lens strongly affects the paths of the electrons. Also not shown is the selected area aperture which should be located in the image plane.

The image forming system contains the sample and the strongest lens in the microscope: the objective lens. The description of high resolution imaging later is essentially about how the electron wave becomes distorted by the aberrations of this one lens, with the illumination system being reduced to a few parameters and the projection system more or less ignored. The sample and objective lens are shown in more detail in figure 2.1c from a ray optics perspective, together with the wave optics notation used for high resolution imaging. The parallel illumination interacts with the sample, is scattered and then brought to a focus by the objective lens. For a purely periodic sample, such as an ideal crystal lattice, the electrons will be diffracted only to certain angles. Note that rays scattered to the same angles are focused into points in the back-focal plane, forming the diffraction pattern. Even when dealing mostly with imaging the diffraction pattern is very important: the distribution of intensity between the different spots gives a clear

[1] Photo courtesy of Gunnel Karlsson.

indication of the sample orientation, allowing the crystals to be tilted to the desired viewing direction.

Two apertures are also included in the image forming system: the objective aperture and the selected area aperture. The objective aperture is inserted into the back-focal plane and excludes electrons scattered more than a certain angle, which is very important for the contrast and quality of the images. The selected area aperture is located in a conjugate image plane: when it is inserted only electrons from a small part of the illuminated area are allowed to pass. This allows diffraction patterns to be collected from small areas even with a wide, and therefore less convergent, illumination.

The projection system is responsible for projecting and magnifying either the image or the diffraction pattern formed by the objective lens. In order to see the final image it is projected onto either a phosphorescent screen for quick viewing, or onto a scintillator fiber-optically coupled to a CCD (charge-coupled device) detector for recording digital images. The impinging electrons and the photons they generate will be scattered to some degree in the scintillator, which can blur the image and reduce the contrast. In addition, the process of converting a continuous signal to a discrete, pixelated image will also reduce the contrast for rapidly varying features. This detector-related degradation of the image is described by the modulation transfer function (MTF) and can be measured by imaging a known object, such as a sharp edge.[16] Other detectors which instead detect the impinging electron directly or use different read out methods have been developed recently, but were not available on either of the microscopes used to record the images presented in this thesis.

Contrast in Conventional TEM

There are many different mechanisms for generating contrast in TEM. For the purpose of forming images in TEM the electrons are best described as waves, and the contrast mechanisms can therefore be divided according to whether they rely on the amplitude or the phase of the transmitted waves. The description of phase contrast used in high resolution imaging will occupy much of the remainder of this chapter, but a brief description of two other important mechanisms relying on differences in amplitude is included here. Mass-thickness contrast relies on the fact that heavier elements or thicker areas of the sample scatter more of the incoming electrons to high angles. These high angle electrons are then excluded from the image by the objective aperture or by the column itself, making the corresponding areas in the image dimmer. Diffraction contrast works by a very similar mechanism but relates more specifically to when a smaller objective aperture is used to select only a single or a few diffraction spots. In that case only areas which diffract in this very specific direction will have any intensity in the image. Such images are referred to as either bright field (BF) or dark field (DF) if they are formed from the direct or a diffracted beam respectively.

2.2 High Resolution Imaging

In TEM, phase contrast provides most of the high resolution information in the images. Electrons passing close to an atomic nucleus will temporarily be slightly accelerated, and thus receive a different phase, compared to electrons passing further away where the nucleus is shielded by its surrounding electrons. For a thin sample, this phase shift will be the sole effect on the passing electrons. In the *phase object approximation* the phase shift of the electron wavefunction after the object, ψ_o, depends on the projected potential of the sample along the path of the electron, V_t, and an interaction parameter, σ. If the phase shift is small it has approximately a linear dependence on V_t, as shown in the *weak phase object approximation* in equation 2.1.

$$\psi_o = \exp\left[-i\sigma V_t(\mathbf{x})\right] \approx 1 - i\sigma V_t(\mathbf{x}) \tag{2.1}$$

Equation 2.2 shows the object wavefunction in reciprocal space, which is related to the expression in equation 2.1 by Fourier transformation. As a convention, lower case symbols with coordinate $\mathbf{x}$ will be used in real space, while upper case symbols with coordinate $\mathbf{k}$ are used as the reciprocal space equivalents. To somewhat simplify the derivation of the phase contrast transfer function in the next section, the terms for the scattered electron beams are collected into $\Psi_{o,s}$.

$$\Psi_o = \mathcal{F}\psi_o = \delta - i\sigma V_t(\mathbf{k}) = \delta + \Psi_{o,s} \tag{2.2}$$

The weak phase object approximation is only strictly correct for very thin samples; even a single heavy atom could break the condition that the phase shift should be very small. An even bigger problem is that the projected potential model is invalid for thicker samples where multiple scattering is significant, which makes a 2D potential distribution an inadequate description.

The Phase Contrast Transfer Function

For a description of how the aberrations of the objective lens affect the object wavefunction it is easiest to start from the contrast in the image, c.[17, 18] The image contrast stems from the amplitude of the image wavefunction, ψ_i, as shown in equation 2.3 for both real and reciprocal space. Note that for a phase object where the object wavefunction is transferred perfectly into the image wavefunction, the contrast would be zero.

$$c(\mathbf{x}) = \psi_i\psi_i^* \Rightarrow C(\mathbf{k}) = \mathcal{F}c(\mathbf{x}) = \Psi_i \star \Psi_i^* \tag{2.3}$$

The convolution of the image wavefunction with its conjugate in reciprocal space can be simplified in the case of a weak phase object, where most of the intensity remains

in the direct beam. In that case it is sufficient to consider only the interference between the direct beam and the scattered beams, ignoring any contribution from interference between two or more of the scattered beams. This reduces the convolution integral to a sum and is therefore called the *linear imaging approximation*. The image wavefunction can now be expressed as the object wavefunction multiplied by a transmission coefficient, T, which describes the phase change – caused by the lens aberrations – of the scattered beam relative to the direct beam. The change in phase can in turn be expressed in terms of wavelengths, $\chi(\mathbf{k})$, and will depend on the reciprocal coordinate of the scattered beam as shown in equation 2.4.

$$\begin{aligned} C(\mathbf{k}) &= \delta + \Psi_{o,s}(\mathbf{k})\,T(\mathbf{k}) + \Psi^*_{o,s}(-\mathbf{k})\,T^*(-\mathbf{k}) \\ &= \delta + \Psi_{o,s}(\mathbf{k}) \exp\left[i\chi(\mathbf{k})\right] + \Psi^*_{o,s}(-\mathbf{k}) \exp\left[-i\chi(-\mathbf{k})\right] \end{aligned} \tag{2.4}$$

By noting that the scattered beams as described by the weak phase object approximation are conjugate anti-symmetric, $\Psi_{o,s}(\mathbf{k}) = -\Psi^*_{o,s}(-\mathbf{k})$, the expression can be simplified according to equation 2.5.

$$\begin{aligned} C(\mathbf{k}) &= \delta + \Psi_{o,s}\left(\exp\left[i\chi(\mathbf{k})\right] - \exp\left[-i\chi(-\mathbf{k})\right]\right) \\ &= \delta + \Psi_{o,s}\left[\cos\chi(\mathbf{k}) + i\sin\chi(\mathbf{k}) - \cos\chi(-\mathbf{k}) + i\sin\chi(-\mathbf{k})\right] \end{aligned} \tag{2.5}$$

The aberrations causing χ are either even functions, $\chi(\mathbf{k}) = \chi(-\mathbf{k})$, or odd functions, $\chi(\mathbf{k}) = -\chi(-\mathbf{k})$. In either case the cos terms disappear. In equation 2.6 the final form of the expression is derived by substituting the weak phase object approximation for $\Psi_{o,s}$ according to equation 2.2.

$$C(\mathbf{k}) = \delta + \Psi_{o,s} 2i \sin\chi(\mathbf{k}) = \delta + 2\sigma V_t(\mathbf{k}) \sin\chi(\mathbf{k}) \tag{2.6}$$

The $\sin\chi$ term is called the phase contrast transfer function (pCTF) and describes how phase information in the object wavefunction is transferred to image contrast for a *weak phase object* and *linear imaging* conditions. Equation 2.6 shows that by setting the aberrations to $\chi = -\pi/2$ the $\sin\chi$ term becomes -1, resulting in the full transfer of V_t – which is related to the atomic positions in your sample – to the contrast in the image. In this way the aberrations are not exclusively detrimental to your images, but are also essential for generating contrast from phase objects.

Aberrations

The aberrations are usually given as the distance the wave front is displaced, W, which is called the wave aberration function. This function is related to the previously used χ

Table 2.1: The wave aberration function with terms up to fourth order in $\mathbf{k}$.

$W(\lambda\mathbf{k}) = \Re\{$	$A_0\lambda\mathbf{k}^*$	Image shift
	$+\frac{1}{2}A_1\lambda^2\mathbf{k}^{*2}$	Twofold astigmatism
	$+\frac{1}{2}C_1\lambda^2\mathbf{k}^*\mathbf{k}$	Defocus
	$+\frac{1}{3}A_2\lambda^3\mathbf{k}^{*3}$	Threefold astigmatism
	$+\frac{1}{3}B_2\lambda^3\mathbf{k}^{*2}\mathbf{k}$	Axial coma
	$+\frac{1}{4}A_3\lambda^4\mathbf{k}^{*4}$	Fourfold astigmatism
	$+\frac{1}{4}S_3\lambda^4\mathbf{k}^{*3}\mathbf{k}$	Axial star
	$+\frac{1}{4}C_3\lambda^4\mathbf{k}^{*2}\mathbf{k}^2\ \}$	Spherical aberration

by a factor of $2\pi/\lambda$, and is generally dependent on both the position, $\mathbf{x}$, on the sample and the scattering angle, $\boldsymbol{\omega}$. However, since only small areas are imaged at a time in HRTEM the dependence on $\mathbf{x}$ can usually be ignored (known as the *isoplanatic approximation*). The scattering angle can be converted to a reciprocal coordinate using the electron wavelength, λ, according to $\boldsymbol{\omega} = \lambda\mathbf{k}$. In table 2.1 the wave aberration function is shown with all terms up to fourth order in $\mathbf{k}$.[17, 19] Here the wave aberration function is given as the real part ($\Re$) of a complex expression for brevity.

For microscopes without an aberration corrector we can usually ignore all aberrations except defocus C_1, twofold astigmatism A_1, and spherical aberration, C_3. Twofold astigmatism causes a smearing of the image in one direction, but can be compensated by stigmator coils which provide a counteracting effect. Spherical aberration on the other hand is unavoidable in round magnetic lenses and causes high angle rays to be focused closer to the lens than lower angle rays.[20] Keeping only defocus and spherical aberration and substituting the scalar spatial frequency k for the complex reciprocal vector $\mathbf{k}$ (since both C_1 and C_3 are rotationally symmetric) the wave aberration function is reduced to the expression in equation 2.7.

$$\chi(k) = \frac{2\pi}{\lambda}W(k) = 2\pi\left[\frac{1}{4}\lambda^3 C_3 k^4 + \frac{1}{2}\lambda C_1 k^2\right] \tag{2.7}$$

By setting the defocus to a negative value it is possible to offset the effects from the large positive spherical aberration and get the correct phase shift for a large set of k. Figure 2.2a shows $\sin\chi$ for a 300 kV microscope with $C_3 = 0.6$ mm (corresponding to the JEOL 3000F) for $C_2 = -42$ nm, which provides the optimal balance between the two aberrations. At this defocus there is a large range of spatial frequencies up to

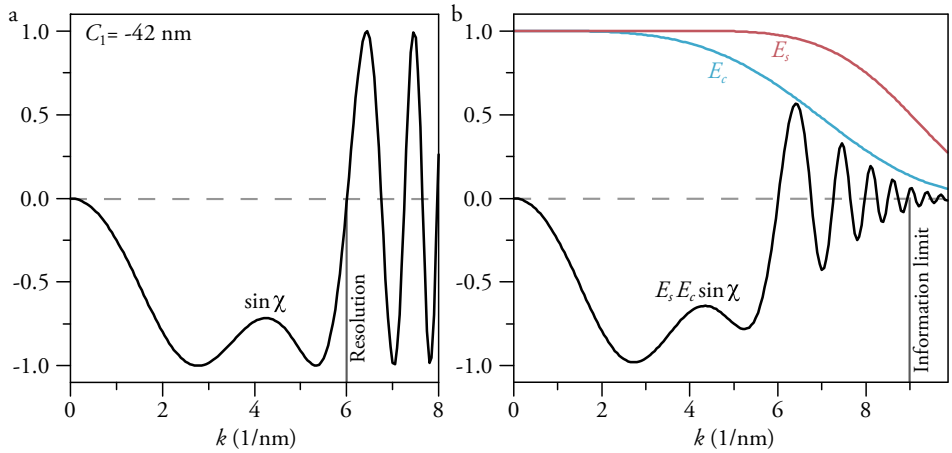

Figure 2.2: (a) Phase contrast transfer function for the optimum defocus which shows a large band of equal transfer up to about 6 nm^{-1}, which defines the maximum resolution of 0.17 nm. (b) Same as in (a), but including the effects of limited coherence of the illumination. The parameters were chosen to match a JEOL 3000F: 300 kV acceleration voltage, C_3 = 0.6 mm, ΔC_1 = 4 nm, and α = 0.2 mrad.

6 nm^{-1} where the phase information in the object wavefunction is transmitted correctly to the image, which defines the point resolution of 0.17 nm.

After the phase contrast function crosses the k axis the first time the spherical aberration will again dominate and as a result the function oscillates. This results in an out-of-phase transfer of the higher spatial frequencies (that is the smaller distances in real space) making the image difficult to interpret. In normal HRTEM this problem is reduced by inserting an objective aperture, which hinders all spatial frequencies above some k from contributing to the image, ideally allowing only the correctly transferred frequencies through.

At high spatial frequencies the phase contrast transfer function is dampened by the limited coherence of the illumination. The energy spread of the gun and small fluctuations in the acceleration voltage result in some variations in the energy of the electrons in the illumination. Electrons with different energies will be focused differently by the objective lens due to its large chromatic aberration. The strength of the lens itself will also fluctuate slightly over time due to small variations in the lens currents. Together, these effects result in a defocus spread, ΔC_1, of a few nanometres instead of a single defocus value. In addition, the electrons originate from a small area on the gun rather than a single point, which means that there is always a distribution of different illumination directions characterized by the convergence semi-angle α. These variations in the illumination are then summed incoherently in the image, which averages away the most rapidly varying parts of the contrast transfer function. In effect the contrast

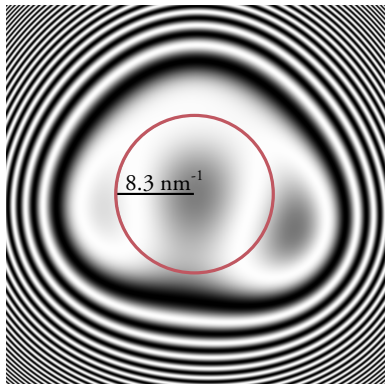

Figure 2.3: $\sin\chi$ after tuning the aberration corrector on the 200 kV JEOL 2200MCO.

transfer function is dampened by two factors, E_c and E_s, related to the variations in defocus and illumination direction respectively according to equations 2.8 and 2.9.

The effect of the dampening functions are shown in figure 2.2b for reasonable values for the JEOL 3000F. It can be seen that E_c causes the ultimate limit to resolution by eventually reducing the contrast transfer below the noise level. This limit is called the information limit of the microscope.[15] It should be noted that variations in the specimen during the image acquisition will also result in the incoherent summation of the different configurations. Because of this, additional envelope functions for specimen vibration and drift can be added.[21]

$$E_c(k) = \exp\left[-\frac{1}{2}(\pi\Delta C_1)^2 k^4\right] \qquad \left(\text{from } \frac{\partial\chi}{\partial C_1}\right) \qquad (2.8)$$

$$E_s(k) = \exp\left[-\left(\frac{\pi\alpha}{\lambda}\right)^2 \left(C_3\lambda^3 k^3 + \lambda C_1\right)^2\right] \qquad \left(\text{from } \frac{\partial\chi}{\partial k}\right) \qquad (2.9)$$

The assumption that only defocus and spherical aberration will contribute to χ is not correct at resolutions approaching 0.1 nm. Here even the smaller aberrations will have significant effects and the wave aberration function is no longer rotationally symmetric. The full $\sin\chi$ for an aberration corrected microscope at optimum defocus is illustrated as a 2D image in figure 2.3 together with the resolution limit imposed by the sum of all aberrations.

Image Simulation

The image formation theory as outlined earlier also serves as the basis for simulating TEM images. The first step in such simulations is to calculate how the incoming electron wave interacts with an atomic model of the sample to become the object wavefunc-

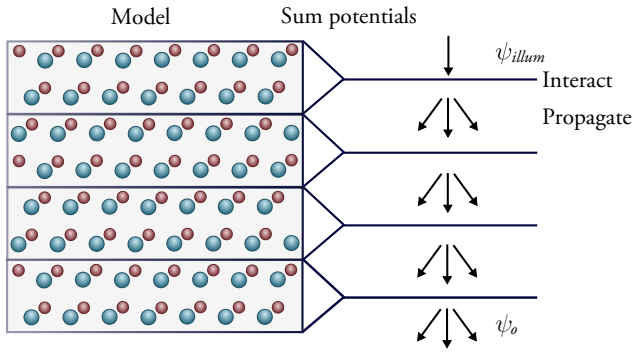

Figure 2.4: Principle steps in the simulation of TEM images by the multislice method. A model structure is cut into thin slices perpendicular to the electron wave, each thin enough for the weak phase object approximation to hold. The electron wave interacts with a slice, followed by free space propagation to the next until it has passed through the entire structure.

tion. For perfect crystals this interaction can be calculated exactly from the Schrödinger equation based on the symmetry and periodicity of the electrostatic potential. This method is called the Bloch wave method. For TEM we are often interested not in the perfect crystal lattice, but rather in the local deviations and defects in this lattice, which limits the use of this method.

An alternative, more widely used, method is instead based on slicing the model atomic structure into thin slices orthogonal to the electron beam. If each slice is sufficiently thin (commonly on the order of 0.2 nm) the weak phase object approximation holds for the individual slices, even if it does not for the structure as a whole, and a projected potential model can be used. After each interaction of the electron wave with the projected potential of a slice the wave is subject to free space propagation to reach the next slice. In this way the object wavefunction is generated after the electron wave has interacted with each slice of the model.[22] This calculation is called the multislice method. The term "multislice" is appropriate as even for a relatively thin nanowire structure several hundreds of slices might be needed. The concept behind multislice simulations is illustrated in figure 2.4.

Simulated and experimental images can be compared in terms of intensity, contrast and pattern. While patterns can be readily matched, contrast is usually much larger in simulated images by as much as a factor of three.[23] There is no one good candidate for this discrepancy, but possible candidates include: scattering in the camera and scintillator,[24, 25] many small errors, e.g. from amorphous layers and inelastic scattering, together with errors in the modelling of the imaging system,[26] or thermal diffuse scattering due to the atoms vibrating around their lattice positions.[27]

2.3 Aberration Correction

Two methods of aberration correction have been used for the studies reported in this thesis: hardware correction and focal series reconstruction. With hardware correction the aberrations of the round objective lens are compensated by additional non-round lenses. By tuning the relative strength of these lenses it is possible to achieve a phase contrast transfer function without reversals up to the information limit of the microscope.[28] Focal series reconstruction instead aims first to recover the complex image wavefunction containing both phase and amplitude information, and then to correct the phase and amplitude changes to get the object wavefunction. This is fundamentally different from hardware aberration correction which still results in normal phase contrast images, albeit with much smaller (but not zero) aberrations than in conventional HRTEM. The drawback is that focal series reconstruction is an off-line method, requiring the processing of several images recorded with different defocus in order to arrive at an aberration-free object wavefunction.

The hardware and focal series reconstruction methods benefit from being used together. Hardware aberration correction typically measures and minimizes high order aberrations not accessible to focal series reconstruction. The low aberrations also minimize the delocalization and the dampening of the contrast caused by the variations in illumination direction. The latter point can be seen directly in the expression for E_s in equation 2.9 which includes both C_1 and C_3. Focal series reconstruction on the other hand removes the remaining aberrations at the site of interest and corrects for amplitude dampening in the phase contrast transfer function.[17, 29]

There are more methods available for aberration correction than the ones mentioned above. Electron holography can also be used to recover the image wavefunction, which can be corrected just as for focal series reconstruction.[20] Tilt series reconstruction is very similar to focal series reconstruction, but uses varying illumination tilts in addition to varying defocus. Since tilting the illumination shifts the temporal coherency envelope it is possible to exceed the information limit using this method, but it requires a very thin sample and is more difficult to carry out.[30] Regardless of which method is used the first step is to measure the aberrations accurately.

Measuring the Aberrations

The even aberrations can be measured directly from images of an amorphous object, such as the carbon support film on the grids. Amorphous objects have a wide and continuous distribution of spatial frequencies, which makes the zero-valued parts of the phase contrast transfer function directly visible as dark rings in the image Fourier transform (also called the diffractogram). The spacing of these rings is related to defocus and spherical aberration, while any deviation from a circular shape is related to twofold astig-

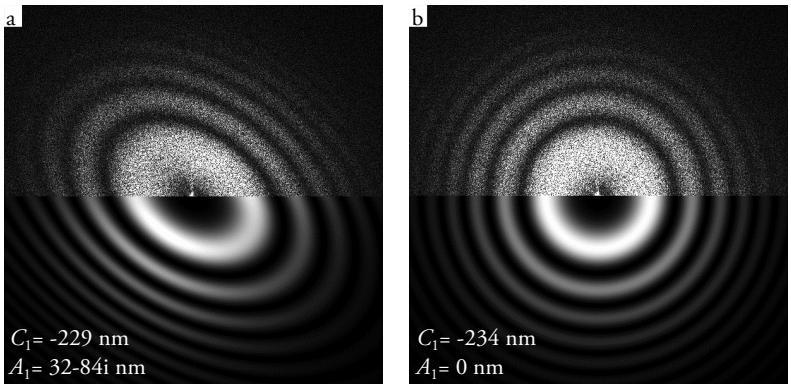

Figure 2.5: Experimental diffractogram of amorphous carbon (top) matched with simulated phase contrast transfer functions (bottom) for a 300 kV TEM with C_3 = 0.6 mm. (a) With twofold astigmatism, and (b) with only defocus.

matism. In this way the diffractograms can be directly matched to the phase contrast transfer function. Such a matching is illustrated in figure 2.5.

In order to achieve resolutions approaching 0.1 nm it is important to also measure the odd aberrations. By tilting the beam the origin of the wave aberration function is shifted and higher order aberrations will induce additional defocus and twofold astigmatism. By measuring defocus and twofold astigmatism for a series of different beam tilts, all aberrations present under axial illumination can be determined. Such a tableau of diffractograms of an amorphous object recorded with varying beam tilts is called a Zemlin tableau.[31] This method is implemented in the alignment routine of the CEOS imaging aberration corrector on the JEOL 2200MCO.[32]

The method described above requires a purely amorphous object while the typical sample is crystalline with only a thin layer of amorphous material on top or nearby. To avoid having the aberration measurement dominated by the few, but very intense, crystalline diffraction spots it is possible to use only the diffractogram phase. By matching the diffractogram phase with the phase from the phase contrast transfer function calculated for various aberration coefficients, it is possible to measure the aberrations even from almost purely crystalline areas. Matching with calculated patterns does however take more time than measuring the aberrations directly and is used only in post processing of images.[33, 34]

Hardware Correction

Round magnetic lenses always have a positive spherical aberration, which is the single largest contributor to the wave aberration function. With hardware aberration correctors extra multipole lenses, which do not have this constraint, are added to the micro-

scope. In this way the total spherical aberration of the objective lens and aberration corrector can be tuned by making the two add up to either a small positive or negative value.[35]

For the purpose of image formation the same equations apply as for uncorrected microscopes, only using lower coefficients for the aberrations. The largest difference is that with an aberration corrector the spherical aberration, in addition to the defocus, is accessible to the user and needs to be set to some optimal value. There are many suggestions in the literature as to how the optimum conditions for C_3 and C_1 should be defined: they can be set to compensate for the uncorrected fifth order spherical aberration (C_5),[36] to make the first crossover of the optimum resolution correspond to the information limit,[36] or to minimize the contrast delocalization up to the desired resolution.[37] The differences between these proposed optimum conditions are however mainly in the sub 0.1 nm resolution range.

A more important distinction for the resolutions used in this thesis is between positive and negative spherical aberration, used together with a negative or positive defocus respectively. For negative spherical aberration the phase contrast transfer function results in bright contrast at the positions of the atomic columns (with a total phase shift of 0), instead of dark contrast (with a total phase shift of π). This difference becomes important when considering samples where the weak phase object approximation is not valid, which is almost all samples of realistic thicknesses. The image will then contain non-linear interferences between the scattered beams in addition to the linear term. For normal, positive C_3 the non-linear contrast will subtract from the linear contrast (which provide the structure information), while in the negative C_3 case they will add.[38] This is particularly advantageous when imaging light atom columns in the vicinity of heavy atom columns, such as oxygen in metal oxides.[39, 40] It is however still important to simulate images for the particular conditions in your sample, as there is no guarantee even with negative C_3 that the structure will be represented in a directly interpretable way in the images.

Image Series Reconstruction

The aim of image series reconstruction is to find the complex object wavefunction, given a set of images and their aberrations. As suggested by equation 2.3 the relationship between image and object wavefunction is quite complicated in the full treatment of image formation, making iterative methods necessary. In the linear imaging approximation on the other hand the object wavefunction can be directly approximated from the images. Comparisons between the two classes of methods show that the phase of the object wavefunction can be retrieved by the linear method as long as the non-linear contributions to the image are small, but that the amplitude in addition requires that most intensity remains in the direct beam. For Si [110] this gives a limit of 14 nm for phase but only 4 nm for amplitude.[41] Simulations for GaAs indicate that the major

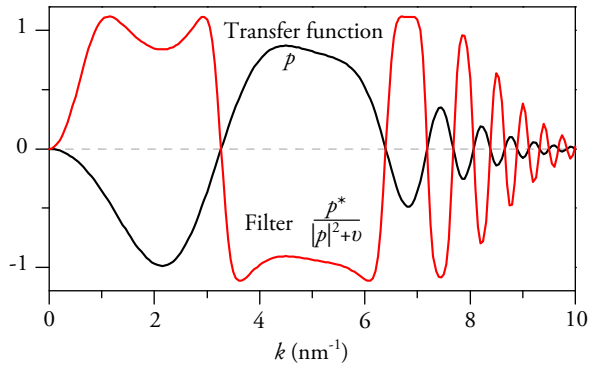

Figure 2.6: Phase contrast transfer function and corresponding Wiener filter for a single image with transfer function p. When applied the filter will correct the phase (due to p^*) and amplitude (due to $1/|p|^2$) of the transfer function, without amplifying noise from the regions with little or no information transfer (due to the noise reduction term ν).

improvement in using a full non-linear method to the reconstructed object wavefunction lies in the treatment of the amplitude.[42]

The solution for linear imaging can be derived in many different, but equivalent, ways.[43] The reconstructions presented in this thesis have been calculated using a Wiener filter based method applied to a series of images recorded at different defocus.[33] In this case the object wavefunction is estimated by multiplying the Fourier transform of each image in the series by a filter and then inverse transforming the sum of all such filtered diffractograms. The filter for each image is based on both the aberrations in the particular image and on the aberrations in all other images in the series. Figure 2.6 illustrates this approach for a single image. The filter can be described qualitatively as follows: for a Fourier component that is transferred in some of the images in the series, the filter simply averages them and corrects any phase change. If instead a Fourier component is not transferred in any of the images (or only transferred very weakly), the filter approaches zero in order to reduce the noise. A full description of the filter function is given by Meyer et al.[33] For a single image this function becomes much simpler, as can be seen from figure 2.6 where the filter function only contains the transfer function of the single image, p, and a noise term, υ. The dampening of the phase contrast transfer function at high spatial frequencies by the defocus spread sets the ultimate limit for focal series reconstruction.

2.4 Scanning Transmission Electron Microscopy

In scanning transmission electron microscopy (STEM) the illumination system forms a small probe on the sample from a convergent electron beam, rather than illuminating

the whole imaged region simultaneously with a broad, parallel beam as in TEM. The electron beam is then scanned over the sample, generating the image sequentially by measuring some signal for each probe position, as illustrated in figure 2.7a. The resolution in STEM is dependent on the size of the probe generated by the illumination system, how much the electrons are scattered in the sample, and how the measured signal is generated, as in some cases the signal can be delocalized to include areas outside the probe.[15] The size of the probe is ultimately limited by the aberrations of the probe-forming lens which can be corrected by additional multipole lenses in a hardware aberration corrector, similar to TEM.[20]

The transmitted electrons are one source of signal used for imaging in STEM. Figure 2.7a illustrates three detectors covering different parts of the diffraction pattern generated by the sample. As the sample is illuminated with a convergent beam the diffraction pattern contains discs rather than spots as in TEM. The bright field (BF) detector collects the direct beam, while the annular dark field detectors (ADF) collect either diffracted beams or electrons scattered to high angles (high angle annular dark field, HAADF).[15]

STEM bright field images are completely analogous to conventional TEM bright field images.[44] There are however two areas where STEM has advantages over TEM. The first is HAADF imaging which uses an annular detector with a large central opening to allow all the direct and diffracted beams to pass through, detecting only the electrons that have been scattered to high angles. Scattering to such high angles, typically above about 50 mrad for 300 kV electrons, is dominated by incoherent thermal diffuse scattering which depends primarily on the thickness and atomic number (Z) of the material. The incoherent, Z-dependent nature of the HAADF signal results in a linear response to thickness over a large thickness range, a contrast related to the composition of the sample, and contrast transfer without inversions.[45]

The second advantage with STEM over TEM is that various spectroscopies can be performed at each position of the probe, enabling spatially resolved compositional analysis, in addition to the electron image. Spectrum imaging, where a full spectrum is recorded at each pixel in an image, in particular shows the benefit of combining STEM and spectroscopy.[46]

2.5 Inelastic Scattering and Analytical TEM

The imaging techniques described so far all rely on elastically scattered electrons, but there are also inelastic processes occurring as the beam passes through the sample. The inset in figure 2.7a shows an example of one such process, in which the incoming electron from the beam transfers enough energy to one of the inner-shell electrons to eject it from the atom in the sample. The electron from the beam continues through the sample with a small deflection having lost only a fraction of its original energy, the ejected

electron ends up either in an unfilled higher energy state or in the vacuum, and the atom itself is left in an excited state. The atom can lose some of the excess energy of the excited state by filling the vacancy in the inner shell with an electron from an outer shell, and in the process emit an X-ray photon or an Auger electron. The energy of the emitted X-ray or Auger electron is determined by the energy difference of the shells involved (of the order of 10^2–10^4 eV) and is characteristic for each element. Auger electrons are generated primarily by the lighter elements and few electron microscopes are equipped with detectors to make use of them.

The process described above is the main source of signal used for elemental identification and quantification in TEM, but there are also several non-ionizing interactions occurring. The incoming electrons can cause the struck atoms to vibrate in the lattice, generating what is known as a phonon (of the order of 1 eV), in effect heating the sample. Another possibility is to create oscillations in the electron density, so called plasmons (of the order of 10 eV). The energy absorbed by the plasmons depends on the density of the free or weakly bound electrons that oscillate, which is material dependent and can in some circumstances be used for compositional analysis.[47]

The inelastic interactions described above are important for generating signals for compositional analysis but the energy deposited in the sample can also be damaging. Depending on the acceleration voltage some atoms of some elements can be knocked out of the lattice entirely causing so-called knock-on damage. The ionization described earlier can also cause radiolysis damage by changing the structure, with the exact mechanism varying from material to material. Typically knock-on damage increases with increasing acceleration voltage while radiolysis damage decreases.[48]

Energy Dispersive X-ray Spectroscopy

Perhaps the most common method for compositional analysis in electron microscopy is to make use of the characteristic X-rays emitted from the sample. The energy of the individual X-ray photons can be measured using an energy dispersive X-ray spectrometer in which the X-rays generate a number proportional to their energy of electron-hole pairs in a semiconductor. The two most common detector types for energy dispersive X-ray spectroscopy (XEDS), Si(Li) and silicon drift detectors (SDDs), both use silicon but differ in the way the generated signal is read out.[15] The differences between the two are not important for the characterizations reported in this thesis and the two types of detectors have both been used. However, in practice the higher output count rates of the SDDs make them much nicer to work with.

An example EDX spectrum is shown in figure 2.7b. It has been labelled to show the origin of the peaks, both in terms of the element and of the shell from which the electron was originally ejected. The ratio of the intensities for the peaks from the different elements is related to their relative prevalence in the irradiated volume, which allows quantitative analysis to be made. The exact relationship between intensities and com-

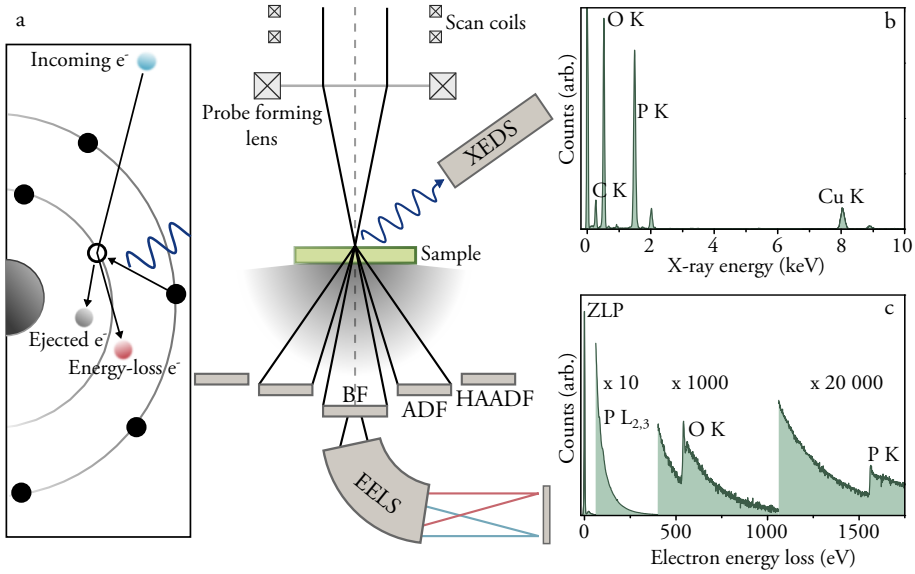

Figure 2.7: (a) Principle behind scanning transmission electron microscopy (STEM), where the electron beam is focused to a small probe which is scanned across the sample. Images can be generated from electrons scattered to the bright field (BF), annular dark field (ADF) or high angle annular dark field (HAADF) detectors. The fast primary electron can undergo inelastic scattering in the material, and in the process lose some of its energy, which can generate characteristic X-rays as shown in the inset. Example energy dispersive X-ray (EDX) spectrum (b) and electron energy loss (EEL) spectrum (c) are shown. In the EEL spectrum, note the large reduction in intensity with increasing energy loss, and that the P $L_{2,3}$ edge can only barely be seen due to the large background from the plasmon peak.

position varies from system to system (due to different detector efficiencies, absorption from the thin windows protecting the detector etc.) and is provided by the manufacturer or measured from standards with known composition. Nanowires are a special case for quantitative XEDS in one regard: they are often analysed when viewed perpendicular to their long axis. In this orientation at least one set of (111) planes are parallel with the beam and thus strongly diffracting. Under such strongly diffracting conditions the electrons can be channelled along certain atomic planes which will contribute more to the inelastic signal than expected under non-channelling conditions. This effect is strong enough to change the apparent ratio between elements occupying different planes in the crystal, such as the group III and V atoms in the III-V materials.[15]

The spatial resolution is limited by the size of the electron beam as it passes through the sample, which in turn depends on the size of the incident beam and how much it is broadened by scattering in the sample. Assuming single scattering, this can be estimated to be on the order of 2 nm at best in 50 nm thick InP.[49]

The minimum detectable fraction of an element by XEDS is somewhere around 0.5–1 at%. This might seem not very sensitive, but since only a small volume of atoms is analysed this can correspond to detecting only a few of atoms. The detection limit of course depends on the current in the probe and collection time, as the signal to noise ratio will increase with an increasing number of counts. This comes at the expense of having a larger probe and damaging the sample more. The thickness of the sample also matters: for a sufficiently thin sample the small volume through which the probe passes might not even contain any of the trace elements.[15]

Electron Energy Loss Spectroscopy

The energy-loss electrons can also be used for compositional analysis. Compared to the X-rays discussed previously the energy-loss electrons also carry information about non-ionizing events and more detailed information about the ionizing processes. In electron energy loss spectroscopy (EELS) the electrons are sorted according to their energy by a magnetic prism. The energy-loss electrons are slower and therefore deflected more by the prism than the electrons that have not lost energy to the sample, and so the electrons are dispersed according to their energy onto a CCD detector.

An example electron energy loss (EEL) spectrum is shown in figure 2.7c. Note that the scale going from 0–2000 eV energy loss corresponds to electrons having 300000–298000 eV kinetic energy in this case. Most electrons do not lose energy to the sample, or only excite low energy phonons, and so end up in the zero-loss peak (ZLP). The full width half maximum (FWHM) of the ZLP is about 1 eV and indicates the maximum energy resolution that can be achieved on this particular microscope. A much smaller number of electrons excited plasmons in this sample, indicating that it is very thin, as can be seen from the small plasmon peak at around 20 eV. Fewer electrons still managed to eject inner shell electrons from the atoms in the sample and so the regions containing the P $L_{2,3}$, O K, and P K edges caused by such events are all displayed on different intensity scales compared to the ZLP. The edge, rather than peak, shape of these core-losses is due to there being a minimum energy needed to cause the ionization, but larger losses can be accommodated by simply transferring more kinetic energy to the ejected electron. The exact shape of the edge depends on the empty states which are available to accept the ejected electron, and these can vary depending on the bonding and oxidation state of the atom.

All of the core loss edges sit on top of a large, decaying background caused by electrons undergoing a multitude of various low loss processes. In addition it is possible for core-loss electrons to undergo further inelastic processes, which convolutes the spectrum. These effects make quantification more difficult in EELS than in XEDS. The advantage of EELS lies in detecting light elements with low X-ray yields, the additional information contained in the edges, and the possibility to detect non-ionizing processes.[15]

Chapter 3

Growth of III-V Nanowires

Complex semiconductor structures, such as nanowires, are often synthesized using the crystal structure of a substrate as a template for the addition (or growth) of new material in a process known as epitaxy. If the same material as the substrate is added (homoepitaxy) the growth will ideally continue with the same crystal structure and direction as the substrate, forming a single crystal. If a different material than the substrate is added (heteroepitaxy) the same guiding principle can still work, as long as the two materials are similar enough in terms of crystal structure. This is the case for all III-V and group IV semiconductors and it is therefore possible to combine these materials in epitaxial heterostructures.[50]

There are many different methods for supplying the material for the growth, with vapour phase methods being the most common. These methods can be further divided according to their operating pressure and the chemistry of the growth species. For III-V nanowire growth three methods are mainly used: metalorganic vapour phase epitaxy (MOVPE) performed at moderate pressures with metalorganic precursor species, chemical beam epitaxy (CBE) performed in vacuum with precursor compounds, and molecular beam epitaxy (MBE) performed in vacuum with evaporated pure elements or pre-cracked precursor compounds. At the low pressures used in MBE and CBE the growth species have a free path to the sample without other gaseous species in between, and are therefore transported in a beam rather than by diffusion. All the nanowires presented here were grown using MOVPE with methylated or ethylated group III elements and group V hydrides (with the exception of Sb), transported in a stream of hydrogen. This method will be presented in more detail in the following section, which is focused on the details of the processes by which new material is added to the growing nanowire. There are however many more processes that need to be considered for successful growth than are presented here, such as precursor decomposition and surface diffusion.[51] On top of this, MOVPE is typically carried out with severely toxic and flammable gases.

These complications can be useful to keep in mind if the growth seems simple from the descriptions given in this thesis.

3.1 The Basics of Nanowire Growth by MOVPE

Compared to normal epitaxy of thin films, nanowire growth involves additional complications: how to insure that growth occurs only at certain locations and with the desired shape. The most common method uses nanoparticles as seeds which define the positions and diameters of the growing nanowires. Gold has so far proven the most successful seed particle material for controlled growth, yielding epitaxial nanowires for a wide range of semiconductors and growth conditions.[52] Other foreign metals, such as Cu[53] and Ag[54], have also been used, but have so far only been demonstrated to work for a smaller range of semiconductor materials and growth conditions. Another possibility is to use droplets of the same group III element as in the desired III-V material in so called self-seeded growth.[55, 56] Although gold is to date the most widely used seed particle material, it has the disadvantage of negatively affecting the electronic properties of Si. This effect could potentially also be a problem for III-V nanowires if they are to be integrated with other devices on a silicon substrate.[57] A detailed description of the many methods available for producing gold nanoparticles is given by Messing et al.[52] The nanowires presented in this thesis have all been grown from gold nanoparticles generated by the evaporation/condensation method.

Figure 3.1 gives an overview of the nanoparticle seeded growth process. A substrate with Au seed particles is placed on a susceptor (a) which is heated to the desired temperature under a constant flow of hydrogen carrier gas. In the illustration the substrate has been given another colour than the nanowire to distinguish the two, but for the purpose of this discussion they can be taken to be of the same material. For III-V materials an overpressure of the group V element, commonly supplied as a hydride, is often used during the heating to prevent the decomposition of the substrate material. The metalorganic group III precursor is then introduced to initiate the growth (b). In MOVPE the precursors constitute only a small fraction of the gas mixture supplied to the sample, with the remainder being the hydrogen carrier gas. Using InP as an example, the overall chemical reaction can be written as in equation 3.1.

$$\mathrm{In(CH_3)_3(g) + PH_3(g) \longrightarrow InP(s) + 3\,CH_4(g)} \tag{3.1}$$

In reality the precursors first crack into the pure elements over many steps and dissolve in the seed particle – to various degrees depending on the elements involved – before they precipitate and combine to form the semiconductor material. Not all precursor molecules will however crack completely due to the short contact times with the heated substrate and the relatively low temperatures used during nanowire growth. For this

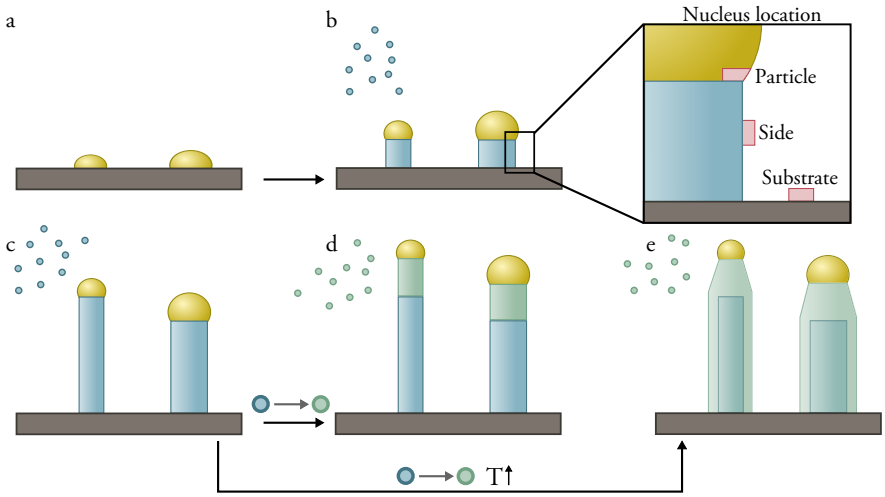

Figure 3.1: Principle behind gold assisted metalorganic vapour phase epitaxy (MOVPE) of nanowires. The substrate with seed nanoparticles is first heated (a). Growth is initiated by supplying metalorganic precursor species (b). The inset shows three alternative locations for forming new crystalline nuclei. Ideally new material is added only underneath the particle until the desired length is reached (c). Axial (d) and radial (e) heterostructures can be formed by exchanging the precursors.

reason, there is a risk in MOVPE growth of incorporating carbon from the remaining organic ligands into the nanowires.[51] Ideally material is only added underneath the gold particles, which therefore determine the diameters and positions of the nanowires, until the desired length is reached (c). By exchanging one or more of the precursors, for instance PH_3 to AsH_3, during the growth it is possible to form axial heterostructures (d). Throughout this thesis such heterostructures are named according to the growth order of the constituent materials. The growth parameters can in addition be tuned to allow the new material to attach preferentially to the nanowire sides, thereby forming a radial heterostructure. In figure 3.1e this is exemplified by an increase in temperature, which makes the growth less selective and under certain circumstances increases the rate of the radial growth. To stop the growth, the group III supply is turned off and the substrate is cooled.

At the growth conditions, the chemical potential of the growth species will be higher in the vapour phase than in the seed particle solution, and higher still than in the crystal. For material nucleating under the seed particle it is the difference in chemical potential, $\Delta\mu$, between the growth species dissolved in the seed particle and incorporated into the crystal which constitute the driving force for the growth. In nanowire growth this chemical potential difference is often directly referred to as the supersaturation, but generally the supersaturation is instead defined as $\Delta\mu/RT$. In order for new material to crystallize

and extend the nanowire a small nucleus must first be formed. Such nuclei consist of a small number of atoms and either rapidly grow into stable bilayers or re-dissolve into the seed particle after forming. It is likely that the nuclei are only a single layer of atoms high and thus have a well-defined height h, but their shape is otherwise unknown. In the following discussion the size of the nucleus is given only by its diameter d and no further assumptions are made about its geometry. By forming a nucleus, the overall free energy of the system will be reduced by the chemical potential difference between the dissolved and solid growth species. This reduction in free energy is however counteracted by an excess interface energy Γ associated with the atoms located at the surface of the nucleus. While the negative contribution from the chemical potential difference scales with the volume of the nucleus, hd^2, the positive contribution from the interface energy scales only with the surface area of the sides of the nucleus, hd. The total change in free energy of the system, ΔG, for forming a nucleus is given by equation 3.2.

$$\Delta G \propto -hd^2\Delta\mu + hd\Gamma \tag{3.2}$$

The fate of a newly formed nucleus depends on whether the free energy is increased or decreased by the addition of more atoms. For a small nucleus a large proportion of its constituent atoms are located at the surface which allows the interface energy term to dominate. Expanding the nucleus would in this case increase the free energy, and so the nucleus most likely dissolves instead. At some critical size, d^*, the chemical potential difference will however become dominant and more atoms will attach to the growing nucleus until a new layer has formed. This critical nucleus size can be found by setting the derivative of ΔG with respects to d to zero. At the critical size the free energy of the nucleus will reach its maximum, ΔG^*, which constitutes the free energy barrier for nucleation. The critical size and nucleation barrier for the nucleus defined in equation 3.2 are given by equation 3.3.

$$d^* \propto \frac{\Gamma}{\Delta\mu}\ ,\ \Delta G^* = \Delta G(d^*) \propto \frac{\Gamma^2}{\Delta\mu} \tag{3.3}$$

The following discussion of how nucleation relates to nanowire growth is adapted and simplified from Wacaser et al.[58] In the inset in figure 3.1b three possible nucleation sites are shown, each with distinctly different surfaces. Note that only the surfaces on the sides of the nucleus enter into Γ in homoepitaxy, as the top surface simply replaces the surface underneath the nucleus. As interfaces between solid and liquid phases generally have lower energy than interfaces between solid and vapour phases, Γ is lower for a nucleus underneath the particle than for nuclei on either of the bare surfaces. Consequently the critical nucleus size is smaller underneath the particle and stable nuclei will form there at a much higher rate than on the bare surfaces. Increasing the temperature

increases the rates at which nuclei form at all three locations and reduces the difference between them. However, as the nanowire sides and substrate surface are much larger and provide many more potential locations for nuclei to form, growth at these locations will eventually dominate over axial growth underneath the gold particle. It is important to keep in mind that the material nucleates under different conditions on the nanowire sides compared to underneath the gold particle. For this reason ternary compounds can potentially form with different compositions, and dopants incorporate at different concentrations, in the radially and axially grown material.

The growth of new layers underneath the seed particle from small nuclei has actually been observed live by *in-situ* TEM. Generally it is favourable for material to add to an existing growing layer rather than to form a new nucleus nearby, as the energy barrier is much lower for adding material at a step site than for forming a nucleus on a flat surface. In this way the step formed by the nucleus at the growth front will spread to cover the interface between the particle and nanowire before the next nucleus is formed.[59–61] This model for nanowire growth is however not complete, which is clearly demonstrated by more recent *in-situ* TEM experiments where the dynamics of the growth front have been examined in detail. These experiments have shown that the growth front does not consist of a single, stable facet but in addition has small inclined facets at the perimeter. Material was continuously added to these smaller facets until the growth front became almost flat. At that point some of the material at the perimeter was dissolved and a new layer nucleated on the large top facet. In the process the inclined facets reformed, which allowed the process to start over again.[62–64]

Aerotaxy

The substrate based method described in the previous section would be difficult and expensive to scale up for the industrial production of nanowires. The main drawbacks for this method are that it is a batch process which necessarily involves down-time between the growth runs, and that it requires costly 300 µm thick substrates to support an active layer of nanowires about 10 µm thick at most. This inefficient use of time and material needs to be addressed, particularly for applications requiring large areas to be covered.

In paper V a new method called aerotaxy is described which is similar to normal MOVPE growth, but is in principle continuous and does not use a substrate during the growth process. The aerotaxy concept is illustrated in figure 3.2. First, an aerosol of size selected gold particles is generated in the same way that seed particles are generated for the standard epitaxial growth method discussed in the previous section. Gold vapour is condensed into agglomerates of primary particles (a), which are then size selected (b) according to their mobility in an electric field in a differential mobility analyser (DMA). The now uniformly-sized agglomerates are then compacted into spherical particles in an oven (c). The nanowire growth takes place in a second oven where metalorganic precursors, the same as for the standard growth, are mixed into the gas stream (d).

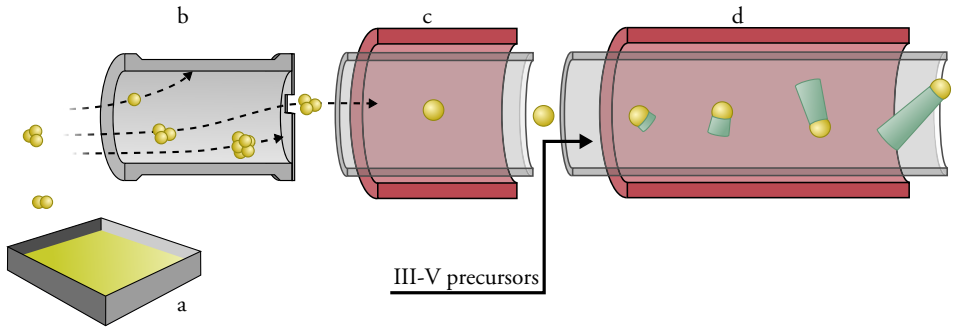

Figure 3.2: The aerotaxy concept. Gold agglomerates are generated by condensing a gold vapour (a), size selected according to their mobility in an electric field (b), and compacted into spherical particles in an oven (c). In a second oven MOVPE precursors are added to the gas stream and nanowires form from the gold particles in flight (d).

During their approximately 1 s residence time in this oven, a nanowire of the order of 1 µm in length is formed from each gold nanoparticle. This makes the average growth rate 20–1000 times larger than in the standard growth method. The nanowire aerosol formed at the end of this process can then be deposited onto any substrate with no requirements on crystallinity. Depending on the application the nanowires may need to be oriented in specific directions and arranged into patterns, but that is not a subject for this thesis.

The very start of the growth in aerotaxy differs from the standard growth in that there is no substrate to provide a preferential nucleation site and epitaxial guidance for the crystal structure. The initial lack of a site for nucleation will increase the nucleation barrier, but once a stable nucleus has formed further material can be added to it with no extra penalty compared to normal nanowire growth. In the early stages of the growth when the crystallite is small, the gold particle can likely wet or move between several equivalent facets. When one facet becomes large enough to support the particle on its own, the growth can proceed exclusively in the associated direction to form a nanowire.

Paper V describes the growth by aerotaxy of nanowires of a single, undoped material (GaAs) from large enough gold particles that no size effects could be observed. The remaining sections in this chapter on heterostructures, doping, etching, and size effects are therefore based exclusively on nanowires grown epitaxially on substrates. However, as the method is continues to be developed, some of these effects must eventually be considered also in aerotaxy.

3.2 Some Notes on Heterostructures

The growth of nanowires containing two or more different materials in a heterostructure is more complicated than the separate growth of nanowires of the individual materials. As an example, heterostructures often show a tendency to kink, i.e. change growth direction, at the interface when switching materials in one direction but not the other. This effect stems from the additional interface energy which enters equation 3.2 when the nucleus and nanowire are of different materials.[65] Compositional grading constitutes another complication which is the topic of the remainder of this section and is also discussed in both papers III and IV. When exchanging one element for another the corresponding change in nanowire composition is often much slower than the change of the input precursor gases. As a result the change in composition can occur over long lengths in the resulting nanowire. Two factors which can negatively influence the sharpness of the transition between two materials are outlined below.

Reactor memory effects occurs when precursors linger in the reactor after they have been removed from the gas stream. The precursors can for example adsorb to the substrate surface – which has a very large area compared to the nanowire growth fronts – and only slowly desorb to be removed from the reactor by the constant flow of carrier gas. The desorbing species provide a lasting background pressure of that particular element and can be incorporated into the nanowires during later growth stages. For arsenic and phosphorous this is usually not a problem due to their relatively high vapour pressure, which ensures that they are quickly desorbed. Consequently it is possible to fabricate very sharp interfaces between arsenides and phosphides by both CBE[66] and MOVPE.[67] Antimony on the other hand has a much lower vapour pressure and will remain in the reactor much longer after the flow of its precursor is turned off, making it very difficult to achieve sharp transitions from antimonide materials. The main method of reducing this memory effect is to pause the growth for as long as possible in order to allow at least some of the adsorbed species to be removed before the growth continues. The use of this strategy to reduce the unwanted carry-over of Sb to InAs during the growth of GaSb-InAs nanowires is described in paper III.

The reservoir effect stems from the fact that the seed particle in most cases dissolves or alloys with a large amount of the group III elements during growth. This also applies to the group IV elements during the growth of group IV nanowires. The main path for the dissolved atoms to leave the particle is to be incorporated into the crystal. At the time of the precursor exchange, a large amount of the previous element remains dissolved in the seed particle and is only gradually replaced as the growth continues. Note that pausing the growth will usually have little effect as the material remains dissolved even at equilibrium and will not crystallize or evaporate. The group V elements, with the exception of Sb, are dissolved in much smaller amounts and therefore experience much less compositional grading due to the reservoir effect.

For group IV elements dissolved in gold, which behave almost like an ideal solution,

the compositional gradient can be readily predicted. For a nanowire with a diameter d the volume of the reservoir is proportional to d^3 while the cross-sectional area is proportional to d^2, leading to a compositionally graded segment with a length proportional to d.[68, 69] Two or more group III elements dissolved in gold form a non-ideal solution, where the presence of one element significantly affects the solubility of the other. This is for example the case for indium and gallium. Typically the solvent (Au) will have a much higher affinity for one of the solutes (In) than the other (Ga). In one switching direction (from Ga to In) the incoming solute quickly displaces the other, making for a sharp interface, while in the other direction (from In to Ga) the new solute is only slowly dissolved into the particle.[70, 71]

Strategies to reduce the compositional grading from the reservoir effect have been developed by attempting to reduce the solubility of the growth species in the particle. Examples of successful strategies for group IV nanowires include alloying the gold particles with another element in order to grow from solid instead of liquid particles,[72, 73] or choosing a different element for the particle altogether, such as tin.[74] For III-V nanowires the non-ideal solubility of the group III elements in gold can be turned into an advantage by supplying short pulses of one element to reduce the solubility of the other without incorporating the pulsed element into the nanowire.[75]

3.3 Doping and Etching

In order to form working devices the steps described previously in this chapter are often not enough. *Doping*, the controlled addition of small quantities of an impurity to a material, is usually required to modify the electrical properties. Often the growth parameters that result in the desired crystal structure and composition do not yield the desired shape of the nanowire, in which case *etching* might also be needed. Nanowire growth is very sensitive however and any addition to the growth process is likely to have more than one effect.

Doping in the context of III-V semiconductors means replacing a few of the atoms with another element having fewer (an electron acceptor, p-type) or more (an electron donor, n-type) valence electrons than the atom it replaces. This affects the type and availability of charge carriers in the material and is an essential part of turning nanowires into working electronic devices. With nanowires it is desirable to add the dopants during growth in order to create controlled junctions and have a large degree of control over the dopant distribution. In MOVPE growth this means introducing additional precursors during the growth. The amount of dopant that is desired varies a lot with the intended application, but concentrations of 10^{19} cm^{-3} can be used as an example of the order of magnitude. This corresponds to replacing about 1 in 4000 atoms in the material with the dopant atoms. Using *in-situ* doping, p-n junctions in GaAs were reported already in 1992.[76] In this case the dopants were Si from silane (n) and carbon

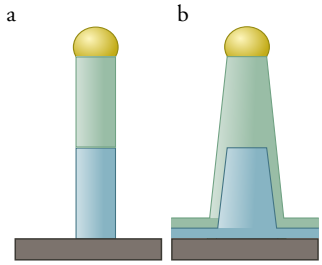

Figure 3.3: (a) Ideal axial heterostructure. (b) Axial heterostructure with unintentional radial growth which can bypass the heterojunction, reducing the performance of any device made from this nanowire.

from the group III precursors (p). Since then many more dopants have been evaluated for many different III-V combinations, see Wallentin et al. for a comprehensive review.[77]

For InP examples of dopants include Zn from diethyl zinc (DEZn) for p-doping,[78] and S from H_2S for n-doping.[79] The crystal structure of the resulting nanowires, which is discussed more in chapter 4 and in papers II and ix, is affected strongly by both H_2S and DEZn, which respectively induce the wurtzite and zincblende crystal structure types. DEZn has a particularly dramatic effect and produces periodically twinned zincblende with {111} side facets if introduced in high enough concentrations.[78] In this case each twin segment has the shape of a truncated octahedron giving the nanowires a "zig-zag" appearance when viewed from certain directions.[80] It is usually difficult to establish the mechanisms behind these effects as there are many parameters involved which might be affected by the introduction of new precursor species, such as surface passivation leading to changed surface diffusion lengths and changed interface energies.

Etching can be used to reduce unwanted radial and substrate growth. Figure 3.3 illustrates the consequences the unwanted growth can have for an axial heterostructure with either two different materials or two different dopings. The material that is incorporated on the sides during the growth of the second segment will form an unintentional shell around the entire nanowire, making it tapered instead of straight. The radial growth provides an alternative route through the nanowire for the charge carriers, bypassing the junction in the middle, which will be hugely detrimental to the device. The radial growth could also be a problem for doped nanowires of a single material if the dopant atoms are incorporated at different concentrations in the axially and radially formed material. This effect might also occur for MOVPE carbon incorporation, which would result in uneven doping even for nominally undoped nanowires of a single material.

Growth parameters can be adjusted to minimize the radial growth, but these might

be fixed or limited due to other demands. The material might, for example, only grow under certain conditions and only have the desired crystal structure under an even narrower set of parameters. *In-situ* etching involves the introduction of a reactive species during growth with the intention that it reacts preferentially with material attached at undesired locations before it becomes fully incorporated into the nanowire. For InP nanowire growth HCl has been successfully used for this purpose, as reported in paper viii. It is important to note that the etchant needs to be introduced during growth in order to create untapered nanowires as only weakly adsorbed (physisorbed) In species on the sides are preferentially removed. Once the material is fully incorporated into the structure (chemisorbed), the selectivity disappears. For this reason HCl etching post-growth does not reduce tapering.[81]

3.4 Size Effects

For many applications it would be beneficial to grow the nanowires as thin as possible. A small diameter could for example produce quantum confinement effects, allow for more efficient gating, and improve the ability of the structure to accommodate the strain at a heterojunction without forming dislocations. A sufficiently small object, such as a thin nanowire or its seed particle, will have a relatively large fraction of its atoms at the surface, which changes its properties compared with a larger but otherwise identical object. For instance, the chemical potential of a material in a particle, and therefore also its vapour pressure, will increase with decreasing particle size. This size effect is particularly problematic for nanowire growth as it can reduce the driving force for transferring growth species from the vapour phase to small seed particles. For sufficiently small particles the driving force is reduced to zero and the growth fails. This effect, known as the Gibbs-Thomson effect, will be derived and discussed in more detail in the remainder of this section.

Two systems both containing particles of phase β, but with different curvatures H (simply $2/d$ for a spherical particle), in equilibrium with their surroundings of phase α are related by the expression in equation 3.4. Here P is the vapour pressure, V is the molar volume with the subscript denoting the corresponding phase, and γ is the interface energy between the two phases.

$$-\left(V^{\alpha} - V^{\beta}\right)\mathrm{d}P + 2\gamma V^{\beta}\mathrm{d}H = 0 \tag{3.4}$$

For liquid or solid particles in contact with gaseous precursors, as during nanowire growth, $V^{\alpha} \gg V^{\beta}$ and $\Delta V \approx V^{\alpha}$. Assuming that the vapour behaves like an ideal gas at the relatively low pressures used during growth, the vapour pressure over the particle P_H can now be related to the vapour pressure over the corresponding bulk material $P_{H=0}$.[82]

$$P_H = P_{H=0} \exp\left(\frac{4\gamma V^\beta}{dRT}\right) \tag{3.5}$$

As can be seen from equation 3.5 above the vapour pressure will increase with decreasing diameter, d. For a dissolved element this equation needs some further modifications in order to take into account the reduced vapour pressure of a solute compared to the pure element. For small fractions of solute $P_{H=0} \approx xP^*_{H=0}$ according to Raoult's law, where x and $P^*_{H=0}$ are the molar fraction and saturation vapour pressure of the pure element respectively.

$$P_H = xP^*_{H=0} \exp\left(\frac{4\gamma V^\beta}{dRT}\right) \tag{3.6}$$

The equilibrium vapour pressure according to equation 3.6 above can now be compared to the actual partial pressure in the MOVPE reactor. The difference between these can be seen as the driving force for the transport of elements from the vapour to the seed particle. Since the operator can only indirectly control the partial pressure of an element by changing the partial pressure of its precursor, this pressure is instead expressed as αP_{MO}. Here P_{MO} is the controllable metalorganic precursor partial pressure and α is a utilization factor which takes into account for instance incomplete cracking. As long as $\alpha P_{\mathrm{MO}} > P_H$ there is a driving force to transport material to the particle.[83] At $\alpha P_{\mathrm{MO}} = P_H$ there is no driving force to supply the nanowire with new material and the growth stops. The critical diameter at which the growth stops can be found from equation 3.6 as shown in equation 3.7 below.

$$d_{crit} = \frac{4\gamma V^\beta}{RT \ln\left(\frac{\alpha P_{\mathrm{MO}}}{xP^*_{H=0}}\right)} \tag{3.7}$$

The solute fraction in the seed particle, x, is likely also affected when changing the precursor partial pressure. The exact relation between x and P_{MO} is not known, but as an approximation a model can be used where x increases linearly with P_{MO} from some equilibrium value, x_{eq}. Note that for the group III elements x_{eq} is likely large compared to the change with P_{MO}, so that x is approximately constant. For InAs for example, post-growth measurements consistently show around 30–40 at% In in the catalyst particle,[84] which is an indication of the high x_{eq}. Consequently, in this case the Gibbs-Thomson model fits well with a constant solute fraction.[85] For antimony on the other hand, the solubility at equilibrium in the Au-III alloy is quite low, and even a small change in solute fraction with the Sb precursor partial pressure could have a significant effect.

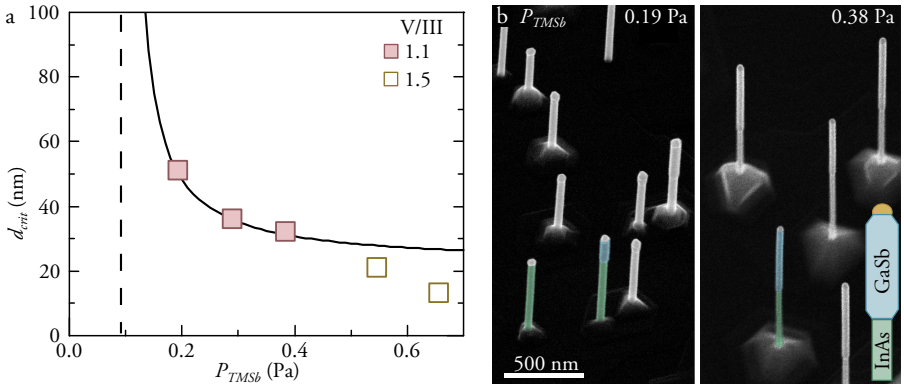

Figure 3.4: Critical diameter for successful growth of GaSb on InAs as a function of trimethyl antimony (TMSb) partial pressure (a). A Gibbs-Thomson model is fitted to the measurements from the growths with a 1.1 ratio between the precursor partial pressures for the group V and group III elements (V/III = 1.1). Note that the model fits well also with the P_{TMSb} = 0.096 Pa sample where no successful growth was observed for any diameter. (b) SEM images[2] of two of the samples from (a), where the presence or lack of GaSb segments can be clearly seen due to the increased diameter for GaSb compared to InAs.

The critical diameter for growing GaSb on InAs stems is shown in figure 3.4a. The reasons for investigating this particular heterostructure, as well as a more detailed discussion of the results, are given in paper IV. For the purpose of the discussion in this section it is sufficient to note that there is a very clear dependence of the critical diameter on the precursor partial pressures. In the example SEM images in figure 3.4b the presence or lack of a GaSb segment for the different diameters can easily be seen due to the GaSb segments having a larger diameter than the stems. The increase in diameter for the GaSb segment has been attributed to an increase in group III content in the seed particle during the growth of antimonides compared to arsenides.[86] The Gibbs-Thomson model in figure 3.4a is fitted only to the three samples grown with a ratio of 1.1 between the group III and V precursor partial pressures (V/III = 1.1). It should however be noted that the model also agrees with a fourth sample, marked by a dotted line in the figure, where no GaSb segments were observed for any diameter. In order to obtain a good fit to the measured critical diameters the Sb fraction in the seed particle is allowed to vary from 2 at% to 5 at% over the precursor partial pressure range.

Extrapolating the Gibbs-Thomson model to higher precursor partial pressures suggests that increasing the precursor partial pressures further will give diminishing returns. Growths at higher precursor partial pressures with V/III = 1.5 do however indicate that there is some room for improvement. The (small) discrepancy between the model and these results could be an effect from fitting to only three points. It is also uncertain

[2]SEM images courtesy of Mattias Borg.

whether the minimum diameters found in these samples really correspond to the critical diameters, as slightly thinner nanowires somewhere else on the substrate could have been overlooked. Another alternative is that the V/III ratio has some effect on the growth, perhaps by influencing the exact relation between the precursor partial pressures and the Sb fraction in the gold particle. Similar effects have been seen for CBE grown InAs-InSb nanowires.[87]

When using these types of models for nanowire growth it is common to use the interface energy and molar volume of the solvent, pure gold, as these are not known for the various alloys that are actually present. With fractions of group III atoms of up to 0.7 (corresponding to growth of GaSb from supersaturated $AuGa_2$ for example) one would expect these properties to differ from pure gold. However, the differences are compensated by the fitted parameters (x and α, which are also not known), allowing quantitative predictions within the specific materials system being analysed.

Comparisons between different materials systems are difficult, as changing the solute can potentially affect the interface energy, molar volume, solute fraction (and its dependence on the precursor partial pressure), and utilization factor simultaneously. The choice of solvent could have similar effects. For III-Sb nanowires both In (i.e. self-seeded growth)[55, 56] and Ag[54] have been shown to yield epitaxial nanowires, but not thin enough to allow an evaluation of the differences between these seed particle materials and gold.

Chapter 4

The Crystal Structure of III-V Materials

The crystal structure types adopted by the semiconductor materials discussed in this thesis are shown in figure 4.1. In bulk all III-V materials adopt the cubic zincblende crystal structure type at normal temperatures and pressures, except the nitrides which instead adopt the hexagonal wurtzite crystal structure type. In nanowires the crystal structure is however often determined by the growth kinetics, and most materials can adopt either of the two crystal structure types. Also shown for comparison is the diamond crystal structure type, adopted by silicon and germanium. In all three crystal structures the atoms have a tetrahedral arrangement, with each atom bonding to four neighbours of the other element (or the same element in the case of Si and Ge).

The similarity between the three crystal structures is most obvious when comparing the zincblende and diamond structure types. Both can be described as two interpenetrating face centred cubic lattices shifted (1/4,1/4,1/4) along the space diagonal with respect to one another. In the diamond structure type the two sub-lattices contain the same element. For zincblende, by convention, the sub-lattice with its origin at (0,0,0) contains the group III element while the sub-lattice with its origin at (1/4,1/4,1/4) contains the group V element. As the two sub-lattices in zincblende do not contain the same elements the centre of symmetry is lost and the structure is non-centrosymmetric. The polar nature of the zincblende structure becomes apparent when comparing the two opposite {111} and $\{\bar{1}\bar{1}\bar{1}\}$ planes: the former is terminated by group III atoms while the latter is terminated by group V atoms. Facets formed from these two planes will have different physical and chemical properties, such as different interface energies and susceptibility to etching. As an example, the two different {111} surfaces of InP differ by 40 % in interface energy.[88] In order to make these differences more apparent the directions and planes terminated by group III atoms often have an A appended, while those terminated by group V atoms are appended with B.

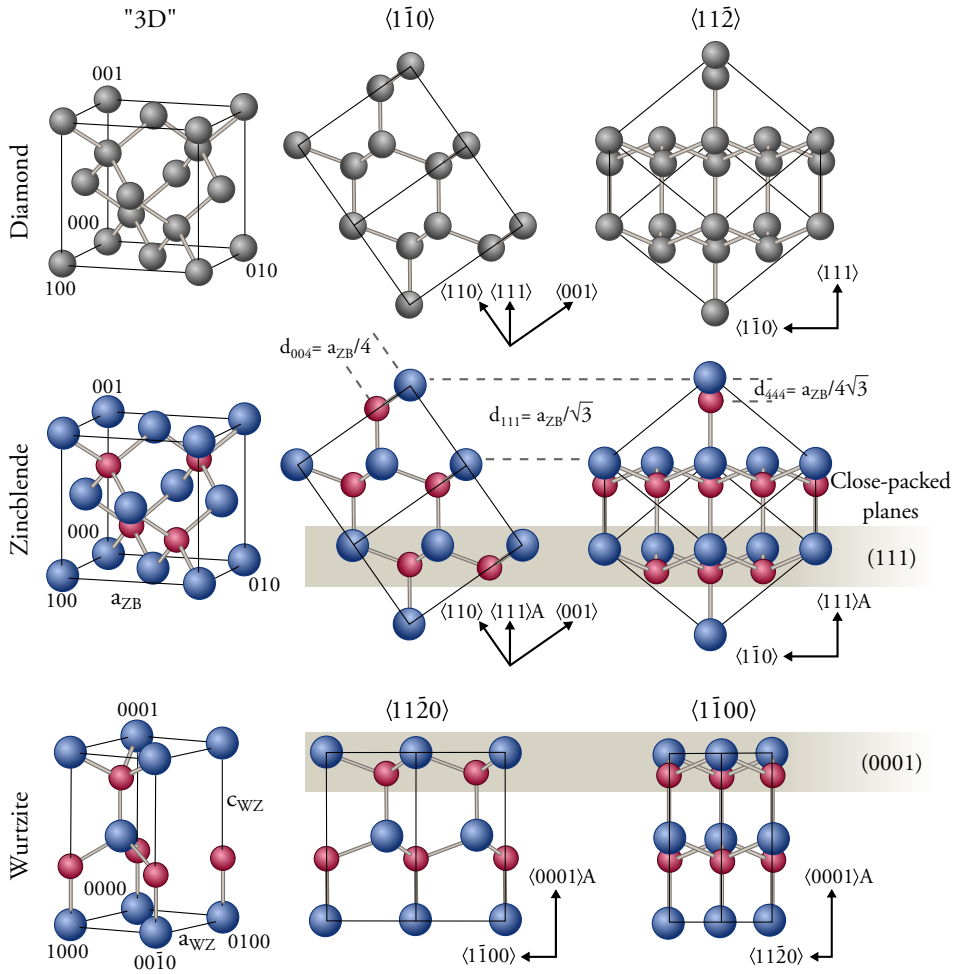

Figure 4.1: Unit cells of the cubic zincblende and hexagonal wurtzite crystal structure types, which III-Vs adopt, with the diamond crystal structure type of Si and Ge shown for comparison. The projections of the structures along ⟨110⟩ and ⟨112⟩ are also shown to highlight the similarities between the three. In these projections atoms lying outside the unit cells have been included to better show the projected structure as a whole. Distances between some of the planes are shown in terms of the lattice parameter. The bilayers in the horizontal close-packed planes have been marked for zincblende and wurtzite.

The similarity between the zincblende and wurtzite crystal structure types is best seen when viewing the structures along ⟨112⟩ for zincblende, which corresponds to ⟨1$\bar{1}$00⟩ for wurtzite. In figure 4.1 these projections are shown with the close-packed (111) and (0001) planes horizontal. In this projection the two structures appear identical and it will usually not be possible to distinguish the two in TEM images or diffrac-

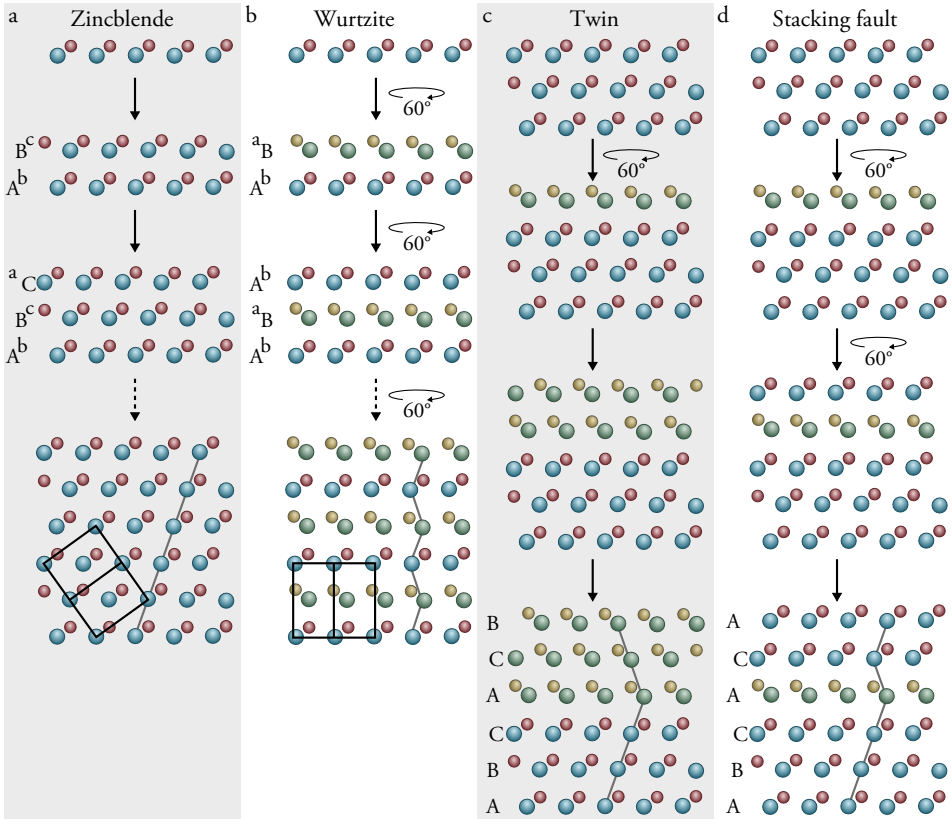

Figure 4.2: Stacking of (111) bilayers during growth to form the zincblende and the wurtzite crystal structure types, viewed in ⟨110⟩. By rotating each new layer 60° with respects to the previous, the stacking sequence changes from . . . abc. . . in zincblende to . . . abab. . . in wurtzite. The stacking sequences to form a twin and stacking fault in zincblende are also shown. The guide lines underneath the structures emphasize the stacking order.

tion patterns. In reality there are small differences in the distances in and between the close-packed planes in the two crystal structure types,[89] but for the purposes discussed in this thesis these can be disregarded.

When viewed in the ⟨110⟩ and ⟨11$\bar{2}$0⟩ direction respectively, the difference between zincblende and wurtzite can be seen. In zincblende each bilayer is oriented the same way, while in wurtzite each bilayer is rotated 60° around the plane normal with respect to the bilayers in the two neighbouring close-packed planes. As nanowires are most commonly grown on substrates with (111)B surfaces, the evolution of the two structures can be illustrated as in figure 4.2, where close-packed bilayers are added one at a time. If each new bilayer is added with the same orientation as the preceding one the result is the zincblende crystal structure type (a). Looking at one sub-lattice only, the

repeating stacking sequence is ...abc... in this case. If instead each bilayer is rotated 60° with respect to the preceding one the wurtzite crystal structure type is produced (b). Here the stacking sequence is ...ab... instead. As they differ only in the stacking sequence of the bilayers, zincblende and wurtzite are examples of *polytypes*. It is also possible to conceive of other, longer stacking sequences in higher order polytypes, where for instance only every other or every third bilayer is rotated with respect to the preceding one. The polytypes can be systematically named after the number of bilayers in the repeating stacking sequence and the crystal system to which they belong. In this scheme zincblende is named 3C (C for cubic), wurtzite 2H (H for hexagonal), and the ...abac... stacking sequence which corresponds to a rotation of every other bilayer is named 4H.[90] Although these crystal structure types might seem quite similar they do result in measurably different electronic structures and bandgaps for the same material,[vii] even in segments consisting of only a few bilayers.[91]

So far the focus has been on perfect crystals with a pattern of stacked layers that is repeated in principle indefinitely, which is rarely the case in reality for nanowires. Often there are local deviations and changes in the stacking order that need to be characterized, for which TEM is particularly well suited in comparison to for example X-ray diffraction. Consider for instance the ...abc**b**abc... stacking sequence where a single layer is inserted in an otherwise perfectly repeating pattern with cubic stacking. This is known as a stacking fault and is illustrated in figure 4.2d. There is also the possibility of changing the cubic stacking order as in the ...abcbca... sequence. Now there is no single layer that has been inserted or removed, but rather there are two different zincblende structures which are each other's mirror image. The two segments are in this case known as twins and the plane where the stacking sequence is mirrored is called the twin plane. There are actually three different ways of forming the twin which all have different structures in the interface between the two twin segments. The first, illustrated in figure 4.2c, simply involves a rotation of the second segment of 60° as discussed earlier, which maintains the III-V bonds across the interface. For this reason it is called a rotational or ortho twin. In this case only the stacking sequence rather than the crystal structure is actually mirrored over the twin plane. The two remaining possible twin structures form due to a true mirroring of the crystal structure, either by connecting two {111}A planes or two {111}B planes forming III-III or V-V bonds across the interface respectively. These are known as mirror or para twins and can be named more specifically para-III or para-V depending which type of interface is formed.[92,93] The different twin structures are discussed further in chapter 5 in connection to how they can be distinguished by TEM.

In III-V nanowires the twin planes are usually located on the (111) planes perpendicular to the [111]B growth direction. For TEM characterization the nanowires are normally imaged in a ⟨110⟩ direction perpendicular to the growth direction, lying flat on the carbon film on the grid. When viewed in this direction these twins are easy to distinguish as they do not overlap in the images. Occasionally, especially in Si nanowires,

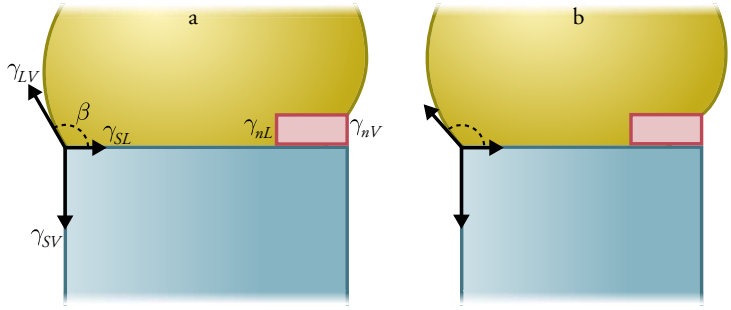

Figure 4.3: A closer look at the nucleation process with the relevant interface energies, γ, noted. The two nanowires are growing from the same volume seed particle, but with $\gamma^a_{LV} > \gamma^b_{LV}$. This difference results in a larger contact angle β in (b) than in (a) to maintain the force balance, assuming that the nanowire sides are perpendicular to the growth facet in both cases.

twins can however also form on other {111} planes, in which case they will overlap in the normal viewing directions. Overlapping twins can result in long range, typically 3×(111), variations in the contrast which can be mistaken as originating from a higher order polytype. In these cases it is important to image the nanowire in additional orientations,[94] or compare the high resolution images with conventional images relying on diffraction contrast.[95]

4.1 Polytypism in Nanowires

For III-V materials where zincblende is the stable bulk form, there is an extra energy on the order of $\Phi = 10 - 20$ meV per III-V atom pair associated with the formation of wurtzite. The difference arises from the fact that the third nearest neighbouring atoms are closer in wurtzite than in zincblende. For the III-N compounds, where the constituent elements differ more in electronegativity, this is actually advantageous as it brings atoms with opposing partial charges closer together.[96] The first attempts at explaining polytypism in non-nitride nanowires considered how the extra energy for wurtzite could be offset by forming more favourable surfaces[97] or edges[98] for the nanowire sides. For small enough diameters these interface and edge energies will dominate giving wurtzite the advantage, but this does not explain why wurtzite forms in larger nanowires. A better way of looking at this problem is to consider only the nucleus rather than a whole bilayer, as the orientation of the bilayer is decided by the orientation of the nucleus. For a small nucleus the barrier to forming wurtzite is low enough that occasionally an ...aba... sequence will form, resulting in twinning in the otherwise pure zincblende structure.[99] However, in nanowires it is under some growth conditions possible to force the material into adopting a pure wurtzite structure.

In order to explain how wurtzite can become dominant a closer look on the nucleus is needed.

Figure 4.3 shows a more detailed illustration of the nucleus forming underneath the seed particle than was shown in the previous chapter. The effective excess interface energy of the nucleus Γ is shown in equation 4.1 in terms of the interface energies γ between the nucleus (n), seed particle (L), nanowire (S) and vapour (V) phases for a nucleus where a fraction x is in contact with the vapour.

$$\Gamma = (1 - x)\gamma_{nL} + x(\gamma_{nV} - \gamma_{LV}\sin\beta) \tag{4.1}$$

The zincblende {110} facets are known to overgrow more rapidly than the wurtzite $\{1\bar{1}00\}$ or $\{11\bar{2}0\}$ counterparts, which suggests that they have a higher interface energy γ_{SV}.[100] In the same way that the interface and edge energies for the nanowire as a whole are lower for wurtzite (WZ) than zincblende (ZB), γ_{nV} should be lower also for a wurtzite nucleus making Γ_{WZ} as a whole lower than Γ_{ZB}.[101] The ratio between the nucleation barriers from equation 3.3 for zincblende and wurtzite is given by equation 4.2.

$$\frac{\Delta G^*_{WZ}}{\Delta G^*_{ZB}} = \frac{\Delta\mu_{ZB}}{\Delta\mu_{WZ}} \times \left(\frac{\Gamma_{WZ}}{\Gamma_{ZB}}\right)^2 = \frac{\Delta\mu_{ZB}}{\Delta\mu_{ZB} - \Phi} \times \left(\frac{\Gamma_{WZ}}{\Gamma_{ZB}}\right)^2 \tag{4.2}$$

The nucleation barrier ratio contains both a ratio of the respective liquid-solid chemical potential differences, which favours zincblende due to the extra cohesive energy Φ of wurtzite, and a ratio of the effective interface energies, which favours wurtzite. Equation 4.2 suggests two different mechanisms which can influence the ratio between the two crystal structure types. Increasing the supersaturation would decrease the relative importance of Φ, allowing the interface energies to dominate. Using this line of reasoning, the increased supersaturation for smaller seed particles from the Gibbs-Thomson effect has been proposed to be the underlying cause for the diameter dependence of the crystal structure.[102] The other way of affecting the crystal structure is by changing the interface energies. For instance, an increase in the liquid-vapour interface energy would favour wurtzite by making the relative difference in nucleus-vapour interface energy between the two structures more influential.

The higher order polytypes are not directly accounted for by this model as it only assumes a difference in energy between ...ab**c**... and ...ab**a**... nuclei. Indirectly this can still cause for instance short segments of 4H to form by chance if the nucleation barriers between zincblende and wurtzite are roughly equal. In order to explain extended segments of higher order polytypes, the model must however allow for planes even further down to influence the nucleation barriers.[xvii]

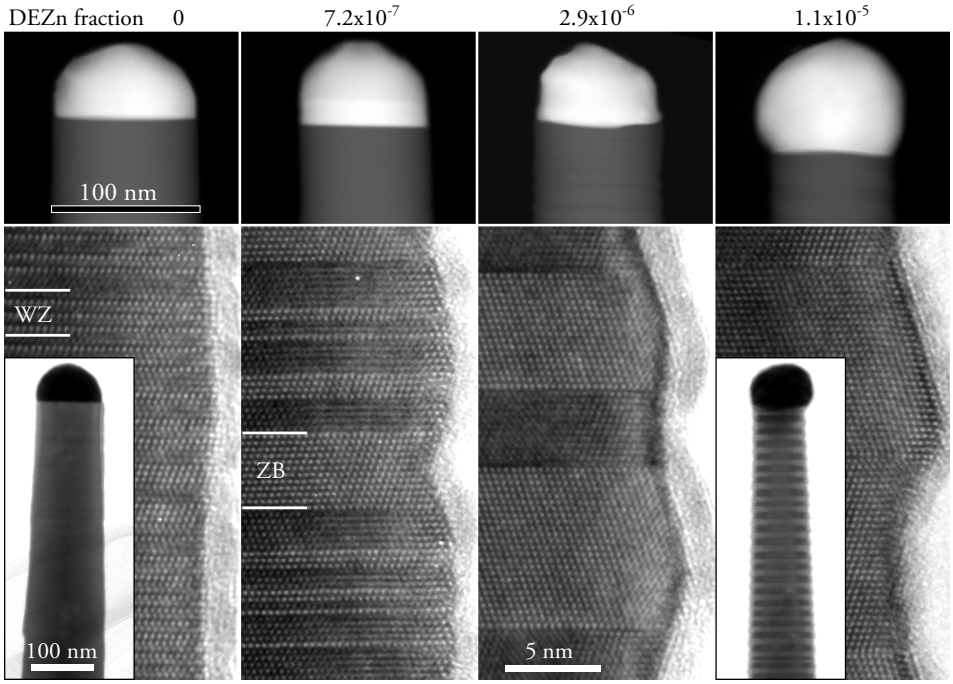

Figure 4.4: STEM images of the gold particles and top part of the nanowires (top), and HRTEM images (bottom) showing the effect of DEZn doping on seed particle and crystal structure respectively. For the lowest and highest DEZn molar fractions a TEM overview image is also included to show the effects on morphology.

By carefully optimizing the growth conditions it has become possible to fabricate defect free single crystalline nanowires of either the zincblende or wurtzite crystal structure type,[103] nanowires with controlled segments of both,[100] and even superlattices with short repeating sequences of the two.[104] Control of the crystal structure on this level will be essential for creating high performance devices from the nanowires, as unwanted variations in the crystal structure can be detrimental to the transport properties of the material.[105]

4.2 Changes in Crystal Structure with Zn Doping

Introducing additional precursors during the growth for doping can significantly affect the crystal structure of the growing nanowire by influencing the interface energies. Here I will briefly illustrate how dramatic these changes can be using the p-doping of InP with Zn from diethyl zinc (DEZn) as an example.

Figure 4.4 shows TEM images of InP nanowires grown with DEZn molar fractions

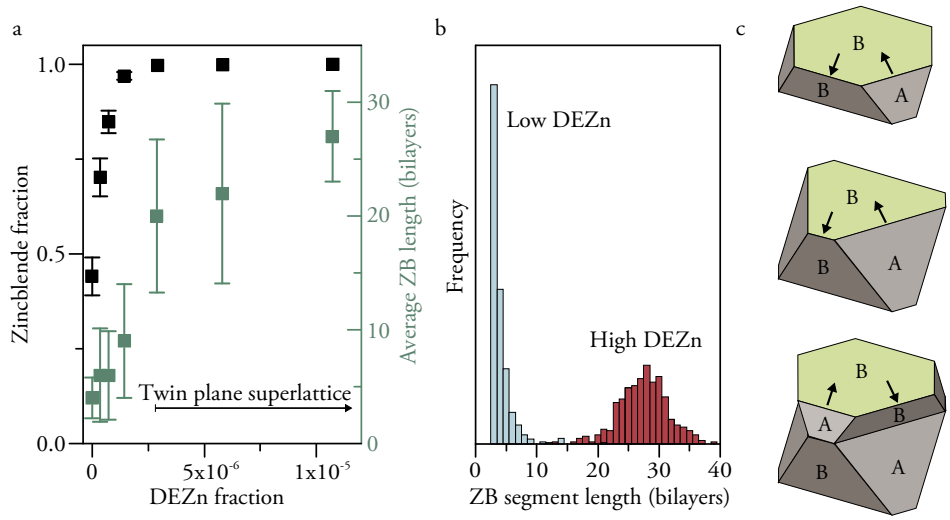

Figure 4.5: (a) Fraction of the nanowire which adopts the zincblende (ZB) crystal structuretype and average length of the zincblende segments as a function of DEZn fraction. (b) Distribution of zincblende segment lengths for the case of an undoped nanowire and for high DEZn fractions where a twinning superlattice has formed. (c) Illustration of the changing nanowire cross-section during growth with the polarity of the {111} facets noted. The seed particle has been removed from the growth facet (green) for clarity.

in the range of $0 - 1.1 \times 10^{-5}$. For comparison the group III precursor (TMIn) fraction was 6.3×10^{-6} during all these growths. From the high resolution images a trend towards zincblende with fewer, but more regularly spaced, twins can be seen. This is also visible in the overview TEM images for the two extreme cases where, in the case of high doping, the regular twinning produces a periodic striped pattern across the nanowire. The distribution between zincblende and wurtzite (stacking faults and other structures which cannot be classified as either of the two make up at most a few percent) is shown in figure 4.5a as a function of DEZn fraction. At DEZn fractions of 2.9×10^{-6} the crystal structure becomes pure zincblende and a twinning superlattice forms with a fairly regular spacing between the twin planes. Further increase of DEZn has two effects as seen in figure 4.5a: it increases the average twin segment length and reduces the variation. The difference between the normal mixed crystal structure and the twin plane superlattices can be seen in the histogram of the segment lengths in figure 4.5b. For the mixed crystal structure at low DEZn fractions only a few zincblende segments are longer than a few bilayers, while for higher DEZn fractions the majority of the twin segments are more than 20 bilayers long.

Unlike dimethyl zinc (DMZn),[106] DEZn does not have any dramatic influence on the growth rate and the nanowires have roughly the same length independent of the

dopant fraction. The growth rate is a very sensitive indication of the supersaturation, which can therefore be ruled out as an explanation for the change in crystal structure. This leaves changes in interface energies as a potential explanation. According to the force balance at the triple-phase line in figure 4.3 (triple-phase point in the 2D illustration) any change in liquid-vapour or solid-liquid interface energy should be visible as a change in contact angle β according to equation 4.3. As a side note, this expression implies that nanowire growth will only be stable for certain ratios of the interface energies, as the seed particle must not for example de-wet the nanowire by having a too large contact angle.[107]

$$0 = \gamma_{SL} + \gamma_{LV} \cos\beta \Leftrightarrow \cos\beta = -\frac{\gamma_{SL}}{\gamma_{LV}} \tag{4.3}$$

The contact angle measured post growth is not necessarily the same as the contact angle during growth. The increase in contact angle seen with increasing DEZn fractions can potentially arise when the sample is cooled down after growth. However a difference in contact angle during growth will also result in a difference in nanowire diameter provided that the seed particles are of the same size, which is the case here. The nanowire diameter can in this way be used as an indication of the relationship between γ_{SL} and γ_{LV} during growth. Making only a qualitative comparison from figure 4.4 a reduction in diameter with increasing DEZn fraction can be seen, indicating an increased γ_{SL}/γ_{LV}. If the increased ratio between the interface energies is due to a reduction in γ_{LV} this will directly favour zincblende by reducing the interface energy advantage of the wurtzite nucleus. If instead DEZn mainly increases γ_{SL} one can speculate that there should be a similar increase for γ_{nL}, which also would decrease the advantage of a wurtzite nucleus. Furthermore the increase in contact angle enters directly into the effective interface energy as described in equation 4.1, again in the favour of zincblende. As the change in diameter only indicates a change in ratio between the interface energies it is not possible to pin-point where DEZn exerts its influence.

The peculiar regular spacing of the twin planes at high DEZn fraction can in part be explained by the high barrier to forming an ...ab**a**... nucleus as explained above. The other cofactor is that the zincblende segments under these conditions form {111} side facets which are not parallel to the growth direction. With the addition of each new bilayer the cross section becomes increasingly triangular as the {111}A facets grow and the {111}B shrink, as shown in figure 4.5c. Only by introducing a twin plane can the cross section revert to becoming more hexagonal again, which would be preferable from the point of view of the spherical seed particle. In this way there is a balance between two opposing forces with the nucleus preferring to continue the zincblende stacking of the previous layers and the seed particle preferring to wet an as circular as possible top facet. At increasing DEZn fractions an increasingly triangular top facet is needed before the distortion of the seed particle makes the formation a twin plane favourable.

In this way the periodicity of the twin plane superlattice increases with increasing DEZn fraction and nanowire diameter.[78]

Chapter 5

Polarity Determination in Nanowires

The polar nature of the III-V materials, illustrated in figure 4.1 in the previous chapter, adds one more parameter, in addition to the stacking sequence, that needs to be determined in order to fully characterize the crystal structure. Exchanging the group III and V atoms in any of the structures illustrated in figure 4.2 will leave the stacking sequence of the bilayers the same, but will invert the polarity. This inversion would correspond to a change in growth direction from ⟨111⟩B to ⟨111⟩A. In order to determine the stacking sequence from high resolution images only the positions of the (111) planes need to be resolved. For the polarity on the other hand, the more closely spaced (004) planes need to be both resolved and differentiated to determine whether they are occupied by group III or V atoms. Note that while some directions in the zincblende crystal structure type are polar, such as the ⟨111⟩ directions, other directions are not. One example are the ⟨110⟩ directions, where the associated {110} planes contain equal amounts of the two elements.

For bulk materials the polarity can readily be determined for example from the different etching behaviour of the A and B type facets.[108] Substrates of the III-V materials can therefore be supplied with known polarity. III-V nanowires are often grown on (111)B III-V substrates where normally the known polarity of the substrate should be transferred to the nanowires. In this case it is usually not necessary to independently determine the polarity of the nanowires. However, when using III-V substrates of different orientations the nanowires typically still grow along ⟨111⟩ directions and will then be inclined to the substrate surface. In these cases the polarity of the nanowires is not always obvious from their orientation.

As III-V substrates are expensive it would be advantageous to grow the nanowires on substrates of other materials. One of the main advantages for III-V nanowires is in fact

that it is possible to grow them on silicon substrates, thereby integrating the high performance III-V materials with the cheaper and widely used silicon platform.[1, 2] Silicon, being a single element semiconductor, is not polar and should not directly determine the polarity of the initially grown III-V material.[109] The silicon substrate might still have a very strong influence on the polarity if the growth conditions causes a preference for either the group III or V element to bond to the substrate surface.[110] Other substrate materials, such as graphene, do not form chemical bonds to the nanowires but instead rely on the weaker van der Waals forces to direct the growth.[111] Here the influence of the substrate on the polarity should be even weaker. Finally, in the aerotaxy growth method described in section 3.1 there is no substrate at all during the growth that can impart a polarity on the nanowires.[V] In order to fully understand the growth in the cases presented here the polarity of the resulting nanowires needs to be determined.

The polarity of the nanowires is also interesting from an application point of view. If the two elements in the III-V material differ in electronegativity, there will be a net charge associated with the polar planes and therefore with the surfaces and interfaces consisting of these planes. The electric fields formed by these charges will influence the electrical properties of the structure. As the difference in electronegativity is largest for the nitrides the polarity effects have been studied most extensively for these materials. In III-N nanowire heterostructures grown in the polar $\langle 0001 \rangle$ direction, the electric field formed spontaneously over the heterojunction will influence the band structure. The direction of the electric field is determined by the polarity of the growth direction, which therefore needs to be determined in order to understand the electrical transport characteristics of the device.[112] These polarity effects can be either detrimental or beneficial for the device performance. In light emitting diodes the electric field can separate the electrons and holes in the active region, leading to poorer recombination and light emission efficiency.[113] In tunnelling diode applications on the other hand, the electric field can be used to tune the band bending in the active region to provide as small a tunnelling barrier as possible and thus improve the tunnelling current.[114]

Even if the substrate initially determines the polarity it is possible, if unlikely, that the polarity of the growing material is inverted, forming segments of different polarity within the nanowire. The boundary between such segments, known as an inversion domain boundary, would necessarily contain some type of defect such as homoatomic bonds between group III or group V atoms. Such boundaries are predicted to have a severe negative influence on the electrical properties of III-V materials.[115] Single polarity inversions have been found at the base in GaN nanowires growing in the [0001]B direction on (0001)A substrates.[116] Similar observations have also been made for ZnO.[117] In both cases it is thought that impurity or dopant atoms segregate to the inversion domain boundary, forming a single layer. These impurity atoms could have the ability to replace either of the two other elements in the crystal structure and therefore remove the need to form Ga-Ga (in GaN) or O-O (in ZnO) bonds.

In this chapter two methods for determining polarity in III-V materials are dis-

cussed: high resolution imaging of the structure by means of *focal series reconstruction*, and *convergent beam electron diffraction*. For focal series reconstruction, the determination of the local polarity over a twin boundary in an InP nanowire is given as an example. For convergent beam electron diffraction (CBED), the determination of the overall polarity of GaN nanowires grown on (0001)A substrates and GaAs nanowires grown by aerotaxy are used as examples. As long there is no need to determine interface structures, methods based on CBED are particularly good as they are applicable to most III-V and II-VI materials, are easy to use, produce easily interpretable results, and have very low demands on the microscope performance. An alternative method which also has very low demands on the microscope performance is channelling-enhanced XEDS,[118] which was mentioned briefly in section 2.5. Compared with CBED this method is however more difficult to use.

Scanning transmission electron microscopy also provides methods for determining the polarity in III-V materials, though none were used in the studies on which this thesis is based. With the use of hardware aberration correctors the electron beam can be now converged to a small enough probe that the group III and V atomic columns can be probed individually. This increased resolution has become particularly powerful when combined with HAADF imaging where the signal depends on the atomic number of the atoms probed, making it possible to directly differentiate the group III and V atomic columns in the image.[119] STEM-HAADF has been used in this way to directly image the polarity in for example InAs[71] and GaAs[109, 120] nanowires. Columns of very light elements such as nitrogen can however be difficult to detect in HAADF imaging, as they scatter very few electrons to high angles. For this purpose annular bright field (ABF) detectors have been developed which detect electrons scattered to lower angles of up to approximately 20 mrad.[121] Using either ABF or HAADF imaging depending on the material, the polarity of all III-V and II-VI materials can now be determined using STEM.[115] With the increased probe currents made possible by aberration corrected STEM it is even possible to generate enough signal to perform XEDS[122] or EELS[123] with atomic column resolution.

Finally, I should mention that other methods, not based on electron microscopy, can also be used for polarity determination. Scanning tunnelling microscopy, for example, also has the ability to resolve and differentiate the group III and V atoms on nanowire side facets or cleaved surfaces.[124]

5.1 Focal Series Reconstruction

Even with hardware aberration correction and negative C_3, residual aberrations and the sample thickness are still limiting factors for obtaining interpretable high resolution images. Focal series reconstruction reduces or eliminates the residual aberrations at the site of interest, and reduces the non-linear imaging effects that usually make images from

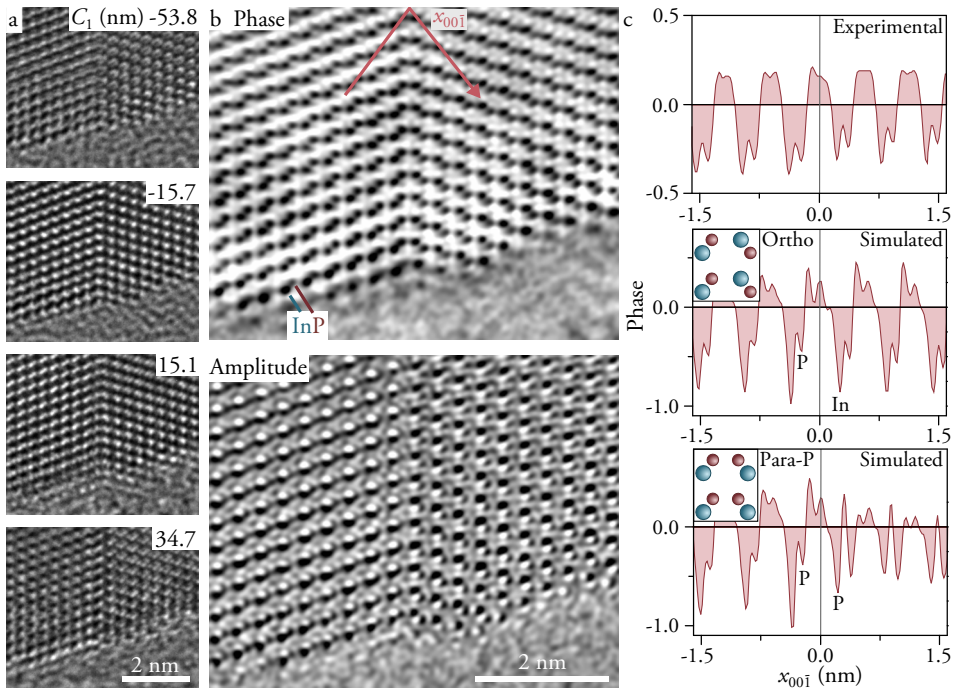

Figure 5.1: (a) Four example HRTEM images from a 20-member focal series of an InP nanowire with a zincblende twin plane superlattice, recorded with negative $C_3 = -10$ µm. (b) Reconstructed phase and amplitude of the object wavefunction using a linear Wiener filter method. The In-P dumbbells are clearly resolved and distinguishable. The nanowire growth direction is to the right in all the images. (c) Experimental and simulated phase line profiles in the dumbbell direction across the twin interface. For the simulated profiles, the model was given the same orientation as the actual sample. The insets show the structure of the ortho and para-P interfaces.

thicker samples difficult to interpret. The technique of combining hardware aberration correction and focal series reconstruction has for example been used to fully resolve the structure of 4 nm thick CdSe/CdS core-shell nanorods.[125] Dislocation cores in GaAs have also been analysed by this method, but required that the small tilt of the sample away from the intended ⟨110⟩ viewing direction was included in the simulations used for comparison.[126, 127]

Sample tilt is a particularly important factor to consider for aberration corrected images, but needs to be taken into account also when analysing conventional high resolution TEM images.[128]. For the GaAs dislocations cores characterized by Tillmann et al. the sample was only about 6 nm thick.[126] As the effects from sample orientation increase with sample thickness, the need to take to take sample orientation into account will be even greater when imaging nanowires. Nanowires can in addition be

quite difficult to orient in the microscope as they are flexible and often bend and twist along their length. In order to use focal series reconstruction for analysing polarity in nanowires, the local tilt of the nanowire away from the intended viewing direction must be taken into account. A simple method for measuring small, local deviations from a ⟨110⟩ orientation for the zincblende crystal structure type is presented in paper I. The use of this method for determining the polarity of a nanowire from focal series reconstructions is described in the remainder of this section, using a twin boundary in an InP nanowire as an example.

Figure 5.1a shows four TEM images, recorded at different defocus, of a small area around a twin boundary in the InP nanowire. The nanowire contains such twin boundaries at a regular interval because it was subjected to heavy Zn doping during its growth, as discussed in section 4.2. With a diameter of 30 nm and with each twin segment consisting of 16 bilayers on average, the *minimum* projected thickness of this nanowire in a ⟨110⟩ viewing direction is just over 14 nm. The images in 5.1a are extracted from a 20-member focal series recorded on an aberration corrected JEOL 2200 MCO with $C_3 = -10$ µm. The small aberrations remaining after the hardware aberration correction should yield a resolution of 0.12 nm, as shown in figure 2.3 in chapter 2. This resolution should make it possible to resolve the 0.147 nm In-P dumbbell separation in a ⟨110⟩ projection. However, due to the thickness of the nanowire, the In-P atomic columns cannot be unambiguously distinguished at any defocus. The interface structure and polarity can therefore not be determined from any single image.

In figure 5.1b the object wavefunction phase and amplitude, reconstructed from the focal series, are shown. The reconstruction corrected for the remaining small spherical aberration and defocus in each image. In addition the twofold astigmatism was also corrected, as it had increased since the hardware aberration corrector was tuned at the beginning of the session. In the reconstructed object wavefunction phase, the individual In and P columns can be resolved and display a contrast pattern where the leftmost atom of the pair is darker. Intuitively the darker spot might be interpreted as corresponding to the In atomic columns, and the lighter as corresponding to the P atomic columns. Before such an interpretation can be made however, the exact orientation of the nanowire needs to be determined for the reasons stated earlier.

In order to estimate the nanowire orientation the Fourier transform of the reconstructed object wavefunction can be used. Unlike the conjugate symmetric diffractogram of a real-valued regular image, the Fourier transform of the object wavefunction is identical in amplitude to the diffraction pattern. The Fourier transform can however be calculated from a much smaller area than the minimum area for which actual selected area electron diffraction is possible. In electron diffraction patterns from thick InP zincblende crystals, dynamical scattering often produces unequal intensities in opposing reflections, $I_G \neq I_{-G}$. One exception is fortunately the $G = 220$ and $-G$ reflections, which have equal intensities for all sample thicknesses in the $[1\bar{1}0]$ orientation. However, if the crystal is tilted slightly in a [110] direction the centre of the Laue circle

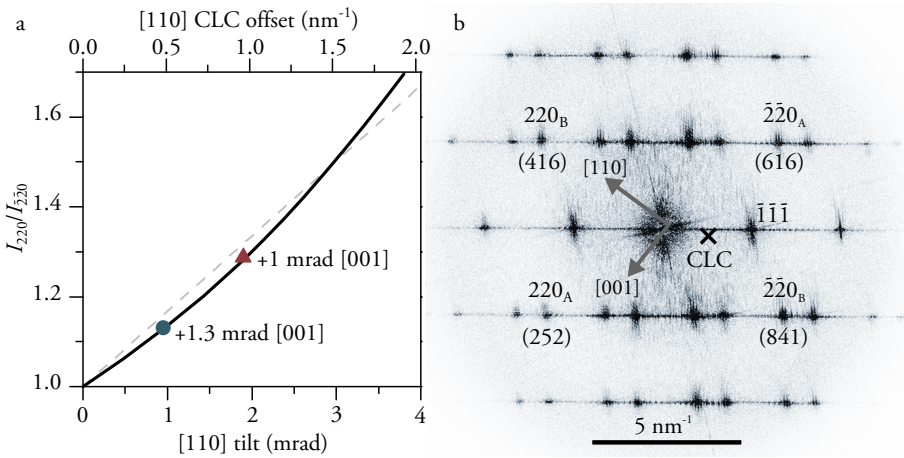

Figure 5.2: (a) Multislice simulation of the effects of crystal tilt in a [110] direction on the ratio of the intensities of the two 220-type reflections. Two additional simulations which have tilts also in the perpendicular [001] direction show that the correlation between the intensity ratio and [110] tilt is robust. (b) Diffraction pattern calculated for the reconstructed object wavefunction from figure 5.1b with the centre of the Laue (CLC) circle marked with x, according to the method from (a).

(CLC) will be shifted closer to either G or $-G$, resulting in unequal excitation errors, and therefore also unequal intensities, for the two reflections. The ratio of the intensity in the two reflections, $I_{220}/I_{2\bar{2}0}$, can therefore be related to the crystal tilt in this particular direction as shown by figure 5.2a. Tilting the crystal in the perpendicular [001] direction does not shift the CLC closer to either G or $-G$, and $I_{220}/I_{2\bar{2}0}$ is not affected. For this reason, tilt in a single zincblende crystal can only be measured in one direction by this method. Luckily the two twin segments in the nanowire in figure 5.1a constitute two zincblende crystals with non-parallel [110] directions for which the tilt can be estimated. The CLC calculated from the two intensity ratios is marked in the calculated diffraction pattern in figure 5.2b, and corresponds to a 4 mrad tilt 3° away from the $[\bar{1}\bar{1}\bar{1}]$ direction. Using this estimate, phase profiles can be simulated along the dumbbell $[00\bar{1}]$ direction and compared to the reconstructed object wavefunction, as shown in figure 5.1c. Clearly the ortho model with preserved polarity across the twin boundary provides the best match, confirming the intuitive interpretation of the reconstructed object wavefunction phase.

It is important to note that the experimental profile shows the same qualitative agreement with the ortho model when using tilt magnitudes ±1.5 mrad and directions ±20° from the estimate. For tilt directions 180° away from the estimate, the difference between the contrast at the In and P columns disappears, which would make it impossible to measure the polarity. In order to use focal series reconstruction for polarity

determination it is therefore crucial not only that the tilt can be estimated, but also that the sample is not tilted in the "wrong" direction.

5.2 Convergent Beam Electron Diffraction

For kinematical scattering the intensities of the G and $-G$ reflections are identical in the diffraction pattern, which is known as Friedel's law. The lack of any difference between the two means that it is not possible to determine the polarity of the nanowire growth direction from such a diffraction pattern. For electrons, unlike X-rays, most samples do however result in dynamical diffraction due to the strong interaction between the electrons and the atoms in the sample. In dynamical diffraction the intensity of opposing reflections will not necessarily be the same, and can accurately reflect the non-centrosymmetric structure of the III-V materials. Dynamical diffraction is often considered a problem for electron diffraction as the intensities in the reflections will be dependent not only on the crystal structure but also the sample thickness. For polarity determination dynamical diffraction is however an advantage, as long as the effects of thickness and crystal orientation on the disparity between the G and $-G$ intensities can be separated from the effects from the polarity.

Converging the electron beam to a small probe on the sample with convergence semi-angle α causes the spots in the diffraction pattern to expand to discs with radius α/λ. In such a convergent beam electron diffraction (CBED) pattern, the effects of a multitude of slightly different beam tilts on the diffraction can be observed simultaneously, with each beam tilt corresponding to a point within the discs. By analysing the patterns within and between the discs the effects of thickness (changes the patterns within the discs), orientation (displaces the patterns in the discs), and polarity (causes a difference in the G and $-G$ patterns) can be distinguished.

For investigating polarity in III-V materials there are two different CBED techniques which can be used depending on the difference in atomic number, ΔZ, between the group III and V atoms. If ΔZ is large (i.e. for materials other than AlP, GaAs, and InSb) the polarity can be directly determined from a zone axis pattern by matching it with a simulated pattern. The thickness of the sample is simultaneously obtained by setting the thickness in the simulation to give the best match with the experimental CBED pattern. The procedure is most easily illustrated for GaN, which produces particularly clear CBED patterns when viewed in $\langle 1\bar{1}00\rangle$,[129] as shown in figure 5.3. The contrast in the CBED patterns that this method relies on is generated mainly by the dynamical scattering from the planes parallel to the electron beam. In the $\langle 112\rangle$ and $\langle 1\bar{1}00\rangle$ orientations for zincblende and wurtzite respectively, the projected structures appear identical, allowing polarity to be determined independently of crystal structure or the presence of twins or stacking faults. When viewed in the $\langle 110\rangle$ and $\langle 11\bar{2}0\rangle$ orientations instead, the presence of short twin segments and stacking faults produces streaking in

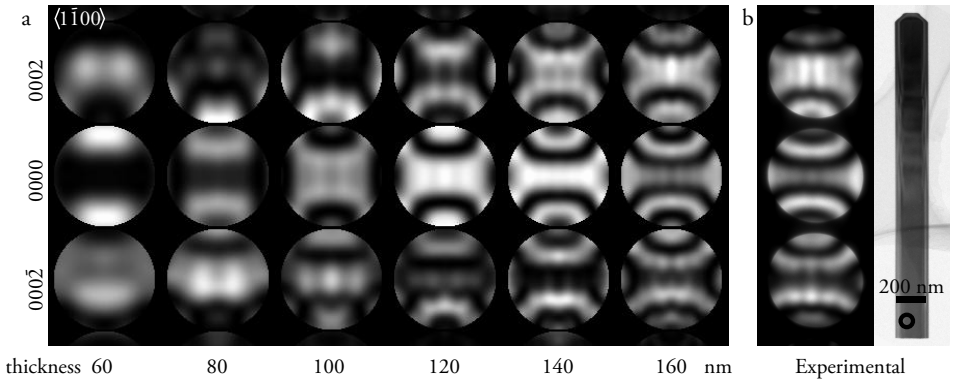

Figure 5.3: (a) A series of GaN CBED patterns simulated for increasing thickness for the 0000 and two 0002-type reflections. (b) CBED pattern recorded from the area marked with a circle on the GaN nanowire. The pattern matches the simulation for 160 nm well and shows that the nanowire growth direction (up in the image) was [0001]A.

the diffraction pattern, making it much harder to form clear CBED patterns. If the twin segments are more than a few tens of nanometres large it is however possible to locate and analyse them individually in this orientation.

For smaller ΔZ dynamical diffraction usually does not result in large enough differences in amplitude between the discs to reveal the polarity. An alternative CBED method can however be used for zincblende which relies instead on phase differences between the dynamically scattered beams. For this method the crystal needs to be tilted, as shown in figure 5.4a–b, so that only three reflections are strongly excited: either 002 together with $\bar{1},\bar{1},11$ and $\bar{1},\bar{1},\bar{9}$, or $00\bar{2}$ together with $\bar{1},\bar{1},\bar{1}1$ and $\bar{1},\bar{1},9$.[130] For GaAs and a 300 kV TEM this involves tilting approximately 7° from the ⟨110⟩ zone around a ⟨002⟩ direction. For the 002 case there are now three possible scattering pathways into the 002 disc, as shown in scheme 5.1. Here the indices above the arrows denote the scattering vector.

$$\begin{aligned} &000 \xrightarrow{002} 002 \\ &000 \xrightarrow{\bar{1},\bar{1},11} \bar{1},\bar{1},11 \xrightarrow{1,1,\bar{9}} 002 \\ &000 \xrightarrow{\bar{1},\bar{1},\bar{9}} \bar{1},\bar{1},\bar{9} \xrightarrow{1,1,11} 002 \end{aligned} \tag{5.1}$$

For the two indirect pathways both scattering vectors are of the $h + k + l = 4n + 1$ type. A similar analysis can be made for the $00\bar{2}$ case, where the indirect pathways instead are $h + k + l = 4n - 1$.

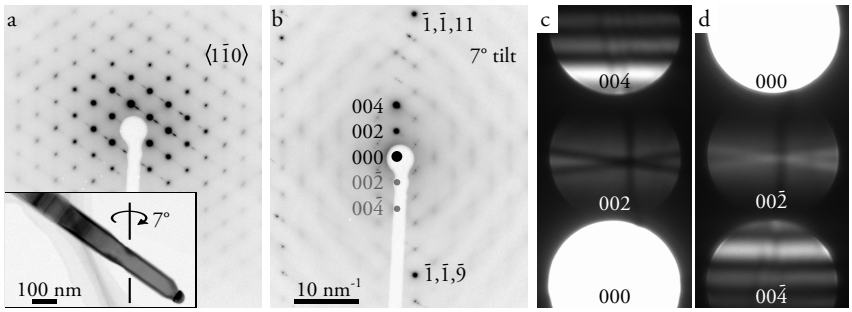

Figure 5.4: (a) SAED pattern from a GaAs nanowire recorded in $\langle 1\bar{1}0 \rangle$. The inset shows a TEM overview image of the nanowire in the same orientation. (b) Appearance of the SAED pattern after tilting approximately 7° along the 002 Kikuchi band, in order to excite the $\bar{1}, \bar{1}, 11$ and $\bar{1}, \bar{1}, \bar{9}$ reflections. (c) Details of the CBED pattern containing G= 000, 002, and 004, recorded from (b) after setting the beam convergence angle to 3.4 mrad. (d) Corresponding pattern for $-G$.

The phases, φ, of the scattered beams can be calculated from the structure factor plus a factor of $-\pi/2$ for the scattering event as shown in equation 5.2.

$$\varphi = -\frac{\pi}{2} + \sum_i f_i \exp\left[2\pi i \left(hx_i + ky_i + lz_i\right)\right] \tag{5.2}$$

For small ΔZ the atomic scattering factors can be replaced with the average scattering factor $\bar{f}$ plus or minus some small Δf, so that for GaAs the scattering factors become $f_{Ga} = \bar{f} - \Delta f$ and $f_{As} = \bar{f} + \Delta f$. This change in notation simplifies the calculation greatly as the small effect of the Δf terms on the phase of the scattered electrons can be ignored. The phases for each of the three different types of scattering event are shown in scheme 5.3.

$$\begin{aligned} 00 \pm 2 &\rightarrow \phi = -\pi/2 + \pi = \pi/2 \\ 4n + 1 &\rightarrow \phi = -\pi/2 + \pi/4 = -\pi/4 \\ 4n - 1 &\rightarrow \phi = -\pi/2 - \pi/4 = -3\pi/4 \end{aligned} \tag{5.3}$$

The resulting phase for the indirect pathways becomes $-\pi/2$ for the 002 case and $\pi/2$ for the $00\bar{2}$ case, which is respectively out of phase and in phase with the direct scattering. Under these specific three beam conditions a constructive interference pattern will be seen in the $00\bar{2}$ disc, while a destructive interference pattern will be seen in the 002 disc. As the two 002-type discs can now be differentiated it becomes possible to assign the polarity to the 111-type discs.[131] The appearance of bright or dark interference lines in the 002-type discs is shown for GaAs in figure 5.4 and illustrates the

difference more clearly. As a general rule the constructive interference signifies the direction of the heavier element, and there is no need to repeat the full analysis of the phases for all the different materials. Although the very small ΔZ materials such as GaAs are best suited for this method, it has also been shown to work for InP[131] and GaP[108]. For these materials one needs to be a bit more careful as the larger Δf will affect the phase of the scattered beams. In this case, the simple rule of constructive interference corresponding to the heavier element might not hold true for thick samples.

Using the method outlined above, the polarity of the growth direction was investigated for ten GaAs nanowires grown by aerotaxy. A sample was chosen with fairly thick nanowires with a pure zincblende crystal structure type containing only a few twins. The thickness insured dynamical diffraction and the long zincblende segments made it easier to achieve the correct diffraction condition. All ten nanowires were found to have grown in a $\langle 111 \rangle$B direction. The bases of the aerotaxy nanowires were often observed to be twinned on many different {111} planes, indicating that the gold particle initially "attempted" growth on many different facets on the small crystallite. Only a {111}B facet, once large enough to support the gold particle, could however result in stable nanowire growth. The fact that the {111}B facets are favoured over {111}A is known also from normal, substrate based growth. GaAs nanowires grown on silicon substrates have for instance been observed to rapidly abandon the vertical $\langle 111 \rangle$A growth direction for an inclined $\langle 111 \rangle$B directions, in those cases where the initial crystallite happened to form with an A polarity.[109]

Chapter 6

Compositional Analysis

The composition is an important characteristic that shoul be determined for almost all nanowires, perhaps with an exception for those known to consist of a single undoped group IV or binary III-V material. Transmission electron microscopy fortunately produces many different signals that can be used for quantitative compositional analysis, each with its own set of strengths and weaknesses. In this chapter three classes of methods are discussed in more detail: *X-ray spectrum imaging*, *plasmon chemical shift measurements*, and *local lattice parameter measurements*. The discussion is focused on the application of these methods to axial heterostructures where the transition from one material to the other is often gradual and produces a compositional gradient. In order to relate the nature of this graded interface to the growth processes and to the performance of the nanowires for the intended application, the composition should ideally be mapped with high resolution and precision.

X-ray spectrum imaging, where a full EDX spectrum is recorded for each pixel in the image, is the most versatile of the three methods presented here. As each element has a unique X-ray fingerprint in the EDX spectra, the prevalence of each element can be determined independently. *Plasmon chemical shift measurements*, although based on EEL spectroscopy, only yield a single value for each measurement: the plasmon energy. This method is therefore most useful in cases where there is a single unknown parameter for the composition, such as x in the ternary compound $Al_xIn_{1-x}P$. Ternary compounds, either intentionally grown or unintentionally formed in the transition between two binary materials, are however common occurrences in III-V nanowires. *Local lattice parameter measurements* similarly also yields a single value: the local spacing between lattice planes, which can be converted to the local lattice parameter. Lattice parameters can of course also be measured very accurately by X-ray diffraction, but with a much worse spatial resolution than can be achieved by TEM based methods.[89]

Some of the polarity determination methods discussed in the previous chapter involved the identification of the element for individual atomic columns. In the examples

discussed in chapter 5 the methods were however only used in a qualitative, rather than quantitative, fashion. It is possible to quantitatively analyse reconstructed object wavefunctions, but this puts even stricter limits on the specimen thickness. Using focal series reconstruction the compositional grading in a planar InAs-GaInSb heterostructure has been analysed separately for the group III and V transitions.[132] Similar analyses have also been performed for lattice resolved STEM-HAADF images, where the contrast is less sensitive to thickness effects than HRTEM images.[133, 134] These methods yield very high spatial resolution analyses of compositional grading, but in order to get absolute quantifications the composition at the start and end of the graded region must be known. This is also the case for both plasmon chemical shift and local lattice parameter measurements. For these methods it is however much easier to use external calibration samples as the properties measured are less sensitive to the sample thickness than the image contrast. For lower resolution HAADF images, absolute compositions have been determined successfully by comparing the contrast with simulated images. In order to achieve good matching between the simulated and experimental images in the case of $GaAs_{1-x}Sb_x$, it proved necessary to include the effects of static atomic displacements caused by the large difference in atomic radii for the two group V elements.[135] The contrast in HAADF is in other words not only related to the atomic number, and can be quite complicated to interpret quantitatively.

All TEM based methods for compositional analysis have in common that they yield only a 2D projection of the composition of the 3D sample. This limitation can be circumvented by acquiring many such 2D projections at different sample orientations and afterwards combine them in a tomographic reconstruction.[136] For nanowires such tomographic methods are not necessary on a routine basis. In axial heterostructures the composition is radially homogeneous in most cases, and no information is lost in a 2D projection perpendicular to the nanowire growth direction. Radial heterostructures are more complicated to analyse, but often the geometry of the nanowires is known well enough that the projection effects can be taken into account. For cases where the full 3D composition is needed, atom probe tomography can often surpass TEM based methods. In atom probe tomography the sample is evaporated atom by atom, with the atomic number and position being determined for a sizeable fraction of the leaving atoms. This method can only be used for small volumes and needle shaped samples, but this is not a severe limitation for most nanowires. The very high sensitivity of atom probe tomography has also made possible the detection of single gold atoms embedded in InAs nanowires at concentrations of 100 ppm.[137] Atom probe tomograms can however become distorted if the sample contains materials with different evaporation yields. Where such distortions are suspected, STEM-HAADF imaging can provide an independent and higher resolution reference.[138]

A larger limitation for the characterization of nanowires is that they are analysed only after the structure has fully formed. In post growth analyses the dynamics of the growth are lost, making it difficult to infer why the growth for instance resulted

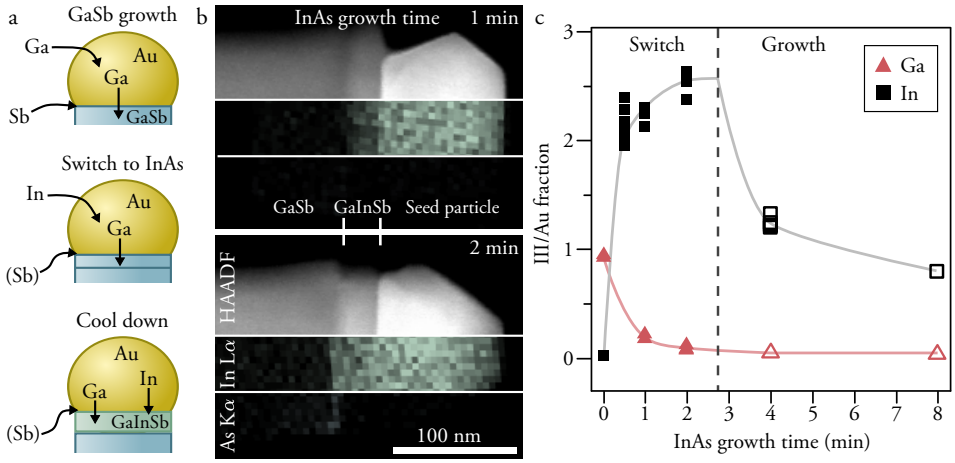

Figure 6.1: (a) Illustration of the processes occurring during GaSb growth, the switch to InAs, and during the cool-down period when terminating the growth. (b) STEM-HAADF images overlaid with XEDS maps of In Lα and As Kα, recorded for GaSb-InAs heterostructured nanowires where the growth was terminated after one or two minutes of supplying InAs precursors. (c) Compositional evolution of the seed particle during the switch from GaSb to InAs, calculated by taking into account the material expelled into the GaInSb segment during the cool-down period. The compositions measured from different nanowires are shown individually and the solid lines only serve as guidelines to the trend in composition over time.

in a particular compositional gradient. Abruptly terminating the growth at various stages can yield important clues, but does not generally represent a "frozen" moment in time. Even when both precursor supplies are turned off and the susceptor is cooled as rapidly as possible, the state of the nanowires can change quite a lot during the growth termination. Growth species adsorbed on the substrate surface can be incorporated into the nanowire, material dissolved in the gold particle can precipitate or parts of the nanowire can re-dissolve into the gold particle.

Occasionally the changes occurring during the cool-down period can be accounted for, making it possible to deduce the state of the nanowire just prior to the cooling. For instance, growth occurring during the cool-down period will form a segment underneath the gold particle that can sometimes be quite distinct from the rest of the nanowire. The origin of this extra segment can then be deduced from how its length, l, depends on the nanowire diameter, d. For material precipitating from the seed particle a $l \propto d$ relationship is expected as the amount of material available scales with d^3, while the volume of the segment scales with ld^2. If the material instead originates from adsorbed growth species one might expect instead a constant l, as the collection area for the adsorbed species scales with d^2.

In cases where the segment formed during the cool-down period originates from material precipitating from the seed particle, simply adding the material in this segment to the seed particle will yield an estimate of the seed particle composition just prior to cooling the sample.[139] Figure 6.1 shows an example of such an analysis for a GaSb-InAs heterostructure, discussed in more detail in paper III. In order to understand the origin of the compositional grading in this structure, the growth was terminated at various stages after switching to the InAs precursors. The InAs growth time here refers to the time measured from the switch of the precursors, regardless of whether an InAs segment had time to form or not. Figure 6.1a illustrates the processes occurring during the GaSb growth, the switch to InAs, and the cool-down period. During the switch to InAs, In enters the seed particle as Ga is expelled and reacts with the remaining Sb to form GaSb. If the growth is terminated before InAs forms, both In and Ga are expelled to some extent during the cool-down period. In the overlaid HAADF images and XEDS maps in figure 6.1b the segments formed during the cool-down period can easily be recognized as they consist of GaInSb, rather than GaSb as the previously grown segment or the intended InAs. The estimates of the seed particle composition at various stages of the materials switch and InAs growth are shown in 6.1c. This demonstrates how powerful simple post growth measurements can be under the right circumstances.

Note that once an InAs segment forms it is no longer possible to distinguish any segment formed during the cool-down period from the rest of the nanowire. The compositions for 4 and 8 min of InAs growth are therefore estimated under the assumption that no precipitation occurred during the cool-down period, and are likely less precise than the other estimates.

6.1 X-ray Spectrum Imaging

In STEM it is possible to acquire a full spectrum by for example XEDS at each position of the probe, thereby forming a spectrum image which has an additional dimension. From such a spectrum image it is possible to extract the qualitative distribution of an element by simply summing the counts under the corresponding peak in the EDX spectra. This technique was used to produce the maps in figure 6.1b. If the elements in the sample result in overlapping peaks, which is the case for example for In and Sb, such maps can however be misleading. A better method for calculating elemental maps is to instead fit reference spectra from all constituent elements to each spectrum in the spectrum image. Such a fitting procedure removes the effects from overlapping peaks, and the results can be further processed to yield quantitative maps if the correspondence between the ratios of the elements and the ratios of their X-ray yields are known.

In TEM the beam always damages your sample in some way, making it essential for all spectroscopic techniques to gather as much signal as possible before the sample has been altered too much from its original state. Spectrum imaging helps in this

regard by spreading the electron dose over a large area. Summing the spectrum image in one direction produces a spectrum line trace where the dose at each position is effectively spread over a larger area. Some of the III-V materials, for instance InP, are quite rapidly damaged by the focused electron beam in STEM, making acquisition schemes like this particularly important. Summing the spectrum image in one direction of course requires that the composition in the sample only varies in the perpendicular direction. Similar dose-spreading acquisition schemes have previously been used for recording EEL spectrum images of beam sensitive material.[140]

The other benefit of recording spectrum images is that it is possible to apply statistical analyses to the large dataset in order to reduce the noise in each spectrum. Principal component analysis (PCA) is one such method that has proven very useful for noisy X-ray spectrum images.[141] PCA makes use of the fact that the signal at the different energies has a large covariance while the random noise does not. For instance, in a sample containing only copper there is a strong relationship between the number of counts at 8.0 keV and 8.9 keV, as they correspond to the Cu Kα and Kβ characteristic X-rays respectively. The EDX spectra are usually described in terms of counts of X-ray photons in a number of energy channels, but they could equally well be described by any set of linear combinations of these energy channels. With PCA a particular set is found so that the first linear combination of energy channels, called the first principal component, covers the maximum amount of variation in the data. The second principal component is then chosen to cover the maximum variation remaining after the first principal component has been subtracted and so on. It is important to note that PCA makes no assumptions about the original data, but only attempts to explain as much of the variation with as few principal components as possible. A more rigorous description of the use of PCA for noise reduction in X-ray spectrum images is given by Burke et al.[141]

Continuing with the copper example, a spectrum image might contain hundreds or thousands of energy channels in each pixel, but the variation of the counts in these channels reflects only one signal. Applying PCA to this spectrum image the first principal component should reflect the copper signal, with the remaining principal components containing only the noise which is not correlated from pixel to pixel. By retaining only the first few principle components, the original data can then be reconstructed with greatly reduced noise. The choice of the number of principal components to retain can be slightly arbitrary, but can be aided by knowing that spectra containing n elements should in principle be possible to describe using only n principal components. Even so, it is important to consider how much of the original signal is lost in the principal component filtering so that no artefacts are introduced by accident. After the noise reduction, the reconstructed spectra can be processed further for quantification or mapping as usual.

The application of X-ray spectrum imaging to characterizing the transition region in a heterostructure is illustrated in figure 6.2. This particular example of an InAs-

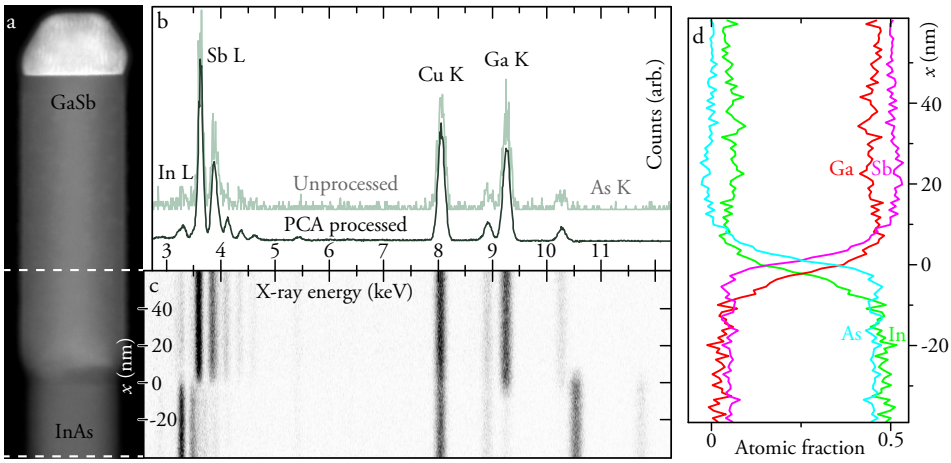

Figure 6.2: (a) STEM-HAADF overview image of the heterojunction area of an InAs-GaSb nanowire. (b) Energy dispersive X-ray spectrum from the GaSb segment, corresponding to the top part of the spectrum image in (c). The spectrum is shown both unprocessed and after PCA filtering, retaining only the five first principal components. The unprocessed spectrum image in (c) is shown with inverted contrast in order to enhance visibility. Black corresponds to only about 40 counts. (d) The compositional profile across the heterojunction calculated from a PCA filtered spectrum image, showing the non-synchronous switch of the group III and group V elements.

GaSb nanowire is taken from paper IV, but here a more in-depth description of the characterization method is given. A full X-ray spectrum image was acquired from the region marked in figure 6.2a, and subsequently summed in the radial direction into the spectrum line-trace shown in figure 6.2c. The spectrum image was acquired with a pixel size of 0.9 nm over 18 minutes. Even so each spectrum in the line-trace contains only about 2000 counts in total and they are therefore quite noisy, as shown in figure 6.2b. Since the dose was distributed along the radial direction, the acquisition time was in this case limited by the drift of the nanowire rather than the beam damage.

In the 2.5-12.5 keV energy range the EDX spectra only contain characteristic X-ray peaks from the four elements in the heterostructure and from Cu, which is present due to the nearby grid. The five first principal components from the spectrum image cover 93 % of the variance in the original data, and result in spectra with greatly reduced noise. The PCA processed spectra were then fitted with reference spectra acquired from GaAs, InAs, GaSb and InSb nanowires. By comparing the relative peak intensities of Ga and In from the GaAs and InAs references, and As and Sb from the GaAs and GaSb references, the fit of the reference spectra was converted to the compositional profile shown in figure 6.2d. Note that in this quantification the ratio between the group III and V elements is assumed to be one, and is not determined from the measurement.

Dopant Profiling

A rather special, but important, case of compositional analysis for semiconductor materials is dopant profiling. Using a 20 nm wide nanowire with a high dopant concentration of 10^{19} cm^{-3} as an example, there are on average only about three dopant atoms in any one nanometre thick cross section of the nanowire. If these dopant atoms were to segregate to the nanowire surface, twin planes or stacking faults, this would have very large effects on the properties of the nanowire. At such low concentrations it is of course very challenging to detect the dopant elements, let alone to quantify or map their distribution. Detection of single dopant atoms using electron microscopy has been demonstrated for heavy atoms in a lighter matrix using aberration corrected STEM-HAADF imaging. In samples from bulk silicon, Sb dopant atoms have been detected using this method. Simulations indicate that this would not be possible by any high resolution TEM method, including focal series reconstruction.[142] The STEM-HAADF method was even capable of determining at what depth the Sb atoms were imbedded from the change in contrast with defocus.[143]

In silicon nanowires, individual gold atoms originating from the gold seed particle have been found using the same method.[144] The smaller the difference in atomic number between the dopant and the matrix, the more difficult it will be to detect the dopant atoms based on HAADF contrast alone. In GaAs for instance, the pure GaAs atomic columns result in almost as much high angle scattering as the columns that include single Au atoms. Only by tilting the nanowire away from the $\langle 110 \rangle$ zone axis, and thereby reducing the scattering from the pure GaAs atomic columns, could the excess scattering from the heavier Au atoms be distinguished.[145] Atomically resolved spectroscopy methods have also been used to detect single dopant atoms, and do not depend on large differences in atomic number between the dopant and the matrix.[74]

For detecting very low concentrations, atom probe tomography should be mentioned again as a powerful alternative or complement to electron microscopy. Using atom probe tomography an unintentionally uneven distribution of P dopant atoms has been observed in Ge nanowires, with the core having a factor 10 lower, and the shell a factor 10 higher, concentration than was intended.[146] For extremely high dopant concentrations, such differences in doping between the core and the shell will also be detectable by X-ray spectrum imaging, as shown in figure 6.3 for a S doped InP nanowire. In this case the average sulfur concentration, as measured by XEDS while illuminating the whole nanowire, is around 1 at%. This corresponds to a concentration on the order of 3×10^{20} cm^{-3}, which perhaps should be called alloying rather than doping.

In order to detect any difference in the S content between the core and the shell, X-ray spectrum images were recorded from the top and bottom of the nanowire. Close to the top the shell is thin as it will have had little time to form during the growth, while closer to the bottom a much thicker shell is expected. The two areas analysed for this nanowire are separated by roughly 2 µm along the nanowire, but differ by only about 20

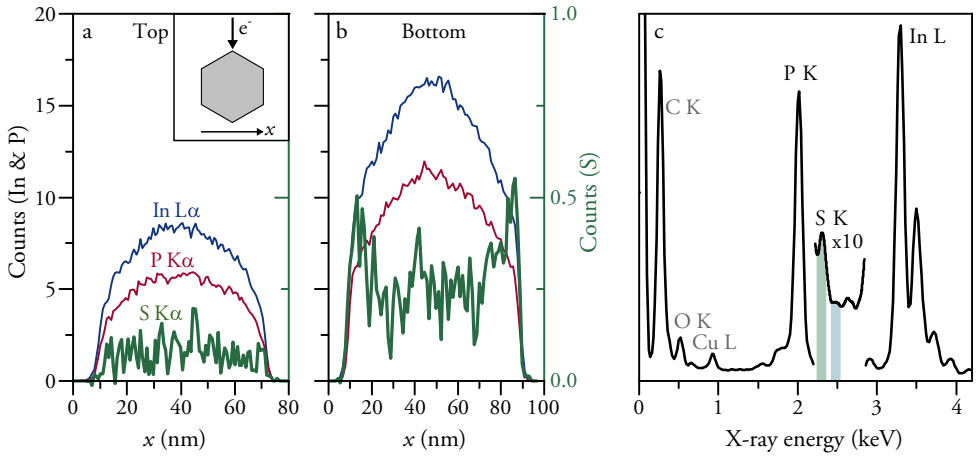

Figure 6.3: Qualitative elemental profiles from XEDS across a highly S doped InP nanowire (a) close to the top, and (b) closer to the bottom. The latter indicates the presence of a shell with higher doping than the core. (c) EDX spectrum from the bottom region showing the small S Kα peak riding on the tail of the much larger P Kα peak. To make the profiles in (a) and (b) a background (blue) was subtracted from the S peak (green).

nm in diameter. The low S content makes it necessary to use long acquisition times in order to produce a useful signal. On the other hand, the shell is quite thin and InP is one of the most beam sensitive III-V materials. It is therefore essential to distribute the dose over as large an area as possible. The low dose acquisition was in this case accomplished by acquiring the X-ray spectrum images from a large area along the nanowire, and then summing them in the axial direction. The dose for each point in the radial profile is in this way spread along the length of the nanowire. In order to provide the qualitative profiles of the S content shown in figure 6.3a–b, a background was subtracted from the S Kα peak as shown in 6.3c. Without this background subtraction the S content would appear to follow the P content closely as many of the counts in the small S Kα peak stem from the tail of the much larger P Kα peak. A more stringent analysis was also attempted by fitting the S and P peaks with Gaussian functions, but this gave no additional benefits due to the very noisy spectra.

The resulting radial profiles show in a qualitative way that close to the top of the nanowire the S concentration is too low for any radial variation to be distinguished from the noise. Closer to the bottom there is however a large increase in the S signal towards the edges. In contrast, the In and P signals are always decreasing towards the edges, as is expected from the hexagonal cross section of the nanowire shown in the inset in figure 6.3a. The different behaviour of the profiles at the edges indicates a greater concentration of S in the shell than in the core. The low signal however prohibits any quantitative measurement of this difference in doping from being made.

6.2 Plasmon Chemical Shift

The strength of XEDS is that it can evaluate all elements in the sample independently, but the downside is that only a small fraction of the generated signal can be collected. Even in the newest electron microscopes dedicated to microanalysis by XEDS, the multiple detectors only cover a solid angle of 0.9 sr.[136] In order to achieve accurate quantifications rather long acquisition times are therefore needed, which might not be possible for beam sensitive samples. EELS generally has a higher collection efficiency but many of the elements in III-V materials do not produce sharp, easily utilized core-loss edges. For many material systems the energy of the bulk plasmon can also provide insight into the composition and is easier to measure, as the primary electrons are much more likely to excite plasmons than core-loss events.[47] The relatively large plasmon signal coupled with the high collection efficiency of EELS allows for accurate measurements of the plasmon energy, E_p, even from short exposures. The size of the plasmon chemical shift varies depending on the materials system. For $Al_xIn_{1-x}N$ the energy of the bulk plasmon shifts from about 20.5 to 15.0 eV over the composition range,[147] while in $InAs_{1-x}P_x$ it only shifts from 14.0 to 14.7 eV.[148] As a general approximation the magnitude of the plasmon chemical shift follows the magnitude of the lattice parameter change, with smaller lattice parameters being linked to higher bulk plasmon energies.

In some cases there are more benefits to using the plasmon chemical shift instead of XEDS than a reduced dose. Figure 6.4a shows a STEM-HAADF image of an InP-AlP heterostructure nanowire which is covered by a roughly 10 nm thick layer of amorphous aluminium oxide. Since the nanowire itself is only about 30 nm in diameter the oxide shell constitutes a relatively large obstacle for the characterization. In an EDX spectrum it would not be possible to separate the aluminium in the oxide from the aluminium in the $Al_xIn_{1-x}P$ transition region between the two materials. In the low-loss EEL spectrum in figure 6.4b on the other hand, the bulk plasmon of the crystalline semiconductor is distinctly different from the plasmon of the amorphous oxide. Moving the electron beam over the transition region, the sharper plasmon peak from the crystalline material can be seen to shift in energy from approximately 14.3 to 16.3 eV as illustrated in 6.4c. By fitting the low-loss region with two Gaussian functions and a linear background it is possible to accurately extract the plasmon energy E_p and map its shift over the heterojunction, as shown in 6.4d. The standard deviation of E_p in the pure InP region is less than 0.02 eV, which corresponds to less than half a pixel in the EEL spectrum.

There are some complications to using the plasmon chemical shift for compositional analysis of nanowires. The energy of the plasmon in III-V nanowires is often observed to be different from the corresponding bulk material. This difference might be related to the presence of various polytypes in the nanowires, which do not exist in the bulk samples.[148] The difference between bulk and nanowire samples makes it difficult to use external standards or reference values for converting the measured plasmon energies

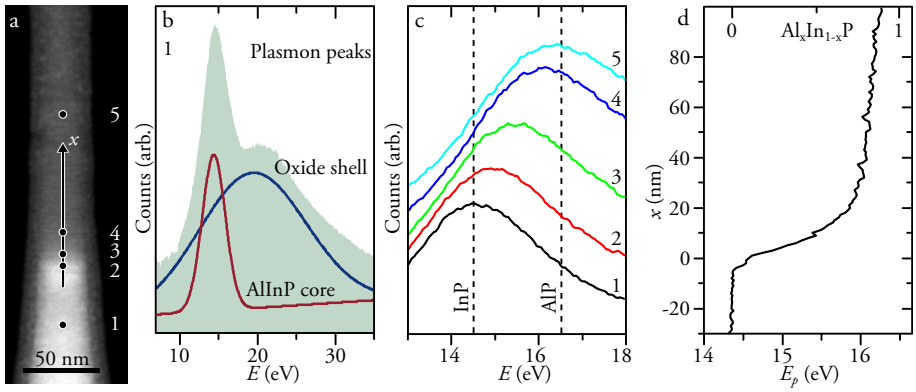

Figure 6.4: (a) STEM-HAADF overview image of an InP-AlP heterojunction embedded in amorphous aluminium oxide. (b) Low-loss EEL spectrum recorded from point 1 with two Gaussian functions fitted for the partially overlapping crystalline InP and amorphous aluminium oxide plasmon peaks. (c) Comparison of the plasmon peaks of the crystalline material from the five points indicated in (a), showing a 2 eV shift from InP to AlP. (d) Line profile with 1 nm sampling of the plasmon energy E_p along x, as marked in (a).

to a composition. If the compositions at the start and end of the transition region are known or can be determined by some other method this problem can be circumvented. The compositional profile in 6.4d was for example validated using local lattice parameter measurements.

Another problem for the plasmon chemical shift method is that the energy of the bulk plasmon is affected not only by the composition, but also by strain. The energy of the bulk plasmon is related to the density of the oscillating electrons. A change in the unit cell volume due to strain will therefore change the plasmon energy even if the composition is unchanged.[149] The errors in the determined composition should be small for material systems with large plasmon chemical shifts, as the change in plasmon energy with strain is this case small compared to the change with composition. However, large plasmon chemical shifts are often associated with large changes in lattice parameter, meaning that the strain is potentially large in these material systems. It should be noted that strain in one direction does not necessarily lead to a change in unit cell volume of the same magnitude, as compression in one direction might be compensated by an extension in the other. Even so, one should be careful when interpreting shifts in the plasmon energy in regions of the sample where the strain is large. For very sharp interfaces the delocalized nature of the plasmon oscillations, which can be generated up to about two nanometres away from the impinging electron, should also be kept in mind.[148]

6.3 Local Lattice Parameter Measurements

Local lattice parameter measurements are often called strain measurements, but this is not entirely correct in my opinion. Strain is a deviation from the relaxed lattice caused by some external or internal stress applied to the material. The local changes in lattice parameter that are measured by the methods discussed in this section can also be related to changes in composition. Only if we know the composition can we relate the changes in local lattice parameter to strain, and conversely we need to know the strain in order to relate the local lattice parameter to composition. For nanowires, the planes perpendicular to the growth direction are not pinned at the surface, and the lattice can relax efficiently in this direction. Simulations indicate that the spacing between these planes will relax to the bulk value only a few nanometres after a sharp heterojunction.[150]

Local lattice parameter measurements are particularly useful for ternaries where the lattice parameter can be directly related to composition. Often the lattice parameter is simply assumed to vary linearly throughout the composition range. This approximation is known as Vegard's law. Calculations using density functional theory show that the deviation from linearity is stronger the larger is the difference in covalent radii for the two elements being exchanged. For most material systems a smaller unit cell volume is predicted by these calculations than by Vegard's law. For AlInAs the maximum deviation in unit cell volume is predicted to be about 0.002 nm^3, which corresponds to a deviation in lattice parameter of only about 0.002 nm.[151] If the AlInAs composition had been estimated from a measured lattice parameter using Vegard's law, the error would be less than 1 % in this worst case scenario.

There are many different methods available in TEM for precise measurements of the local lattice parameter at high spatial resolution. The different methods and their strengths and weaknesses are listed by Beche et al.[152] To summarize the main points, diffraction based methods are very accurate and can be used over very large areas on the sample, but are not easily used for mapping at high spatial resolution. Dark field holography can be used for mapping, but requires specialized equipment and expertise. Analysis of high resolution images is yet another option, provided that the fringes in the images correspond in spacing, if not in exact position, to actual atomic planes in the sample. Image analysis methods have limited field of view compared to the two other classes of methods mentioned before, and generally require thinner samples. These limitations are not very detrimental to the analysis of nanowires, which are usually thin enough for high resolution imaging. The thinnest nanowires are in fact excellent for high resolution imaging, but on the other hand produce very little signal in for example XEDS. Local lattice parameter measurements from high resolution images are therefore an excellent complement to the other techniques discussed in this chapter. The small field of view in high resolution images is usually also not a problem since the compositional grading in nanowires typically occurs over lengths comparable to the nanowire

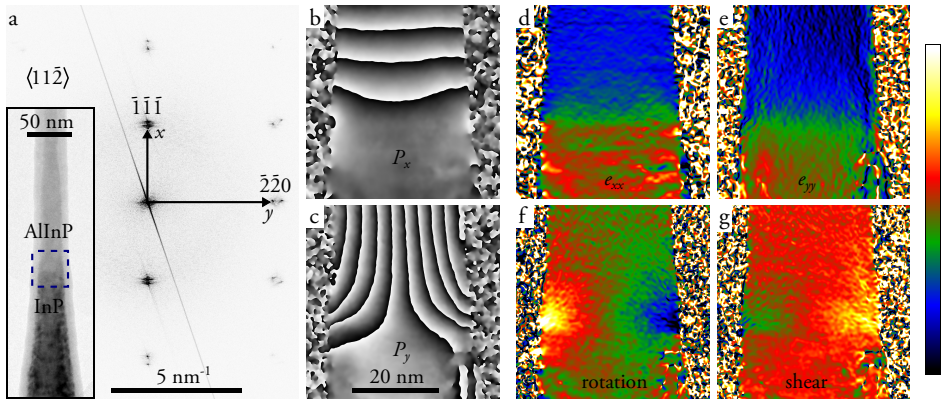

Figure 6.5: (a) Diffractogram of the InP to AlP transition region marked in the inset, with the two reflections used for GPA marked. (b–c) Phase images calculated for the $\bar{1}\bar{1}\bar{1}$ reflection in the x direction, and for the $\bar{2}\bar{2}0$ reflection in the y direction, respectively. (d–e) Local lattice parameter maps in the *x* and *y* directions. The scale represents changes of 0.92 to 1.08 compared to the reference InP lattice. (f) Lattice rotation map. The scale represents rotations of -14° to 14°. (g) Lattice shear map. The scale represents shears of -0.25 to 0.25 InP unit cells.

diameter.

Many different methods have been developed for estimating the local lattice parameter from high resolution images, and most of them have been applied to III-V materials at some point. Pattern matching has been used to locate and determine the lattice distortion on a unit cell basis in InP quantum dots.[153] Peak-pair analysis, where the separations between pairs of contrast maxima are measured and compared to a reference area on the sample, has been used to measure the strain across the InAs-InP heterojunction in a nanowire.[150] Geometric phase analysis has been used to measure the strain in Ge nanowires grown on Si substrates,[154] and the strain across InAs-InSb[155] and GaN-GaInN[156] nanowire heterojunctions. Of these three methods, the geometric phase analysis (GPA) method stands out as particularly easy to implement and is not computationally demanding. The full, rigorous description of the GPA method is given by Hÿtch et al.[157]

The use of GPA to analyse a heterojunction is illustrated in figure 6.5 for a InP-AlP heterostructure nanowire. The nanowire shown in the inset in figure 6.5a originates from the same sample as the nanowire used in figure 6.4 to illustrate the plasmon chemical shift. GPA is somewhat related to the simpler method of applying a mask to a reflection in the diffractogram of a high resolution image, inverse transforming, and observing the distribution of the corresponding fringe in the image (hereafter referred to as Fourier filtering). To make the workings of GPA clearer and to highlight the differences to Fourier filtering, I will briefly describe the different steps in the algorithm below, using a simple 1D image as an example. For a 1D image containing a single set of fringes

with spacing $d = 1/g$, the contrast is simply $c(x) = \cos 2\pi gx$. The diffractogram of this image is given by equation 6.1.

$$C(k) = \mathcal{F} \cos 2\pi gx = \frac{1}{2}\left[\delta(k-g) + \delta(k+g)\right] \tag{6.1}$$

In the first step, a mask M is applied to the diffractogram, covering only the reflection centred on g and its immediate surroundings, as shown in equation 6.2. The reflections used for the analysis of the InP-AlP transition are denoted by x and y in figure 6.5a. If the original image contains other fringes or a background, these are removed from the image by the filter at this stage. Inverse Fourier transforming the filtered diffractogram yields a complex image, $c_{filt.}$, as shown in equation 6.3.

$$MC(k) = \frac{1}{2}\delta(k+g) \tag{6.2}$$

$$c_{filt.} = \mathcal{F}^{-1} MC = \exp\left[\pi igx\right] \tag{6.3}$$

The phase of $c_{filt.}$ is the geometric phase, P'_g, of the fringes associated with g and can easily be converted into the actual fringe spacing by simple differentiation, as shown in equation 6.5. In figure 6.5b–c the geometric phase from the reference InP lattice has been subtracted to yield the relative geometric phase P_g, which more clearly shows the change in lattice parameter over the heterojunction.

$$P'_g = \angle c_{filt.} = \pi gx \tag{6.4}$$

$$\frac{\mathrm{d}}{\mathrm{d}x}\frac{P'_g}{\pi} = g \tag{6.5}$$

The final results of the geometric phase analysis of the InP-AlP heterojunction are shown in figure 6.5d–g. These local lattice parameter maps have been calculated by differentiating the two geometric phase images according to equations 6.6–6.9. The relative changes in lattice parameter are precisely measured by the GPA method provided, of course, that the fringes correctly represent the lattice. The absolute values for the lattice parameter however depend on the magnification calibration of the microscope, which is not very reliable. In order to improve the accuracy, a reference area in the image is needed where the lattice parameter is known, or at least can safely be assumed to have a certain value. In the maps in figure 6.5 the pure InP segment was used for this purpose. The contraction of the lattice, caused by the abrupt increase in Al at the beginning of the transition to AlP, forces the lattice to bend inwards at the heterojunction perimeter, as shown in figure 6.5f. The bending of the lattice at the surface of the nanowire demonstrates that the strain distribution is not radially homogeneous. In

areas with large radial variations the maps are the result of overlaid projections of many slightly different lattices and need to be interpreted carefully.

$$e_{xx} = \frac{\partial P_x}{\partial x} \tag{6.6}$$

$$e_{yy} = \frac{\partial P_y}{\partial y} \tag{6.7}$$

$$\text{Rotation} = \frac{1}{2}\left(\frac{\partial P_x}{\partial y} - \frac{\partial P_y}{\partial x}\right) \tag{6.8}$$

$$\text{Shear} = \frac{1}{2}\left(\frac{\partial P_x}{\partial y} + \frac{\partial P_y}{\partial x}\right) \tag{6.9}$$

In order to show why GPA is superior to Fourier filtering we return to the 1D image and look more closely at $c_{filt.}$. The previous description in this section hopefully makes it clear how GPA quantitatively maps the variation in fringe spacing across the image using the phase of $c_{filt.}$. In Fourier filtering it is instead the amplitude of $c_{filt.}$ that is used. All fringes selected by the mask will however contribute equally to the amplitude, meaning that each Fourier filtered image will include a whole range of fringes with slightly different spacings. In order to increase the selectivity of the $c_{filt.}$ amplitude, it is necessary to apply a smaller mask. However, applying a mask M in the diffractogram is equal to convoluting the image with the inverse Fourier transform of the mask, m. The widths of M and m are inversely related, so applying a smaller M will blur of the image more severely and make the location of the fringes more uncertain. For this reason there is a compromise in Fourier filtering between precision and spatial resolution, making the method unsuitable for analysing compositional grading.

Chapter 7

In-Situ Growth

As was mentioned in the previous chapter, TEM usually only provides information on the fully formed structures, from which we have to infer what occurred during growth. Ideally we would like to instead carry out time-resolved observations *in-situ* under the growth conditions. However, the presence of gases and the speed of the growth process make this impossible for most characterization techniques. Instead a compromise must be found between conditions that are compatible with the characterization technique and conditions that result in small, or at least well understood, differences compared to normal growth. In the case of nanowire growth *in-situ* observation has been accomplished for infra-red spectroscopy,[158] X-ray diffraction,[159, 160] and indeed TEM.

The transmission electron microscope column is normally evacuated to prevent the electrons from being scattered before reaching the sample and to prevent damage to the gun. In order to study reactions involving gases *in-situ*, such as nanowire growth, the requirement on vacuum must of course be relaxed. There are basically two routes for allowing gases at the sample: differential pumping and windowed cells. The former involves a modification of the actual microscope, which is then referred to as an environmental transmission electron microscope, to allow gases directly into the pole-piece gap. A set of pressure limiting apertures reduce the diffusion of gases from the pole-piece area into the rest of the microscope, where extra vacuum pumps maintain the normal, low pressure. This design allows a huge difference in pressure between the sample area and the gun, and confines most of the gas to the 5–7 mm pole-piece gap around the sample. Heat is supplied by the sample holder, which can be chosen freely as the gases are handled by the microscope itself.[161]

The windowed cell method instead encloses the sample in a small cell with electron transparent windows, completely sealing the reactor volume from the vacuum in the microscope column. In order to accommodate the cell – including heating and inlets and outlets for the gases – a special, dedicated holder is required. This holder can then, at least in principle, be used in any microscope without modification. The windows

above and below the sample, each some tens of nanometres thick, will inevitably affect the electrons to some degree and add a background to the images and spectra recorded from the enclosed material. On the other hand, the windows can withstand pressure differences of over one atmosphere while the environmental TEM (ETEM) method is limited to much lower pressures of about 2×10^3 Pa.[162] As the gases come into direct contact with the microscope interior in the ETEM method, gases which leave residues or corrode the linings and seals, should be avoided. For windowed cells there is in principle no limitation to what gases can be introduced, but due to the possibility of leaks and broken windows one still must be careful.

All previous *in-situ* TEM observations of semiconductor nanowire growth have been made using the ETEM method. So far the group IV materials Si and Ge, and the III-Ga compounds GaN,[163] GaP,[63] and GaAs have been studied. It would be useful to expand this list to include more compounds since there are differences in their growth behaviour. In particular, different group III elements should be tested as they dissolve in the gold seed particle to a large extent, which should affect its properties. Antimony and some dopants, such as zinc, are also known to have a large influence on the growth by affecting the various interface energies, and would also be interesting for future *in-situ* experiments. Compared to normal MOVPE the *in-situ* growths have all been carried out at low pressures, and have used undiluted precursors or precursors at high concentrations in He instead of low concentrations in H_2. At least for group IV nanowires, H_2 is known to affect the growth by modifying surface energies.[158] Despite the limited number of compounds that have been tested and the differences compared to normal growth conditions, much insight into nanowire growth has been gained from *in-situ* TEM as has been mentioned throughout the previous chapters.

The *in-situ* studies mentioned in this thesis have used one of two different sample geometries. The most common geometry uses a small substrate as an epitaxial support, where one facet parallel to the electron beam has been decorated by either seed particles or pre-grown nanowire stubs. With this sample geometry it is possible for the operator to choose the viewing direction of the growing nanowires by orienting the substrate in a suitable way. Often a $\langle 110 \rangle$ viewing direction is desired so as to have the $\{111\}$ growth planes parallel, and the growth direction perpendicular, to the electron beam. The non-overlapping projection of the growth facet in this viewing direction has allowed detailed studies of the kinetics of forming new bilayers,[60] as well as the morphology[65] and compositional grading[72, 73] of heterostructures. The pre-defined orientation is critical for achieving high resolution images of the growth,[62] but also helps in the characterization of smaller, dynamic facets at lower resolution.[63] The downside of this sample geometry is that the nucleation and initial growth of the nanowires can be obscured by the strong Fresnel fringes from the thick substrate.

The other possible sample geometry instead uses seed particles placed directly on an electron transparent membrane. This sample geometry makes it possible to study the initial nucleation of semiconductor material from the seed particles.[164] By using

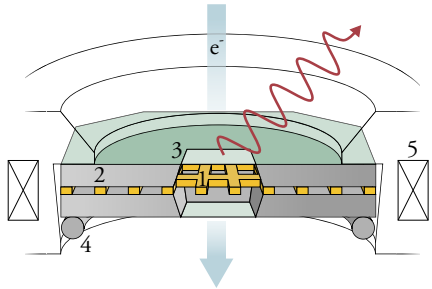

Figure 7.1: (a) Illustration of the closed *in-situ* cell seen in cross section. The source material and gold particles are supported by a holey carbon gold grid (1) which is enclosed by two silicon dies (2), forming a small reactor in the centre. The electron beam, and X-rays generated from the sample, can pass through the thin SiN windows (3). The whole cell is clamped into place by a metal clip (4) and heated by a coil at the perimeter (5).

an amorphous material as the membrane there is no epitaxial guiding for the initial nanowire growth, which could make this method interesting for gaining insight into the initial stages of the growth in aerotaxy. For studying the continued growth this geometry has the disadvantage that the nanowires are randomly oriented with respect to the beam. There will at most be some tendency for the nanowires to grow along the surface of the membrane, rather than at an angle to it, making some viewing directions more likely than others. Only rarely can one expect a low index viewing direction like $\langle 110 \rangle$, but the growth facet will often be roughly parallel to the electron beam. This preference in orientation has made it possible to study the formation of bilayers[59] and facet dynamics[64] at high resolution also with this sample geometry.

Environmental transmission electron microscopes and holders for windowed cells are only available at a few laboratories in the world, and fewer still can be used for *in-situ* studies of vapour phase epitaxy processes. For this reason we developed a closed cell for use with a standard heating holder in a conventional transmission electron microscope. The use of this closed cell is described in paper VI for the study of gold seeded InAs nanowire growth. A schematic of the cell, in place in the heating holder, is shown in figure 7.1. Compared to the more advanced windowed cells, the closed cell lacks gas inlets and outlets, and is heated externally by a resistive heating coil in the holder. Similar to the windowed cell the reactor volume is enclosed between two electron transparent windows, in this case consisting of 20 nm thick amorphous SiN_x. Enclosed within the cell is a gold grid which acts as a sealing gasket, heat conductor, and support for a holey carbon film. The holey carbon film in turn supports seed particles and small fragments of III-V. Upon heating the cell, the III-V fragments closer to the hot gold grid will evaporate and supply the seed particles with a flow of growth species. Similar principles have been used for the synthesis of InAs nanowires in physical vapour deposi-

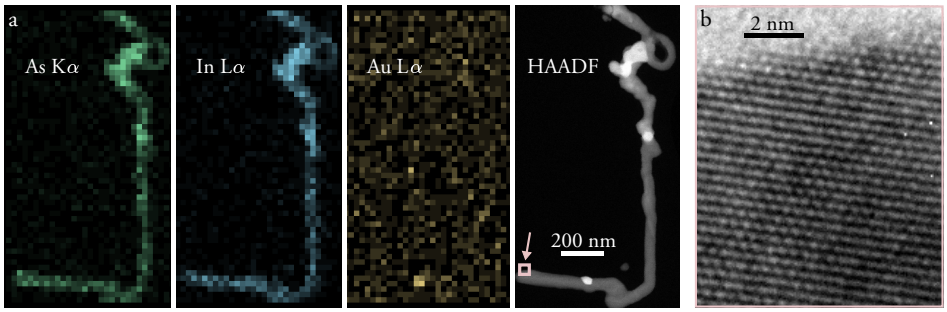

Figure 7.2: (a) XEDS maps calculated from the In Lα, As Kα, and Au Lα counts, together with an STEM-HAADF image of the same area. A quantitative analysis indicates 51 at% In and 49 at% As, which is consistent with InAs given the accuracy of the XEDS quantification. The area marked in the HAADF image with an arrow indicates the region where the high resolution TEM image in (b) was recorded. Both XEDS maps and the high resolution images where recorded from material enclosed in an unheated closed cell.

tion.[165] The temperature of the closed cell determines both the growth temperature and the flux of growth species. The flux of the growth species can to some extent also be controlled independently from the growth temperature by using the focused electron beam to locally heat the III-V fragments. For an unheated cell it is possible to acquire both high resolution images and EDX spectra from the enclosed material, as illustrated in figure 7.2.

In order to provide an example of what can be studied using the closed cell a series of bright field images, extracted from a movie recorded with 15 frames per second, are shown in figure 7.3. The temperature of the cell during this movie, as measured by a thermocouple in the holder, was 620 °C. Just prior to the first frame a nearby InAs fragment had been heated by the electron beam, providing a burst of evaporated material. The increased flow of In reaching the gold particle caused it to expand, and thereby also expanded the nanowire diameter from 52 to 55 nm. During the expansion of the particle, several twins formed on one of the inclined {111} facets on the side of the nanowire (marked with arrows in the 29.3 s panel). As the nanowire continued to grow, these inclined twins eventually reached the opposite side of the nanowire where they pinned the growth front (at the location marked with an arrow in the 51.0 s panel). At this point new material could mainly be added to the outermost twin, which forced the growth front to turn. After a rotation of about 130° the gold particle was able to wet a new {111}B facet and could proceed to grow straight in this direction.

Changes in growth direction, forming kinks in the nanowire, have been observed by ETEM also for Si nanowires.[166, 167] Unlike the kinking process outlined briefly for InAs in this section, the change in growth direction for Si nanowires is not always associated with the formation of inclined twins. However, in the specific case of a

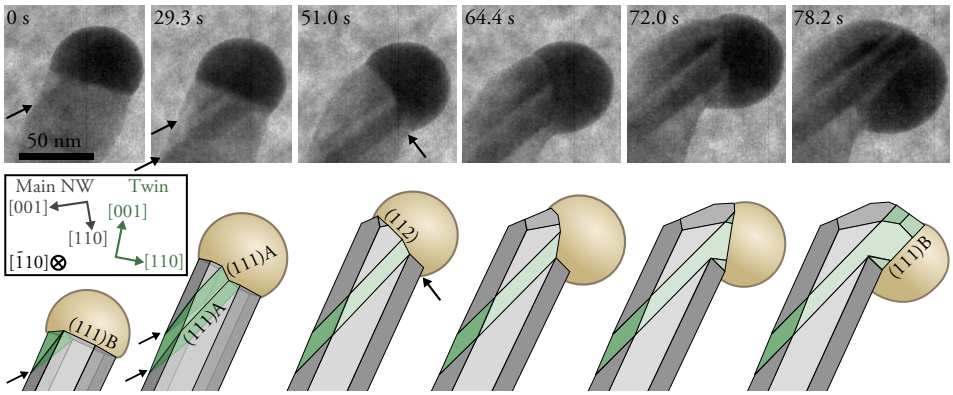

Figure 7.3: A time series of TEM bright field images recorded at 620 °C showing an InAs nanowire in the process of changing growth direction as a set of inclined twins (marked with arrows in the 29.3 s panel) reach the opposite side of the nanowire and pin the growth front (marked with arrow in the 51.0 s panel).

sudden expansion of the seed particle, inclined twins have been observed also for Si nanowires.[168] Also in this case did the inclined twin eventually lead to a change in growth direction, but the kinking process is not described in detail. The change in growth direction likely proceeds somewhat different for Si than for InAs as the former has a diamond crystal structure type rather than zincblende, and therefore has more equivalent {111} facets for the growth to choose from.

The closed cell does have several drawbacks. The growth conditions are not well known and were only estimated from the temperature measured at the perimeter of the cell. Potentially, EELS could be used to measure the local concentration of the growth species. Comparing concentrations measured on the carbon film and over a hole could in addition provide clues as to whether the different growth species are transported mainly by surface or vapour phase diffusion. Either way, the results will still be difficult to transfer to normal MOVPE growth as the conditions are very different. In addition, the lack of a substrate for providing epitaxial guidance means that the nanowires will very rarely have an orientation suitable for high resolution imaging. The particular nanowire shown in 7.3 was for example estimated, based on the projected width of the twin boundaries, to be about 10° titled away from a ⟨110⟩ orientation. Despite these limitations, the closed cell did enable the first *in-situ* TEM observations of growing InAs nanowires with no modification to either the microscope column or the sample holder. Even so, the more advanced windowed cells and environmental transmission electron microscopes do offer huge advantages in that they can use normal MOVPE precursors and offer independent control of the temperature and pressures, including the ratio between the different precursors.

With the introduction of sensitive cameras with fast read out, high brightness elec-

tron guns, and environmental microscopes and cells capable of handling higher pressures, there are increasing opportunities for studying nanowire growth under relevant conditions. One issue which cannot be circumvented is that the electron beam will always affect the reactions it is probing to some degree. The surfaces of illuminated crystals can also be changed, affecting how new material is added to them during crystal growth.[161] In order to resolve smaller features in the images, a higher electron dose is required on the sample. If the images are to be recorded rapidly as well in order to image rapidly occurring processes, a high dose rate is also required. Under such conditions the effects from the electron beam are potentially large. The nature and extent of the influence of the electron beam can be estimated by comparing the areas imaged during the *in-situ* experiment with areas that were not illuminated. In the case of the InAs nanowires grown in the closed cell, the variation between the individual nanowires is however too large to draw any conclusions about the influence of the electron beam. Some recent reports indicate that there is a more fundamental limit to high spatial and time resolution in *in-situ* TEM, with the resolution decreasing with increasing dose rates[169] or beam currents.[170] Neither of these reports explore the consequences for high time resolution *in-situ* TEM, but the requirement of lower dose rates implies that longer exposure times will be needed to achieve high resolution at high gas pressures. The underlying mechanism is currently not well understood, but ionization of the gas molecules is one candidate. Further studies are needed to determine whether, or to what extent, this effect will limit *in-situ* TEM studies of growing nanowires at high time and spatial resolution.

Chapter 8

Conclusions

The sensitivity of the crystal structure in nanowires to the growth conditions means that there is always a need for characterization by high resolution transmission electron microscopy. With the increasing interest in growth on non-native substrates and growth methods foregoing the use of substrates altogether, polarity is becoming an increasingly important parameter to determine. Convergent beam electron diffraction is very versatile for this purpose, being able to determine polarity for most III-V materials and crystal structure types. The low requirements on the electron microscope makes CBED particularly suitable for screening a large number of nanowires. If an inversion boundary is found, it will however be useful to switch to a different method in order to image the local atomic arrangement at the interface. CBED is for instance not able to tell whether the inversion boundary contains homoatomic bonds or segregated impurity or dopant atoms. Focal series reconstruction could fill this complementary role, but requires very detailed knowledge of the local sample orientation before the resulting reconstructed object wavefunction can be interpreted accurately. Most likely, STEM imaging techniques would be better suited for this purpose.

Polarity measurements from GaAs nanowires grown without a substrate – using the aerotaxy method – interestingly indicate that all growths in $\langle 111 \rangle$ directions occur in the As terminated $\langle 111 \rangle$B directions. This indicates that the very strong preference for the B growth direction is determined by the interplay between the surface energies of the seed particle and the nanowire, and does not depend on the substrate. The use of (111)B in substrates in normal growth only ensures that the vertical direction and the favoured growth direction are the same.

Most nanowires intended for use in electronic devices will contain heterostructures with several materials or doping, both of which require analysis of the composition in addition to the crystal structure. Energy dispersive X-ray spectroscopy is in most situations the first method to perform as it can detect and quantify most elements used in III-V materials. Planning the XEDS acquisition to spread the dose over the structure

in an optimal way is crucial for attaining the highest accuracy, sensitivity and spatial resolution. For example, only by summing radial profiles along the length of an InP nanowire was it possible to detect the increased incorporation of S dopant atoms in the unintentional shell. Without such measures, InP in particular will be severely damaged before a sufficient X-ray signal can be collected. For ternary materials, plasmon chemical shift measurements by EELS are a very good alternative to XEDS and result in robust quantifications even with short acquisition times. In addition, even if the electron beam passes through several materials, information about the individual materials can still be extracted as long as their plasmon peaks are distinguishable. Local lattice parameter measurements, which are commonly referred to as strain measurements, can fulfil a similar role.

Understanding the dynamic processes occurring during growth is essential for connecting the structure and composition of the fully formed nanowires with the growth conditions. With post-growth characterization, these dynamic processes can usually only be inferred after varying the growth conditions or terminating the growth at various stages. However, even if the growth is terminated abruptly one should be careful not to interpret the resulting nanowires as representing a frozen moment in time. Only by accounting for all the changes occurring during the growth termination, such as material precipitating from the seed particle, can the actual state of the nanowire during growth be reconstructed. Using this line of reasoning in the case of the transition from GaSb to InAs, the composition of the seed particle was tracked over time. As Ga in the seed particle was expelled in favour of In until none remained, the sharp Ga-to-In transition observed in the fully formed nanowires can be explained.

Observing the growth *in-situ* by TEM provides another opportunity for gaining knowledge of the growth dynamics. Heating InAs fragments and gold seed particles enclosed in a completely closed cell with electron transparent windows allowed real time observations of growing nanowires to be recorded. Intermittently, between the periods of growth at high temperatures, it also proved possible to record high resolution images and XEDS compositional maps. Such closed cells should be compatible with any electron microscope and III-V compound. The growth conditions are however difficult to both control and measure, and differ from MOVPE in terms of pressures and precursor chemistry. The observations made using such closed cells are therefore difficult to transfer to the normal *ex-situ* growths.

8.1 Outlook

The goal of locating and identifying all atoms in the sample does not seem as far-fetched now as it was before the development of aberration corrected STEM. Quantitative analysis of the contrast in HAADF images in combination with discrete tomography has already been used to determine the 3D structure of small metal particles at the atomic scale.[171,172] Atomic-column resolved EELS[123] or XEDS[122] can hopefully soon be included in such tomographic reconstructions in order to provide also the composition or to identify single dopant atoms in the structure. If this approach proves feasible, the characterization of nanowires with complex dopant or compositional profiles would benefit enormously.

Although the combination of atomic-column resolved spectroscopies and tomography would be very powerful, it will not be the be-all and end-all of nanowire characterization. Firstly, it will require too much time and resources per nanowire that is analysed. Normally, several nanowires from several samples need to be studied and compared to be able to relate the observed features to the growth conditions, or to the performance of the nanowires in a finished device. Secondly, not all materials are sturdy enough to withstand the large electron doses needed to gather the necessary signal for the spectroscopies or the tomography. A large variety of electron microscopy methods, such as those presented in this thesis, will therefore be needed also in the future. Other characterization techniques such as atom probe tomography[137] or various surface techniques[173] can of course provide complementary information about the samples. Correlating results from the various methods – TEM based or not – on a nanowire to nanowire basis will be particularly interesting.

This thesis is very much focused on the atomic structure of the nanowires, but the electronic structure is of course also important. Electron microscopy based methods can be used also for this purpose, and hopefully the use of such methods for the characterization of nanowires will become more common. Electron holography has for instance been able to map the active dopants, as opposed to simply all dopants, in Si nanowires.[174] The use of monochromators is increasing the energy resolution in EELS and is making it possible to resolve various band-to-band transitions involving very small energy losses. In affect this allows properties in the visible-light energy range to be measured with TEM spatial resolution.[175] At least for GaN it has for example been possible to measure the change in bandgap between zincblende and wurtzite using this method.[91] It would of course be interesting if such methods could also be applied to more materials and more polytypes.

Even with the advances in characterization capabilities, post-growth analysis will always miss the dynamic processes occurring during the growth. *In-situ* TEM observations have already provided much insight, and quite a few surprises, regarding the growth of nanowires. These results are perhaps especially impressive considering that the few environmental transmission electron microscopes used for studying semiconductor

crystal growth are old. Compared to newer microscopes they have rather low resolution and cannot handle very high gas pressures. A modern environmental transmission electron microscope suitably modified to allow the use of the dangerous MOVPE precursors should provide huge advances in *in-situ* capabilities.

With a state of the art environmental transmission electron microscope with high spatial and temporal resolution, it might for instance be possible to observe the very earliest stages of the nucleation of a new bilayer. Hopefully this will provide insight into the mechanisms behind polytypism. The possibility of performing compositional analysis by XEDS or EELS on growing nanowires would also be very useful. For example, the reservoir effect and the amount of group V atoms present in the seed particle could be explored in this way. Concerning the group V atoms, there are already indications from post-growth analyses that they are dissolved in small quantities in the seed particle during growth,[176] but this requires much further investigation.

Windowed cells might also prove useful for *in-situ* studies of nanowires by making it possible to bridge the entire pressure gap and observe the growth under actual MOVPE conditions. Without such experiments it can be difficult to know whether phenomena observed at lower pressures in a differentially pumped environmental microscope are relevant for conventional growths.

Populärvetenskaplig sammanfattning

För att utveckla och förbättra material krävs det ständigt ökade möjligheter att styra deras uppbyggnad på allt mindre skalor. Inom några områden har utvecklingen gått så långt att materialen behöver designas på nanometerskalan. En nanometer är en miljondels millimeter och rymmer knappt tio atomer. Det tydligaste exemplet på tillämpningar där design på nanometernivå är avgörande är antagligen halvledarkomponenter. Redan i mitten av 2000-talet kunde till exempel transistorer, de grundläggande komponenterna i en processor, tillverkas med beståndsdelar mindre än hundra nanometer. I dagsläget är kisel det mest använda halvledarmaterialet, till stor del på grund av att det är relativt billigt och enkelt att bearbeta. Att bara använda ett material är dock en begränsning och därför bedrivs mycket forskning på hur man kan komplettera kisel med andra halvledarmaterial. I takt med att halvledarkomponenterna blir mindre och mer komplicerade krävs allt mer detaljerade kunskaper om hur de är uppbyggda på allt mindre skala. Elektronmikroskopi är ett mycket viktigt verktyg för detta ändamålet, men måste ständigt utvecklas för nå upp till de ökande kraven. Den här avhandlingen handlar om hur nya metoder för karakterisering med hjälp av elektronmikroskopi kan appliceras på halvledarmaterial.

I elektronmikroskop belyses provet med elektroner istället för ljus (fotoner). Precis som fotoner har elektroner en våglängd och de kan fokuseras med hjälp av linser. I elektronmikroskop används dock magnetfält istället för glaslinser. Ett mikroskops upplösning bestäms i första hand av kvalitén på linserna, men den fundamentala begränsningen för upplösningen ligger i våglängden på belysningen. Mikroskop som använder synligt ljus, vilket motsvarar en våglängd på ca 500 nm, kan därmed inte särskilja föremål som är närmre varandra än ett par hundra nanometer. För att urskilja atomerna i ett prov krävs det ljuskällor med en våglängd på mindre än en nanometer. För fotoner med så pass kort våglängd går det inte att tillverka tillräckligt bra linser. De magnetiska linserna i ett elektronmikroskop kan däremot även fokusera elektroner med mycket korta våglängder. Figur 1 illustrerar en resa ner till atomnivå med hjälp av elektronmikroskop.

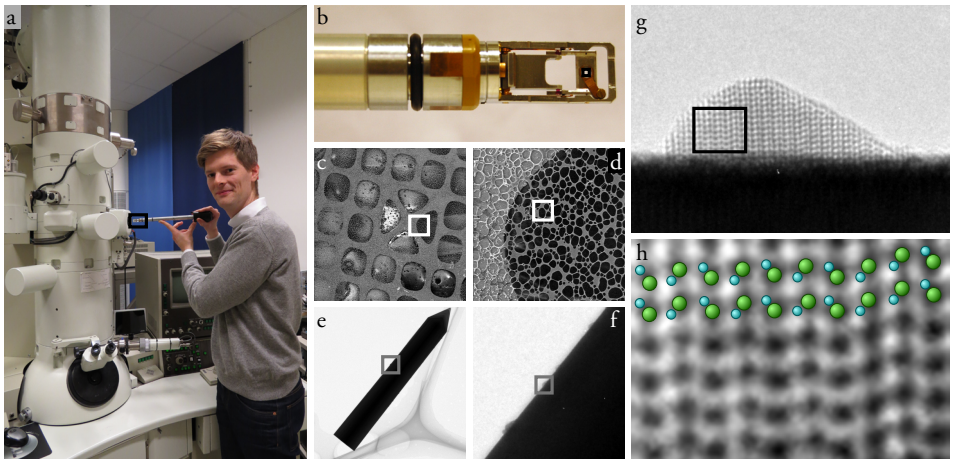

Figur 1: Från mikroskop ner till atomerna. Längderna som anges är asvtåndet kant till kant på bilden (1 mm = 1 000 µm = 1 000 000 nm). (a) Foto på det högupplösande transmissionselektronmikroskopet i Lund. (b) Spetsen på provhållaren, ca 6 cm. (c–d) Bilder tagna med svepelektronmikroskop på det finmaskiga kopparnätet och kolfilmen som provet ligger på, ca 300 µm respektive 40 µm. (e–f) Översiktsbilder tagna med transmissionselektronmikroskopet som visar en avlång galliumnitridkristall med små indiumnitridkristaller på sidan, ca 2 µm respektive 200 nm. (g) Högupplöst transmissionselektronmikroskopibild på en indiumnitridkristall, ca 10 nm. (h) Detalj på ca 3 nm ur bilden i (g) som visar hur mönstret i bilden är kopplad till atomernas position i kristallen.

Utgångspunkten är ett foto på författaren i färd med att föra in ett prov i det högupplösande transmissionselektronmikroskopet på kemicuntrum i Lund (a). Den övre delen av provhållaren är markerad med en ruta och visas i högre förstoring i nästa bildruta (b). Längst fram på provhållaren finns en öppning på 3 mm där ett finmaskigt kopparnät täckt med en mycket tunn kolfilm placeras, en så kallad gridd. Bild c är tagen med ett svepelektronmikroskop och visar mitten på kopparnätet där ett flertal hål syns som vart och ett är ungefär en tjugondels millimeter brett.

Zoomar vi in ytterligare på kanten på ett av hålen syns kolfilmen, som i sig också har mängder av oregelbundna hål, mycket tydligare (d). I en översiktsbild tagen med ett transmissionselektronmikroskop (e) får vi se den första skymten av själva provet: en förhållandevis stor och tjock kristall av galliumnitrid (GaN) som är ungefär en femhundradels millimeter lång. I bakgrunden syns kanten av ett hål i kolfilmen svagt. På sidorna på GaN-kristallen sitter ännu mindre kristaller av indiumnitrid (InN), som var och en är ungefär tio nanometer stora (f). I ännu högre förstoring av en sådan InN-kristall kan vi se att den inte är helt jämn, utan har en inre struktur (g). I den sista bilden (h) visas endast en liten del av InN kristallen som ser ut att bestå av en mängd svarta prickar på en ljus bakgrund: detta är kolumner av atomer. I övre delen av bilden

finns en modell över hur atomerna sitter i GaN-kristallen som förtydligar kopplingen mellan atomernas position i provet och de svarta prickarna i bilden. Avstånden mellan atomkolumnerna i bilden är mindre än en tredjedels nanometer och har blivit förstorade ungefär 15 miljoner gånger i den tryckta bilden jämfört med deras verkliga storlek.

I figur 1 förekommer två olika elektronmikroskopitekniker: svepelektronmikroskopi (SEM) och transmissionselektronmikroskopi (TEM). En kort förklaring av hur de fungerar ges nedan.

Svepelektronmikroskop använder sig av elektroner med förhållandevis lång våglängd och låg energi som fokuseras till en nanometerstor stråle på provet. Elektronerna från belysningen slår loss nya elektroner från provets yta som kan detekteras. Antalet elektroner som når detektorn utgör den signal som skapar bilderna och beror på hur många elektroner som slås loss från ytan, och hur ytan är riktad i förhållande till detektorn. I SEM byggs bilden upp punkt för punkt genom att strålen förflyttas (sveps) över provet.

Transmissionselektronmikroskop använder elektroner med mycket hög energi som skjuts igenom provet. Det är inte ovanligt att elektronerna i belysningen accelereras till upp mot 80 % av ljusets hastighet, men trots det krävs det mycket tunna prov för att elektronerna ska kunna ta sig igenom. Istället för att fokusera elektronerna till en punkt på provet som i SEM används istället en bred stråle. Efter provet bildas en skuggbild som projiceras på ett material som omvandlar elektronerna till synligt ljus. I TEM är det viktigt att tänka på att bilden visar en tvådimensionell projektion av provets tredimensionella struktur.

Galliumnitrid och indiumnitrid som visades i figur 1 är exempel på III-V halvledare. III-V halvledare är föreningar av grundämnen från grupp tre, framförallt gallium (Ga) eller indium (In), och grupp fem som utgörs av kväve (N), fosfor (P), arsenik (As) och antimon (Sb). Anledningen till att undersöka III-V halvledarna är att de har egenskaper som skulle kunna komplettera kisel (Si) i många tillämpningar. Ofta har de till exempel en bättre ledningsförmåga och är bättre på att ta upp och avge ljus än kisel. Kristallstrukturerna för dessa föreningarna är mycket snarlika varandra och skiljer sig i stort bara i avståndet mellan atomerna. I figur 2 illustreras kristallstrukturen för indiumfosfid (InP). Figur 2 försöker även illustrera att den tvådimensionella projektionen av kristallstrukturen blir enklare om man vrider kristallen i en viss riktning. Detta är inte bara användbart för att göra illustrationer, utan det är faktisk det man gör med de verkliga kristallerna inne i transmissionselektronmikroskopet.

På Lunds universitet bedrivs mycket forskning på att framställa III-V halvledare i form av nanotrådar. Nanotrådar är små avlånga kristaller med en diameter på ett tiotal nanometer och en längd på ett hundratal till ett tusental nanometer. Att framställa III-V halvledarna i just den här formen ger många fördelar utöver de bra egenskaper som själva materialen har. Till exempel blir det lättare att styra materialens ledningsförmåga med yttre påverkan från till exempel elektriska fält på grund av att nanotrådarnas är så pass tunna. Det går dessutom att kombinera olika material som i vanliga fall skulle få defekter på grund av att deras kristallstrukturer inte passar ihop helt perfekt. Just

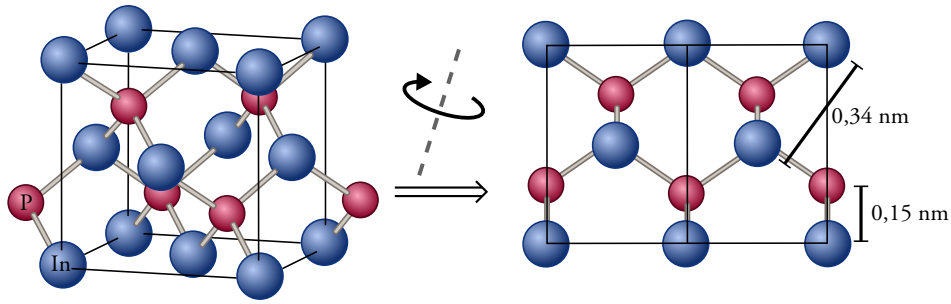

Figur 2: 3D model av kristallstrukturen för indiumfosfid (InP). Genom att rotera den tredimensionella modellen på ett lämpligt sätt hamnar atomerna i prydliga kolumner som ger en enklare tvådimensionell projektion. Detta är inte endast användbart för att göra illustrationer, utan är faktiskt det man gör med de verkliga kristallerna inne i mikroskopet. Två avstånd mellan atomkolumnerna anges i bilden och visar att mikroskopet behöver ha en upplösning på någon tiondels nanometer för att kunna avbilda kristallen.

denna egenskap skulle kunna göra det möjligt att kombinera III-V halvledarna med kisel. Basen i en framtida halvledarkomponent skulle då kunna utgöras av en kiselplatta som innehåller de grundläggande delarna medan de mest krävande processerna sker i nanotrådar av III-V halvledare som står på ytan. Eftersom kisel är så pass mycket billigare och mer etablerad än III-V halvledarna är detta nästan ett krav för att III-V halvledarna ska kunna komma till användning i en större omfattning.

Rent praktiskt så tillverkas nanotrådarna genom att små metallpartiklar placera på en platta (substrat) av ett halvledarmaterial, till exempel kisel eller en III-V halvledare. Sedan tillförs i gasfas beståndsdelarna till materialet man vill tillverka som fastnar på substratet och bilda ett nytt kristallint lager. Vid vissa betingelser bildas de nya lagren endast under metallpartiklarna som på så sätt bestämmer var och hur breda kristallerna som bildas blir. Efterhand som nya lager kristalliserar under metallpartiklarna lyfts de upp från ytan och nanotrådar växer på så sätt fram. I och med att kristallerna växer fram lager på lager på det här sättet kan de få andra strukturer än vad som vanligtvis är möjligt. Genom att ändra sammansättningen på gasen kan man även skapa övergångar mellan olika material i nanotrådarna. Detta är viktigt för många tillämpningar men innebär också en risk att material från en växtomgång dröjer sig kvar och förorenar de material man växer efteråt.

Som illustration över hur komplicerade nanotrådarna kan bli, och hur många olika aspekter det finns som behöver analyseras, visas en nanotråd bestående av indiumarsenid (InAs) och galliumantimonid (GaSb) i figur 3. Just den här kombinationen av material har rätt egenskaper för att bli transistorer som förbrukar mycket lite energi. För att detta ska lyckas krävs det dock att övergången mellan de två materialen sker på ett kontrollerbart sätt. I figur 3a visas en översiktsbild tagen med SEM. En av nanotrådarna har

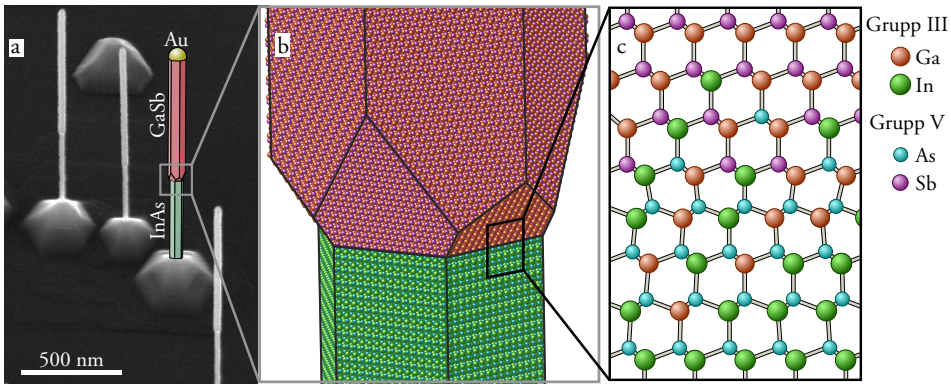

Figur 3: (a) Översiktsbild tagen med SEM på InAs-GaSb nanotrådar. En av nanotrådarna har ersatts med en 3D modell som visar var de två materialen finns och som dessutom visar den guldnanopartikel som användes för att växa fram nanotråden. (b) Mer detaljerad 3D modell över övergången från InAs till GaSb. (c) Struktur och sammansättning på atomlagren kring övergången. Lägg märke till att struktur, avstånd mellan atomerna och sammansättning ändras samtidigt.

ersatts med en 3D modell som också visas i högre förstoring i figur 3b. För att göra själva övergången ännu tydligare har nanotråden vridits och förstorats till 3c som bara visar åtta lager av atomer precis kring övergången. Om vi först fokuserar på kristallstrukturen, det vill säga atomernas positioner i förhållande till varandra, kan vi se att atomerna är ordnade på olika sätt i den övre och den undre halvan. Detta är exempel på två olika kristallstrukturer där den övre strukturtypen kallas zinkblände och är den vanligast förekommande strukturen för de här materialen. Strukturtypen i den undre halvan kallas wurtzit och bildas endast i tunna nanotrådar för det här materialet. Avstånden mellan atomerna ändras också genom övergången och är kortare i de mellersta lagren än överst och underst. Sett till sammansättningen är övergången inte så skarp som översiktsbilden i figur 3b antyder. Bytet från indium till gallium sker gradvis genom hela bilden i figur 3c och påbörjas mycket tidigare än bytet från arsenik till antimon.

Att karakterisera en så pass komplicerad övergång är svårt, men fullt möjligt tack vare transmissionselektronmikroskopi. Översiktsbilden i figur 4 är tagen med TEM och visar den övre delen av en InAs-GaSb nanotråd. Guldpartikeln i toppen på nanotråden är mycket mörkare än resten av strukturen i bilden eftersom guld är ett mycket tyngre grundämne än de övriga och sprider därmed fler elektroner så att de inte når kameran. De två segmenten av olika material kan redan nu identifieras på grund av att GaSb-segmentet är bredare. Detta är en effekt av att guldpartikeln tenderar att ta upp mer indium och gallium när antimon introduceras i växtkammaren. Kolfilmen som nanotråden ligger på skymtar fram i nedre vänstra hörnet men den mest intressanta delen av nanotråden, själva övergången, ligger fritt över ett hål. I InA-segmentet syns flera

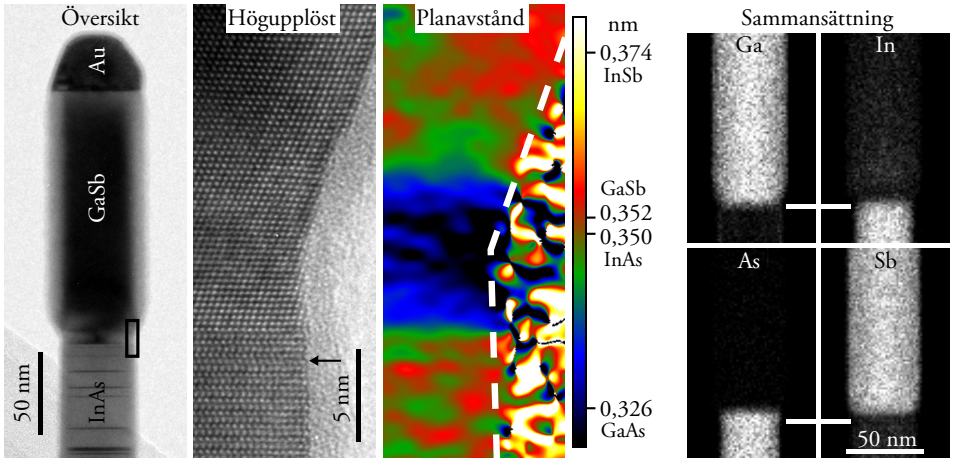

Figur 4: Översikt- och högupplöst TEM bild från en InAs-GaSb nanotråd. I den högupplösta bilden visar en pil ett atomlager som har förskjutits och därmed inte följer samma kristallstruktur som resten av InAs-segmentet. Det vertikala avståndet mellan de horisontella atomplanen visar att det i mitten finns ett segment som snarare liknar GaAs än InAs eller GaSb. Detta bekräftades då sammansättningen kartlades med hjälp av de röntgenstrålar som provet avger då det träffas av elektronerna från belysningen.

mörka, tvärgående linjer. Dessa får sin förklaring först i den högupplösta bilden där man kan se hur atomerna är ordnade. Precis som i modellen i figur 3 är strukturtypen i GaSb-segmentet zinkblände medan den i InAs-segmentet är wurtzit. I InAs-segmentet finns det dock undantag som inte har samma struktur som det övriga segmentet utan istället har zinkbländestruktur. Ett sådant atomlager är markerat med en pil i den högupplösta bilden. Det är dessa lager som syns som mörka streck i översiktsbilden.

Förutsatt att den högupplösta bilden är tagen med korrekt fokus stämmer positionerna för de mörka fläckarna i bilden överens med atomernas position i den verkliga nanotråden. Genom att mäta avståndet mellan prickarna kan därmed avstånden mellan atomerna bestämmas (som tur är kan den processen automatiseras, så ingen behöver sitta och mäta avstånden ett efter ett). Avståndet i höjdled mellan atomplanen som löper vågrätt igenom den högupplösta bilden visas i den färgkodade bilden i figur 4. Skalan löper från strax under 0,33 nm till strax över 0,37 nm vilket täcker in alla planavstånd man kan förvänta sig från de olika materialkombinationerna. Just i själva övergången finns det ett område på ca 5 nm som, utifrån planavstånden, liknar galliumarsenid (GaAs) snarare än InAs eller GaSb. För att kartlägga sammansättningen på ett mer entydigt sätt är det dock mer lämpligt att använda sveptransmissionselektronmikroskopi (STEM).

Sveptransmissionselektronmikroskopi har likheter både med SEM och TEM. Precis som i SEM fokuseras elektronerna till en liten punkt som sveps över provet, men i

likhet med TEM används elektroner med mycket hög energi som skjuts rakt igenom det tunna provet. Detta ger en stor förbättring i upplösning jämfört med SEM där de långsammare elektronerna sprids i provet över en yta som är mycket större än den ursprungliga elektronstrålen. En annan skillnad mot SEM är att bilden i huvudsak byggs upp genom att mäta hur många elektroner från strålen som passerar provet, istället för att mäta antalet elektroner som slås loss från provet. På sin väg genom provet kan elektronerna i strålen avge energi till atomerna. För att bli av med denna överskottsenergi kan atomerna skicka iväg röntgenfotoner vars energi beror på atomslaget. Genom att mäta energin på röntgenfotonerna som sänds ut från provet och koppla det till positionen av elektronstrålen på provet kan sammansättningen kartläggas med mycket hög upplösning.

I figur 4 illustreras sammansättningen av fyra bilder som är uppbyggda av intensiteten av röntgenstrålar från gallium, indium, arsenik och antimon. Intensiteten i dessa bilderna är proportionell mot förekomsten av respektive ämne. Det vita strecket markerar den position längs nanotråden där skiftet från indium till gallium sker, vilket är ett par nanometer före bytet från arsenik till gallium. I och med detta får planavstånden sin förklaring: på grund av bytet från indium till gallium sker före bytet från arsenik till antimon bildas det i övergångsregionen ett kort segment GaAs. Om man tillverkar transistorer av de här nanotrådarna kommer GaAs-segmentet fungera som en barriär som försämrar transporten av elektroner genom nanotråden. Detta är inte nödvändigtvis en nackdel eftersom detta kan förhindra att ström läcker igenom nanotråden då transistorn är avstängd.

Det här är ett exempel taget ut denna avhandling som visar hur det med hjälp av transmissionselektronmikroskop är möjligt att bestämma både struktur och sammansättning på halvledarmaterial ner till nanometernivå. Nanotrådarnas prestanda som halvledarkomponenter kan mycket väl avgöras på denna nivån, så det kommer alltid finnas ett stort behov av den här typen av karakterisering. En mycket viktig aspekt saknas dock: hur materialet blev till. För att förstå strukturen och sammansättningen på de färdiga nanotrådarna måste de kopplas till modeller för hur nanotrådarna bildas. Enbart genom att göra denna kopplingen kan vi tillverka just de specifika strukturer vi är ute efter. Ett exempel på detta nämndes tidigare: genom att veta att guldpartikeln löser stora mängder gallium och indium då antimon är närvarande kan vi förstå varför diametern är större i GaSb-segmentet än i InAs-segentet. Just sådana kopplingar är ett genomgående tema i denna avhandling och de vetenskapliga artiklar den bygger på. Även om det är möjligt att dra slutsatser om hur växten gått till enbart genom att observera de färdiga nanotrådarna är detta en stor begränsning för TEM. Det finns dock möjlighet att med specialdesignade mikroskop eller provhållare växa nanotrådar inne i mikroskopet samtidigt som de observeras. På grund av dessa möjligheter kommer TEM att få en om möjligt ännu viktigare roll att fylla i den fortsatta jakten på mer avancerade halvledarstrukturer.

References

[1] T. Mårtensson et al., "Epitaxial III-V Nanowires on Silicon", *Nano Letters* **4** (2004) 1987–1990

[2] E. P. A. M. Bakkers, M. T. Borgström, and M. A. Verheijen, "Epitaxial Growth of III-V Nanowires on Group IV Substrates", *MRS Bulletin* **32** (2007) 14–19

[3] F. Glas, "Critical Dimensions for the Plastic Relaxation of Strained Axial Heterostructures in Free-Standing Nanowires", *Physical Review B* **74** (2006) 121302(R)

[4] K. Tomioka, M. Yoshimura, and T. Fukui, "A III-V Nanowire Channel on Silicon for High-Performance Vertical Transistors", *Nature* **488** (2012) 189–192

[5] J. Wallentin et al., "InP Nanowire Array Solar Cells Achieving 13.8% Efficiency by Exceeding the Ray Optics Limit", *Science* **339** (2013) 1057–1060

[6] C. P. T. Svensson et al., "Monolithic GaAs/InGaP Nanowire Light Emitting Diodes on Silicon", *Nanotechnology* **19** (2008) 305201

[7] E. D. Minot et al., "Single Quantum Dot Nanowire LEDs", *Nano Letters* **7** (2007) 367–371

[8] C. Thelander et al., "Nanowire-Based One-Dimensional Electronics", *Materials Today* **9** (2006) 28–35

[9] J. Wallentin et al., "High-Performance Single Nanowire Tunnel Diodes", *Nano Letters* **10** (2010) 974–979

[10] B. M. Borg et al., "InAs/GaSb Heterostructure Nanowires for Tunnel Field-Effect Transistors", *Nano Letters* **10** (2010) 4080–4085

[11] S. O. Koswatta, S. J. Koester, and W. Haensch, "On the Possibility of Obtaining MOSFET-Like Performance and Sub-60-mV/dec Swing in 1-D Broken-Gap Tunnel Transistors", *IEEE Transactions on Electron Devices* **57** (2010) 3222–3230

[12] S. Nadj-Perge, S. M. Frolov, E. P. A. M. Bakkers, and L. P. Kouwenhoven, "Spin-Orbit Qubit in a Semiconductor Nanowire", *Nature* **468** (2010) 1084–1087

[13] V. Mourik et al., "Signatures of Majorana Fermions in Hybrid Superconductor-Semiconductor Nanowire Devices", *Science* **336** (2012) 1003–1007

[14] M. T. Deng et al., "Anomalous Zero-Bias Conductance Peak in a Nb-InSb Nanowire-Nb Hybrid Device", *Nano Letters* **12** (2012) 6414–6419

[15] D. B. Williams and C. B. Carter, *Transmission Electron Microscopy: A Textbook for Materials Science*, Springer, New York, 2nd edition (2009)

[16] R. R. Meyer, A. I. Kirkland, R. E. Dunin-Borkowski, and J. L. Hutchison, "Experimental Characterisation of CCD Cameras for HREM at 300 kV", *Ultramicroscopy* **85** (2000) 9–13

[17] S. Haigh, *Super Resolution Tilt Series Exit Wave Restoration from Aberration Corrected Images*, Ph.D. thesis, Oxford University (2008)

[18] M. A. O'Keefe, ""Resolution" in High-Resolution Electron Microscopy", *Ultramicroscopy* **47** (1992) 282–297

[19] A. I. Kirkland and R. R. Meyer, ""Indirect" High-Resolution Transmission Electron Microscopy: Aberration Measurement and Wavefunction Reconstruction", *Microscopy and Microanalysis* **10** (2004) 401–413

[20] P. W. Hawkes, "Aberration Correction Past and Present", *Philosophical Transactions of the Royal Society A* **367** (2009) 3637–3664

[21] A. F. de Jong and D. Van Dyck, "Ultimate Resolution and Information in Electron Microscopy II. The Information Limit of Transmission Electron Microscopes", *Ultramicroscopy* **49** (1993) 66–80

[22] K. Ishizuka, "FFT Multislice Method – The Silver Anniversary", *Microscopy and Microanalysis* **10** (2004) 34–40

[23] M. J. Hÿtch and W. M. Stobbs, "Quantitative Comparison of High Resolution TEM Images with Image Simulations", *Ultramicroscopy* **53** (1994) 191–203

[24] A. Thust, "High-Resolution Transmission Electron Microscopy on an Absolute Contrast Scale", *Physical Review Letters* **102** (2009) 220801

[25] F. F. Krause et al., "Comparison of Intensity and Absolute Contrast of Simulated and Experimental High-Resolution Transmission Electron Microscopy Images for Different Multislice Simulation Methods", *Ultramicroscopy* **134** (2013) 94–101

[26] C. B. Boothroyd, "Why Don't High-Resolution Simulations and Images Match?", *Journal of Microscopy* **190** (1998) 99–108

[27] D. Van Dyck, "Persistent Misconceptions about Incoherence in Electron Microscopy", *Ultramicroscopy* **111** (2011) 894–900

[28] M. Lentzen, "Progress in Aberration-Corrected High-Resolution Transmission Electron Microscopy Using Hardware Aberration Correction", *Microscopy and Microanalysis* **12** (2006) 191–205

[29] A. I. Kirkland, R. R. Meyer, and L.-Y. S. Chang, "Local Measurement and Computational Refinement of Aberrations for HRTEM", *Microscopy and Microanalysis* **12** (2006) 461–468

[30] S. Haigh, H. Sawada, and A. I. Kirkland, "Atomic Structure Imaging Beyond Conventional Resolution Limits in the Transmission Electron Microscope", *Physical Review Letters* **103** (2009) 126101

[31] F. Zemlin, K. Weiss, P. Schiske, and W. Kunath, "Coma-Free Alignment of High Resolution Electron Microscopes with the Aid of Optical Diffractograms", *Ultramicroscopy* **3** (1978) 49–60

[32] J. L. Hutchison et al., "A Versatile Double Aberration-Corrected, Energy Filtered HREM/STEM for Materials Science", *Ultramicroscopy* **103** (2005) 7–15

[33] R. R. Meyer, A. I. Kirkland, and W. O. Saxton, "A New Method for the Determination of the Wave Aberration Function for High Resolution TEM 1. Measurement of the Symmetric Aberrations", *Ultramicroscopy* **92** (2002) 89–109

[34] R. R. Meyer, A. I. Kirkland, and W. O. Saxton, "A New Method for the Determination of the Wave Aberration Function for High-Resolution TEM. 2. Measurement of the antisymmetric aberrations", *Ultramicroscopy* **99** (2004) 115–123

[35] M. Haider et al., "Electron Microscopy Image Enhanced", *Nature* **392** (1998) 768–769

[36] L. Y. Chang, F. R. Chen, A. I. Kirkland, and J. J. Kai, "Calculations of Spherical Aberration-Corrected Imaging Behaviour", *Journal of Electron Microscopy* **52** (2003) 359–364

[37] M. Lentzen et al., "High-Resolution Imaging with an Aberration-Corrected Transmission Electron Microscope", *Ultramicroscopy* **92** (2002) 233–242

[38] C.-L. Jia, M. Lentzen, and K. W. Urban, "High-Resolution Transmission Electron Microscopy Using Negative Spherical Aberration", *Microscopy and Microanalysis* **10** (2004) 174–184

[39] C.-L. Jia, M. Lentzen, and K. Urban, "Atomic-Resolution Imaging of Oxygen in Perovskite Ceramics", *Science* **299** (2003) 870–873

[40] K. W. Urban, "Studying Atomic Structures by Aberration-Corrected Transmission Electron Microscopy", *Science* **321** (2008) 506–510

[41] L.-Y. Chang and A. I. Kirkland, "Comparisons of Linear and Nonlinear Image Restoration", *Microscopy and Microanalysis* **12** (2006) 469–475

[42] A. Thust, W. M. J. Coene, M. Op De Beeck, and D. Van Dyck, "Focal-Series Reconstruction in HRTEM: Simulation Studies on Non-Periodic Objects", *Ultramicroscopy* **64** (1996) 211–230

[43] W. O. Saxton, "What is the Focus Variation Method? Is it New? Is it Direct?", *Ultramicroscopy* **55** (1994) 171–181

[44] R. Brydson (ed.), *Aberration-Corrected Analytical Transmission Electron Microscopy*, Wiley (2011)

[45] S. Pennycook and D. Jesson, "High-Resolution Z-Contrast Imaging of Crystals", *Ultramicroscopy* **37** (1991) 14–38

[46] J. J. Friel and C. E. Lyman, "X-Ray Mapping in Electron-Beam Instruments", *Microscopy and Microanalysis* **12** (2006) 2–25

[47] R. F. Egerton, *Electron Energy-Loss Spectroscopy in the Electron Microscope*, Springer, 3rd edition (2011)

[48] R. F. Egerton, P. Li, and M. Malac, "Radiation Damage in the TEM and SEM", *Micron* **35** (2004) 399–409

[49] D. B. Williams, J. Michael, J. I. Goldstein, and A. D. Romig Jr., "Definition of the Spatial Resolution of X-Ray Microanalysis in Thin Foils", *Ultramicroscopy* **47** (1992) 121–132

[50] D. L. Smith, *Thin-Film Deposition: Principles and Practice*, McGraw Hill, New York (1995)

[51] G. B. Stringfellow, *Organometallic Vapor-Phase Epitaxy: Theory and Practice*, Academic Press, London, 2nd edition (1999)

[52] M. E. Messing, K. Hillerich, J. Johansson, K. Deppert, and K. A. Dick, "The Use of Gold for Fabrication of Nanowire Structures", *Gold Bulletin* **42** (2009) 172–181

[53] K. Hillerich, M. E. Messing, L. R. Wallenberg, K. Deppert, and K. A. Dick, "Epitaxial InP Nanowire Growth from Cu Seed Particles", *Journal of Crystal Growth* **315** (2011) 134–137

[54] A. T. Vogel et al., "Fabrication of High-Quality InSb Nanowire Arrays by Chemical Beam Epitaxy", *Crystal Growth & Design* **11** (2011) 1896–1900

[55] B. Mandl et al., "Crystal Structure Control in Au-Free Self-Seeded InSb Wire Growth", *Nanotechnology* **22** (2011) 145603

[56] M. Pozuelo et al., "Self-Catalyzed Growth of InP/InSb Axial Nanowire Heterostructures", *Journal of Crystal Growth* **329** (2011) 6–11

[57] K. A. Dick, "A Review of Nanowire Growth Promoted by Alloys and Non-Alloying Elements with Emphasis on Au-Assisted III-V Nanowires", *Progress in Crystal Growth and Characterization of Materials* **54** (2008) 138–173

[58] B. A. Wacaser et al., "Preferential Interface Nucleation: An Expansion of the VLS Growth Mechanism for Nanowires", *Advanced Materials* **21** (2009) 153–165

[59] S. Hofmann et al., "Ledge-Flow-Controlled Catalyst Interface Dynamics During Si Nanowire Growth", *Nature Materials* **7** (2008) 372–375

[60] C.-Y. Wen, J. Tersoff, M. C. Reuter, E. A. Stach, and F. M. Ross, "Step-Flow Kinetics in Nanowire Growth", *Physical Review Letters* **105** (2010) 195502

[61] C.-Y. Wen, M. C. Reuter, J. Tersoff, E. A. Stach, and F. M. Ross, "Structure, Growth Kinetics, and Ledge Flow During Vapor-Solid-Solid Growth of Copper-Catalyzed Silicon Nanowires", *Nano Letters* **10** (2010) 514–519

[62] S. H. Oh et al., "Oscillatory Mass Transport in Vapor-Liquid-Solid Growth of Sapphire Nanowires", *Science* **330** (2010) 489–493

[63] C.-Y. Wen et al., "Periodically Changing Morphology of the Growth Interface in Si, Ge, and GaP Nanowires", *Physical Review Letters* **107** (2011) 025503

[64] A. D. Gamalski, C. Ducati, and S. Hofmann, "Cyclic Supersaturation and Triple Phase Boundary Dynamics in Germanium Nanowire Growth", *Journal of Physical Chemistry C* **115** (2011) 4413–4417

[65] K. A. Dick et al., "The Morphology of Axial and Branched Nanowire Heterostructures", *Nano Letters* **7** (2007) 1817–1822

[66] M. T. Björk et al., "Nanowire Resonant Tunneling Diodes", *Applied Physics Letters* **81** (2002) 4458–4460

[67] M. T. Borgström, M. A. Verheijen, G. Immink, T. de Smet, and E. P. A. M. Bakkers, "Interface Study on Heterostructured GaP-GaAs Nanowires", *Nanotechnology* **17** (2006) 4010–4013

[68] N. Li, T. Y. Tan, and U. Gösele, "Transition Region Width of Nanowire Hetero- and pn-Junctions Grown Using Vapor-Liquid-Solid Processes", *Applied Physics A* **90** (2008) 591–596

[69] T. E. Clark et al., "Diameter Dependent Growth Rate and Interfacial Abruptness in Vapor-Liquid-Solid $Si/Si_{1-x}Ge_x$ Heterostructure Nanowires", *Nano Letters* **8** (2008) 1246–1252

[70] M. Paladugu et al., "Nature of Heterointerfaces in GaAs/InAs and InAs/GaAs Axial Nanowire Heterostructures", *Applied Physics Letters* **93** (2008) 101911

[71] P. Krogstrup et al., "Junctions in Axial III-V Heterostructure Nanowires Obtained via an Interchange of Group III Elements", *Nano Letters* **9** (2009) 3689–3693

[72] C.-Y. Wen et al., "Formation of Compositionally Abrupt Axial Heterojunctions in Silicon-Germanium Nanowires", *Science* **326** (2009) 1247–1250

[73] Y.-C. Chou et al., "Controlling the Growth of Si/Ge Nanowires and Heterojunctions Using Silver-Gold Alloy Catalysts", *ACS nano* **6** (2012) 6407–6415

[74] H. Geaney, E. Mullane, Q. M. Ramasse, and K. M. Ryan, "Atomically Abrupt Silicon-Germanium Axial Heterostructure Nanowires Synthesized in a Solvent Vapor Growth System", *Nano Letters* **13** (2013) 1675–1680

[75] K. A. Dick, J. Bolinsson, B. M. Borg, and J. Johansson, "Controlling the Abruptness of Axial Heterojunctions in III-V Nanowires: Beyond the Reservoir Effect", *Nano Letters* **12** (2012) 3200–3206

[76] K. Haraguchi, T. Katsuyama, K. Hiruma, and K. Ogawa, "GaAs p-n Junction Formed in Quantum Wire Crystals", *Applied Physics Letters* **60** (1992) 745–747

[77] J. Wallentin and M. T. Borgström, "Doping of Semiconductor Nanowires", *Journal of Materials Research* **26** (2011) 2142–2156

[78] R. E. Algra et al., "Twinning Superlattices in Indium Phosphide Nanowires", *Nature* **456** (2008) 369–372

[79] M. H. M. van Weert et al., "Zinc Incorporation via the Vapor-Liquid-Solid Mechanism into InP Nanowires", *Journal of the American Chemical Society* **131** (2009) 4578–4579

[80] L. S. Karlsson et al., "Understanding the 3D Structure of GaAs <111> B Nanowires", *Nanotechnology* **18** (2007) 485717

[81] M. T. Borgström, J. Wallentin, K. Kawaguchi, L. Samuelson, and K. Deppert, "Dynamics of Extremely Anisotropic Etching of InP Nanowires by HCl", *Chemical Physics Letters* **502** (2011) 222–224

[82] R. T. DeHoff, *Thermodynamics in Materials Science*, Tailor & Francis, Boca Raton, 2nd edition (2006)

[83] J. Johansson, C. P. T. Svensson, T. Mårtensson, L. Samuelson, and W. Seifert, "Mass Transport Model for Semiconductor Nanowire Growth", *Journal of Physical Chemistry B* **109** (2005) 13567–13571

[84] L. E. Fröberg et al., "Transients in the Formation of Nanowire Heterostructures", *Nano Letters* **8** (2008) 3815–3818

[85] L. E. Fröberg, W. Seifert, and J. Johansson, "Diameter-Dependent Growth Rate of InAs Nanowires", *Physical Review B* **76** (2007) 153401

[86] M. Jeppsson et al., "GaAs/GaSb Nanowire Heterostructures Grown by MOVPE", *Journal of Crystal Growth* **310** (2008) 4115–4121

[87] L. Lugani et al., "Modeling of InAs-InSb Nanowires Grown by Au-Assisted Chemical Beam Epitaxy", *Nanotechnology* **23** (2012) 095602

[88] Q. K. K. Liu, N. Moll, M. Scheffler, and E. Pehlke, "Equilibrium Shapes and Energies of Coherent Strained InP Islands", *Physical Review B* **60** (1999) 17008

[89] D. Kriegner et al., "Unit Cell Structure of Crystal Polytypes in InAs and InSb Nanowires", *Nano Letters* **11** (2011) 1483–1489

[90] V. G. Dubrovskii and N. V. Sibirev, "Growth Thermodynamics of Nanowires and its Application to Polytypism of Zinc Blende III-V Nanowires", *Physical Review B* **77** (2008) 035414

[91] J. Arbiol et al., "Triple-Twin Domains in Mg Doped GaN Wurtzite Nanowires: Structural and Electronic Properties of this Zinc-Blende-Like Stacking", *Nanotechnology* **20** (2009) 145704

[92] D. B. Holt, "Grain Boundaries in the Sphalerite Structure", *Journal of Physics and Chemistry of Solids* **25** (1964) 1385–1395

[93] D. B. Holt, "Polarity Reversal and Symmetry in Semiconducting Compounds with the Sphalerite and Wurtzite Structures", *Journal of Materials Science* **19** (1984) 439–446

[94] E. R. Hemesath, D. K. Schreiber, C. F. Kisielowski, A. K. Petford-Long, and L. J. Lauhon, "Atomic Structural Analysis of Nanowire Defects and Polytypes Enabled Through Cross-Sectional Lattice Imaging", *Small* **8** (2012) 1717–1724

[95] M. I. den Hertog et al., "Hidden Defects in Silicon Nanowires", *Nanotechnology* **23** (2012) 025701

[96] C. Yeh, Z. Lu, S. Froyen, and A. Zunger, "Zinc-Blende-Wurtzite Polytypism in Semiconductors", *Physical Review B* **46** (1992) 10086

[97] R. Leitsmann and F. Bechstedt, "Surface Influence on Stability and Structure of Hexagon-Shaped III-V Semiconductor Nanorods", *Journal of Applied Physics* **102** (2007) 063528

[98] T. Akiyama, K. Sano, K. Nakamura, and T. Ito, "An Empirical Potential Approach to Wurtzite-Zinc-Blende Polytypism in Group III-V Semiconductor Nanowires", *Japanese Journal of Applied Physics* **45** (2006) L275–L278

[99] J. Johansson et al., "Structural Properties of <111>B -Oriented III-V Nanowires", *Nature Materials* **5** (2006) 574–580

[100] S. Lehmann, J. Wallentin, D. Jacobsson, K. Deppert, and K. A. Dick, "A General Approach for Sharp Crystal Phase Switching in InAs, GaAs, InP, and GaP Nanowires Using Only Group V Flow", *Nano Letters* **13** (2013) 4099–4105

[101] F. Glas, J.-C. Harmand, and G. Patriarche, "Why Does Wurtzite Form in Nanowires of III-V Zinc Blende Semiconductors?", *Physical Review Letters* **99** (2007) 146101

[102] J. Johansson et al., "Diameter dependence of the wurtzite-zinc blende transition in InAs nanowires", *Journal of Physical Chemistry C* **114** (2010) 3837–3842

[103] H. J. Joyce, J. Wong-Leung, Q. Gao, H. H. Tan, and C. Jagadish, "Phase Perfection in Zinc Blende and Wurtzite III-V Nanowires Using Basic Growth Parameters", *Nano Letters* **10** (2010) 908–915

[104] K. A. Dick, C. Thelander, L. Samuelson, and P. Caroff, "Crystal Phase Engineering in Single InAs Nanowires", *Nano Letters* **10** (2010) 3494–3499

[105] C. Thelander, P. Caroff, S. Plissard, A. W. Dey, and K. A. Dick, "Effects of Crystal Phase Mixing on the Electrical Properties of InAs Nanowires", *Nano Letters* **11** (2011) 2424–2429

[106] M. T. Borgström et al., "Precursor Evaluation for In Situ InP Nanowire Doping", *Nanotechnology* **19** (2008) 445602

[107] V. A. Nebol'sin and A. A. Shchetinin, "Role of Surface Energy in the Vapor-Liquid-Solid Growth of Silicon", *Inorganic Materials* **39** (2003) 899–903

[108] D. Cohen, S. McKernan, and C. B. Carter, "Characterization of the Absolute Crystal Polarity across Twin Boundaries in Gallium Phosphide Using Convergent-Beam Electron Diffraction", *Microscopy and Microanalysis* **5** (1999) 173–186

[109] E. Uccelli et al., "Three-Dimensional Multiple-Order Twinning of Self-Catalyzed GaAs", *Nano Letters* **11** (2011) 3827–3832

[110] K. Tomioka, J. Motohisa, S. Hara, and T. Fukui, "Control of InAs Nanowire Growth Directions on Si", *Nano Letters* **8** (2008) 3475–3480

[111] A. M. Munshi et al., "Vertically Aligned GaAs Nanowires on Graphite and Few-Layer Graphene: Generic Model and Epitaxial Growth", *Nano Letters* **12** (2012) 4570–4576

[112] M. I. den Hertog et al., "Correlation of Polarity and Crystal Structure with Optoelectronic and Transport Properties of GaN/AlN/GaN Nanowire Sensors", *Nano Letters* **12** (2012) 5691–5696

[113] J. S. Speck and S. F. Chichibu, "Nonpolar and Semipolar Group III Materials", *MRS Bulletin* **34** (2009) 304–309

[114] S. Krishnamoorthy, P. S. Park, and S. Rajan, "Demonstration of Forward Inter-Band Tunneling in GaN by Polarization Engineering", *Applied Physics Letters* **99** (2011) 233504

[115] M. de la Mata et al., "Polarity Assignment in ZnTe, GaAs, ZnO, and GaN-AlN Nanowires from Direct Dumbbell Analysis", *Nano Letters* **12** (2012) 2579–2586

[116] S. Fernández-Garrido et al., "Spontaneous Nucleation and Growth of GaN Nanowires: The Fundamental Role of Crystal Polarity", *Nano Letters* **12** (2012) 6119–6125

[117] G. Perillat-Merceroz, R. Thierry, P. H. Jouneau, P. Ferret, and G. Feuillet, "Compared Growth Mechanisms of Zn-Polar ZnO Nanowires on O-Polar ZnO and on Sapphire", *Nanotechnology* **23** (2012) 125702

[118] N. Jiang et al., "Polarity Determination by Atomic Location by Channeling-Enhanced Microanalysis", *Applied Physics Letters* **80** (2002) 389–391

[119] K. A. Mkhoyan, P. E. Batson, J. Cha, W. J. Schaff, and J. Silcox, "Direct Determination of Local Lattice Polarity in Crystals", *Science* **312** (2006) 1354

[120] H. Shtrikman et al., "Method for Suppression of Stacking Faults in Wurtzite III-V Nanowires", *Nano Letters* **9** (2009) 1506–1510

[121] S. D. Findlay et al., "Robust Atomic Resolution Imaging of Light Elements Using Scanning Transmission Electron Microscopy", *Applied Physics Letters* **95** (2009) 191913

[122] A. J. D'Alfonso, B. Freitag, D. Klenov, and L. J. Allen, "Atomic-Resolution Chemical Mapping Using Energy-Dispersive X-Ray Spectroscopy", *Physical Review B* **81** (2010) 100101(R)

[123] D. A. Muller et al., "Atomic-Scale Chemical Imaging of Composition and Bonding by Aberration-Corrected Microscopy", *Science* **319** (2008) 1073–1076

[124] A. Mikkelsen et al., "Direct Imaging of the Atomic Structure Inside a Nanowire by Scanning Tunnelling Microscopy", *Nature Materials* **3** (2004) 519–523

[125] G. Bertoni et al., "Direct Determination of Polarity, Faceting, and Core Location in Colloidal Core/Shell Wurtzite Semiconductor Nanocrystals", *ACS Nano* **6** (2012) 6453–6461

[126] K. Tillmann, K. W. Urban, and A. Thust, "Spherical Aberration Correction in Tandem with Exit-Plane Wave Function Reconstruction: Interlocking Tools for the Atomic Scale Imaging of Lattice Defects in GaAs", *Microscopy and Microanalysis* **10** (2004) 185–198

[127] X. Xu et al., "Distortion and Segregation in a Dislocation Core Region at Atomic Resolution", *Physical Review Letters* **95** (2005) 145501

[128] C. J. D. Hetherington, "HREM of Defects in Silicon at Twin Intersections", *Mat. Res. Soc. Symp. Proc.* **183** (1990) 123–134

[129] F. A. Ponce, D. P. Bour, W. T. Young, M. Saunders, and J. W. Steeds, "Determination of Lattice Polarity for Growth of GaN Bulk Single Crystals and Epitaxial Layers", *Applied Physics Letters* **69** (1996) 337–339

[130] J. Taftø and J. C. H. Spence, "A Simple Method for the Determination of Structure-Factor Phase Relationships and Crystal Polarity Using Electron Diffraction", *Journal of Applied Crystallography* **15** (1982) 60–64

[131] K. Marthinsen, T. Lindheim, and R. Høijer, "Non-Centrosymmetry Effects and Polarity Determination in III-V Semiconductors", *Acta Crystallographica* **A53** (1997) 366–375

[132] K. Mahalingam et al., "Compositional Analysis of Mixed-Cation-Anion III-V Semiconductor Interfaces Using Phase Retrieval High-Resolution Transmission Electron Microscopy", *Journal of Microscopy* **230** (2008) 372–381

[133] S. I. Molina et al., "Column-By-Column Compositional Mapping by Z-Contrast Imaging", *Ultramicroscopy* **109** (2009) 172–176

[134] S. Van Aert et al., "Quantitative Atomic Resolution Mapping Using High-Angle Annular Dark Field Scanning Transmission Electron Microscopy", *Ultramicroscopy* **109** (2009) 1236–1244

[135] H. Kauko et al., "Compositional Characterization of GaAs/GaAsSb Nanowires by Quantitative HAADF-STEM", *Micron* **44** (2013) 254–260

[136] A. Genc et al., "XEDS STEM Tomography for 3D Chemical Characterization of Nanoscale Particles", *Ultramicroscopy* **131** (2013) 24–32

[137] D. E. Perea et al., "Three-Dimensional Nanoscale Composition Mapping of Semiconductor Nanowires", *Nano Letters* **6** (2006) 181–185

[138] Y. Ashuach et al., "Atomic Intermixing in Short-Period InAs/GaSb Superlattices", *Applied Physics Letters* **100** (2012) 241604

[139] A. I. Persson et al., "Solid-Phase Diffusion Mechanism for GaAs Nanowire Growth", *Nature Materials* **3** (2004) 677–681

[140] K. Sader et al., "Smart Acquisition EELS", *Ultramicroscopy* **110** (2010) 998–1003

[141] M. G. Burke, M. Watanabe, D. B. Williams, and J. M. Hyde, "Quantitative Characterization of Nanoprecipitates in Irradiated Low-Alloy Steels: Advances in the Application of FEG-STEM Quantitative Microanalysis to Real Materials", *Journal of Materials Science* **41** (2006) 4512–4522

[142] P. M. Voyles, D. A. Muller, J. L. Grazul, P. H. Citrin, and H.-J. L. Gossmann, "Atomic-Scale Imaging of Individual Dopant Atoms and Clusters in Highly n-Type Bulk Si", *Nature* **416** (2002) 826–829

[143] D. A. Muller, P. M. Voyles, and E. J. Kirkland, "Depth-Dependent Imaging of Individual Dopant Atoms in Silicon", *Microscopy and Microanalysis* **10** (2004) 291–300

[144] J. Allen et al., "High-Resolution Detection of Au Catalyst Atoms in Si Nanowires", *Nature Nanotechnology* **3** (2008) 168–173

[145] M. Bar-Sadan, J. Barthel, H. Shtrikman, and L. Houben, "Direct Imaging of Single Au Atoms within GaAs Nanowires", *Nano Letters* **12** (2012) 2352–2356

[146] D. E. Perea et al., "Direct Measurement of Dopant Distribution in an Individual Vapour-Liquid-Solid Nanowire", *Nature Nanotechnology* **4** (2009) 315–319

[147] J. Palisaitis et al., "Standard-Free Composition Measurements of $Al_xIn_{1-x}N$ by Low-Loss Electron Energy Loss Spectroscopy", *Physica Status Solidi RRL* **5** (2011) 50–52

[148] L. H. G. Tizei, T. Chiaramonte, M. A. Cotta, and D. Ugarte, "Characterization of Interface Abruptness and Material Properties in Catalytically Grown III-V Nanowires: Exploiting Plasmon Chemical Shift", *Nanotechnology* **21** (2010) 295701

[149] J. Palisaitis et al., "Effect of Strain on Low-Loss Electron Energy Loss Spectra of Group-III Nitrides", *Physical Review B* **84** (2011) 245301

[150] M. W. Larsson et al., "Strain Mapping in Free-Standing Heterostructured Wurtzite InAs/InP Nanowires", *Nanotechnology* **18** (2007) 015504

[151] S. T. Murphy, A. Chroneos, C. Jiang, U. Schwingenschlögl, and R. W. Grimes, "Deviations from Vegard's Law in Ternary III-V Alloys", *Physical Review B* **82** (2010) 073201

[152] A. Béché, J. L. Rouvière, J. P. Barnes, and D. Cooper, "Strain Measurement at the Nanoscale: Comparison between Convergent Beam Electron Diffraction, Nano-Beam Electron Diffraction, High Resolution Imaging and Dark Field Electron Holography", *Ultramicroscopy* **131** (2013) 10–23

[153] A. Carlsson, L. Wallenberg, C. Persson, and W. Seifert, "Strain State in Semiconductor Quantum Dots on Surfaces: A Comparison of Electron Microscopy and Finite Element Calculations", *Surface Science* **406** (1998) 48–56

[154] J. L. Taraci et al., "Strain Mapping in Nanowires", *Nanotechnology* **16** (2005) 2365–2371

[155] D. Ercolani et al., "InAs/InSb Nanowire Heterostructures Grown by Chemical Beam Epitaxy", *Nanotechnology* **20** (2009) 505605

[156] G. Tourbot et al., "Structural and Optical Properties of InGaN/GaN Nanowire Heterostructures Grown by PA-MBE", *Nanotechnology* **22** (2011) 075601

[157] M. J. Hÿtch, E. Snoeck, and R. Kilaas, "Quantitative Measurement of Displacement and Strain Fields from HREM Micrographs", *Ultramicroscopy* **74** (1998) 131–146

[158] N. Shin and M. A. Filler, "Controlling Silicon Nanowire Growth Direction via Surface Chemistry", *Nano Letters* **12** (2012) 2865–2870

[159] R. E. Algra et al., "Formation of Wurtzite InP Nanowires Explained by Liquid-Ordering", *Nano Letters* **11** (2011) 44–48

[160] P. Krogstrup et al., "In-Situ X-Ray Characterization of Wurtzite Formation in GaAs Nanowires", *Applied Physics Letters* **100** (2012) 093103

[161] J. B. Wagner, F. Cavalca, C. D. Damsgaard, L. D. L. Duchstein, and T. W. Hansen, "Exploring the Environmental Transmission Electron Microscope", *Micron* **43** (2012) 1169–1175

[162] J. F. Creemer et al., "Atomic-Scale Electron Microscopy at Ambient Pressure", *Ultramicroscopy* **108** (2008) 993–998

[163] E. A. Stach et al., "Watching GaN Nanowires Grow", *Nano Letters* **3** (2003) 867–869

[164] A. D. Gamalski, J. Tersoff, R. Sharma, C. Ducati, and S. Hofmann, "Formation of Metastable Liquid Catalyst During Subeutectic Growth of Germanium Nanowires", *Nano Letters* **10** (2010) 2972–2976

[165] H. D. Park, S. M. Prokes, and R. C. Cammarata, "Growth of Epitaxial InAs Nanowires in a Simple Closed System", *Applied Physics Letters* **87** (2005) 063110

[166] P. Madras, E. Dailey, and J. Drucker, "Kinetically Induced Kinking of Vapor-Liquid-Solid Grown Epitaxial Si Nanowires", *Nano Letters* **9** (2009) 3826–3830

[167] K. W. Schwarz, J. Tersoff, S. Kodambaka, Y.-C. Chou, and F. M. Ross, "Geometrical Frustration in Nanowire Growth", *Physical Review Letters* **107** (2011) 265502

[168] K. Hillerich et al., "Strategies To Control Morphology in Hybrid Group III-V/Group IV Heterostructure Nanowires", *Nano Letters* **13** (2013) 903–908

[169] J. R. Jinschek and S. Helveg, "Image Resolution and Sensitivity in an Environmental Transmission Electron Microscope", *Micron* **43** (2012) 1156–1168

[170] A. N. Bright, K. Yoshida, and N. Tanaka, "Influence of Total Beam Current on HRTEM Image Resolution in Differentially Pumped ETEM with Nitrogen Gas", *Ultramicroscopy* **124** (2013) 46–51

[171] S. Van Aert, K. J. Batenburg, M. D. Rossell, R. Erni, and G. Van Tendeloo, "Three-Dimensional Atomic Imaging of Crystalline Nanoparticles", *Nature* **470** (2011) 374–377

[172] C.-C. Chen et al., "Three-Dimensional Imaging of Dislocations in a Nanoparticle at Atomic Resolution", *Nature* **496** (2013) 74–79

[173] M. Hjort et al., "Surface Chemistry, Structure, and Electronic Properties from Microns to the Atomic Scale of Axially Doped Semiconductor Nanowires", *ACS Nano* **6** (2012) 9679–9689

[174] M. I. den Hertog et al., "Mapping Active Dopants in Single Silicon Nanowires Using Off-Axis Electron Holography", *Nano Letters* **9** (2009) 3837–3843

[175] M. Kociak and J. Garcia de Abajo, "Nanoscale Mapping of Plasmons, Photons, and Excitons", *MRS Bulletin* **37** (2012) 39–46

[176] L. H. G. Tizei, T. Chiaramonte, D. Ugarte, and M. A. Cotta, "III-V Semiconductor Nanowire Growth: Does Arsenic Diffuse Through the Metal Nanoparticle Catalyst?", *Nanotechnology* **20** (2009) 275604

Acknowledgements

There are many people who I would like to thank for all their help and support over the past five years.

First and foremost are Reine and Kimberly. You make a great pair of supervisors. Thanks for all the guidance, inspiration, 3 a.m. emails, and help you have given me. You always manage to make your PhD students feel appreciated, which just adds to the motivation. Also, thanks for letting me tag along on the most interesting shopping trip I have ever been to.

When it comes to the microscopy, Gunnel, Crispin and Lisa deserve special mention. Gunnel, without you the microscopes would not keep running as smoothly as they do. I'm still not sure why I gained your trust, but I have really enjoyed all the maintenance I've been allowed to help out with. Crispin, having you around has really kept me on my toes regarding all things TEM. Thank you very much for looking through the TEM chapter. Lisa, the one week intensive training was really the best start I can imagine for my PhD studies.

It has been great to be part of the nanometre structure consortium and get to meet so many wonderful and brilliant people. Also, without the never-ending supply of new, fantastic, and sometimes weird nanowires from Solid State Physics there would not have been much for me to do. A few people deserve special mention for keeping me busy over the past five years.

Jesper and Magnus: you have been a fixture during the whole time, coming up with new projects at a rate that is hard to match. I have been constantly impressed by how much the two of you know about all things related to nanowires, if somewhat less impressed by Jesper's ability for recognizing jackets.

In the InAs-GaSb related projects, I couldn't have hoped for a better group than Mattias, Anil, Johannes, Barham, Claes, and Lars-Erik. It was great to have discussions with so many different disciplines represented and I really enjoyed working together with you all. I would like to thank Mattias in particular for all the great and detailed feed-back I got on results and manuscripts.

Magnus, Martin, David, Knut, and Lars: thank you for letting me sneak on board the aerotaxy project for a while. It is a very exciting project to have had a small part in.

Sepideh, although we started working together quite late it's been a great experience. I wish you the best of luck at the microscope now that you will use it yourself (not that you will need it).

There are of course many more people and projects that all have been very inspiring to work with. Jessica, thanks for your incredible drive and for getting me involved in the projects with Anders and Jonas. Philippe, it's been great to interact with you both through "track changes" in word and over a glass (or bottle) of wine at conferences. I would also like to thank Sonia and Anna at EPFL for letting me have a look at their nanowings: time really *flew* by during that project.

I would also like to thank all the other PhD students with whom I have shared the microscope. Maria, you are probably the most positive and hardest working person I have met. Filip, sharing an office, ideas, and complaints about the microscope with you has made all the difference. You and Maria have both been great company during the conferences. Karla, thanks again for stepping in and saving the microscope. Daniel, you and Sebastian have been my nanowire support-line. Sebastian, you deserve huge credits for checking the chapters on growth and crystal structure.

Work wouldn't have been the same without all my fellow PhD students at the division formerly known as Polymer & Materials Chemistry. Just from there having been two different groups of people around over the years makes it feel almost like I have worked at two different places. Anna, Elin and Shogo, it was a minimal division during our time, but very cosy. Isa, Carola, Carlos, Annika, Matilda, and Filip, thanks for all the laughs during fika. Annika and Matilda, it's a relief to know that at least the strong survived my brief stint in the polymer physics course. At CAS, I would also like to thank Maria for all your help with the defence and all things administrative.

Finally, I would like to thank my family for encouraging me when I wanted to be a "fårskare" as a kid. It is thanks to your support that I have been able to keep striving for that goal.

Sara, you have been the best coach and cheerleader imaginable. You have given me the perspective to appreciate my job even when the projects have not been going the way I planned, and have made the past years much happier than I could have hoped for. I hope you know how grateful I am.